Geometric and Dynamic Analysis of Shoe-type Centerless Grinding

by

James E. Charmley

Submitted to the Department of Mechanical Engineering
in partial fulfillment of the requirements for the degrees of

Bachelor of Science in Mechanical Engineering

and

Master of Science in Mechanical Engineering

at the

MASSACHUSETTS INSTITUTE OF TECHNOLOGY

February 1992

Author .....
Department of Mechanical Engineering
December 15, 1991

Certified by 12/17/91
George Chryssolouris
Associate Professor
Thesis Supervisor

Accepted by .....
Professor A.A. Sonin
Departmental Committee on Graduate Students

Geometric and Dynamic Analysis of Shoe-type Centerless Grinding

by

James E. Charmley

Submitted to the Department of Mechanical Engineering
on December 15, 1991, in partial fulfillment of the
requirements for the degrees of
Bachelor of Science in Mechanical Engineering
and
Master of Science in Mechanical Engineering

Abstract

Centerless grinding is a process which can produce workpieces with accurate circular cross sections at high production rates. This study analyzes a form of centerless grinding called shoe-type centerless grinding where the workpiece is held between a grinding wheel and two flat supports. The goal of this study was to analyze the effects of the angular position of these support "shoes" on the geometric and dynamic stability of the process. A model of shoe-type centerless grinding is proposed and analyzed to find the modes of geometric instability along with the roots of the model's characteristic equation. Application of the proposed model produced the following main results.

1. Accurate predictions of lobing instability were found for a dynamically stable machine based solely set up condition geometry.

2. Part roundness trends were derived based on set up geometry. Center-height angles from 13 to 20 degrees produced the best overall part roundness for shoe-type centerless grinding.

3. Vibration growth rates were found for a range of set up conditions based on the stable and unstable roots of the model's characteristic equation.

Grinding experiments at various set up geometries support the theoretical conclusions proposed in this study, confirming the validity of the model and the ability to characterize the centerless grinding process.

Thesis Supervisor: George Chryssolouris
Title: Associate Professor

Acknowledgments

I would like to thank Dr. Fukuo Hashimoto whose knowledge of dynamics and centerless grinding greatly aided in the development of this thesis and whose knowledge of business has helped my lifetime and professional advancement.

Also, I would like to thank The Timken Company where this research was conducted. Both the employees and management were more than helpful in assisting me with this study.

Finally, I would like to thank Professor Chryssolouris who taught me not to be afraid to keep asking the question 'Why?'.

Contents

Chapter 1

Introduction

Cylindrically shaped parts are fundamental to many industries, especially the roller bearing industry. Cylindrical parts are usually made with a turning or grinding process. For analysis, it is crucial to understand the geometry and basic physics of a process whose goal is the production perfectly circular cross sections. A perfect circle is fully defined either by a center and a radius or by three points on the circumference, and precision production of circular cross sections requires strict adherance to one of these two definitions.

There are two types of grinding processes which produce circular cross sections. The process based on the first definition of a circle, establishing a center and a radius, is called center-type grinding. Center-type grinding employs two coned shaped centers which are thrust into the faces of a cylinder while the grinding wheel is positioned a constant distance from the centers during workpiece/grinding wheel rotation as shown in Figure 1.1. This method of grinding is flexible and is well suited for low volume production. Difficulties with this method include: the accurate placement of the centers on the workpiece axis, the constant distance maintenance of the grinding wheel during processing, and the deflection of the workpiece due to the bending moment from the cones and the grinding wheel.

The second definition of an ideal circle, three points on the circumference, is met with a process called centerless grinding. In centerless grinding the workpiece is held between the grinding wheel and two other points (often a regulating wheel

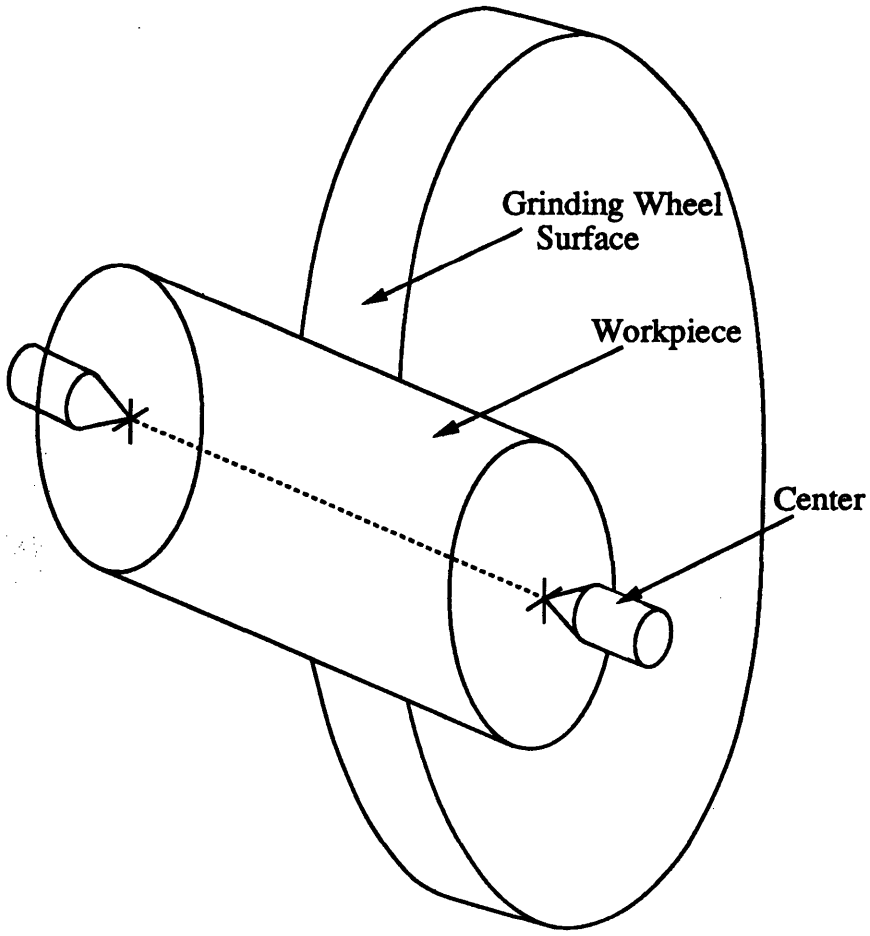

Figure 1-1: Center-type Grinding where Grinding Wheel is kept a constant distance from the cone to cone centerline.

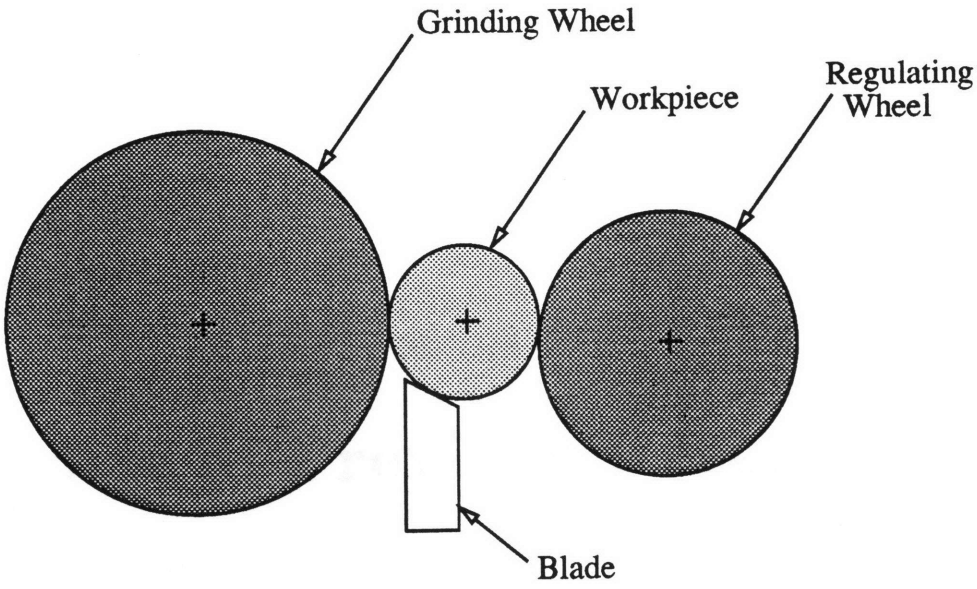

Figure 1-2: Centerless Grinding with the workpiece held at 3 contact points.

and a metal blade) as shown in Figure 1.2. Centerless grinding has many advantages unavailable to center-type or other, over-constrained processes. Centerless grinding optimally constrains the circular workpiece geometry,has high production rates, and can maintain high roundness accuracy. Difficulties with centerless grinding include the lack of stiffness of the machine system and the optimal placement of the two contact points in relation to the grinding wheel during processing.

This study attempts to address the difficulties in centerless grinding including: the effect of set up geometry on the production of accurately round workpieces, the effect of overall machine stiffness on the production of round workpieces, and the effect of set up geometry on unstable vibration given the machine's finite stiffness. As will be seen, the angular placement of the two support points greatly affects the accuracy and stability of the centerless grinding process.

This thesis will first review the seventy-year history of published research into centerless grinding and show the overall lack of comprehensive analysis. Then, a geometric and dynamic model of centerless grinding will be proposed, analyzed, and experimentally evaluated in terms of the accuracy of part cross-section roundness and process dynamic stability. A shoe-type centerless grindiner will be used as the basis for analysis and experimental work in this study.

Chapter 2

Review of Previous Research

Turning and grinding are two major forms of metal removal. Extensive research over several decades has been devoted to the analysis of turning. Grinding is similar to turning in many ways, though it is more complicated to anlayze due to the granular cutting edge of the grinding wheel. Weck[29] formed a good comparison between the turning and grinding processes by applying information previously used in turning to grinding. Weck concluded that grinding is more intricate and complicated than turning due to the high number of micro-cutting surfaces involved.

In 1985, Matsubara and others[6] analyzed orthogonal and three-dimensional turning with a complicated mathematical model based on the structural dynamics of the workpiece, tool, and machine. In turning, bumps or lobes on the surface of the workpiece can affect the cutting process in subsequent revolutions; see Figure 2.1. Depending on speed, stiffness, and other parameters, if lobing frequency matches the tool's vibration, then greater and greater undulations are generated around the workpiece resulting in harmonic vibration known as chatter. Matsubara established stability limits to avoid this regenerative effect in turning. As will be seen below, it would be beneficial if similar limits could be found for centerless grinding.

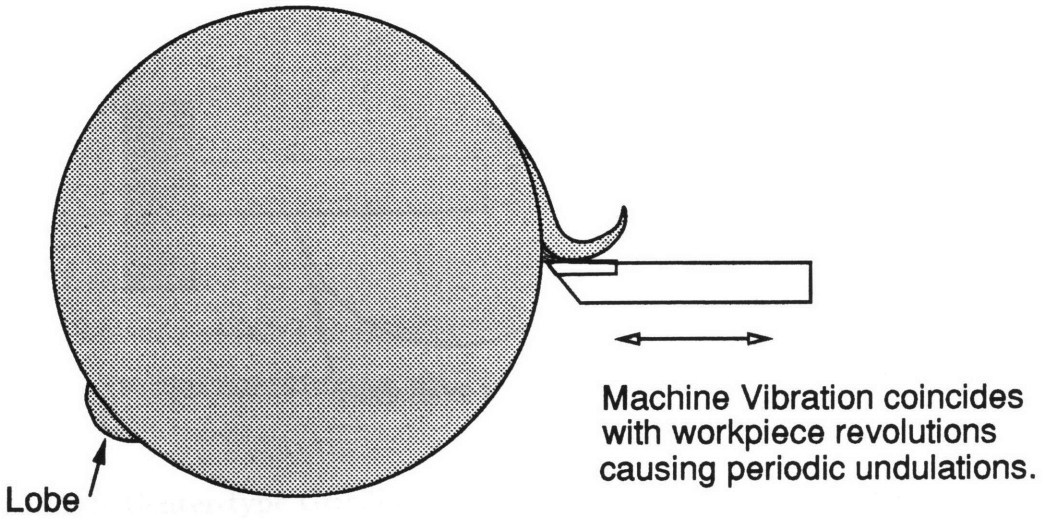

Figure 2-1: Diagram of Turning Operation Showing Regeneration Effect.

2.1 Center-type Grinding Research

In turning, a round workpiece will regenerate surface lobes in rotation. In grinding this regeneration effect is double since both the workpiece and the grinding wheel can have repeating surface undulations as shown in Figure 2.2. The first in-depth analysis of the dual grinding wheel and workpiece regeneration process was conducted by R.S. Hahn. This original work was extended by Snoeys and Brown[34] in 1969. By making simplifying assumptions that the workpiece was rigid and that the machine structure had only one mode of vibration, they were able to model center-type grinding and establish stability limits based on root locus analysis and grinding wheel stiffness.

Snoeys work was furthered by Inaski and Yonetsu[31], who solved the characteristic equation of the center-type model and defined stable and unstable grinding regions based on workpiece speed and depth of cut. A significant result from this research was an initial estimation of regenerative chatter amplitude growth rate and the explanation of chatter during spark-out processes.

In a thorough report[33] from 1971, Furukawa, Miyashita, and Shiozaki analyzed both the stable and unstable regions of grinding. They showed that although some practical grinding applications are conducted in the theoretically unstable region,

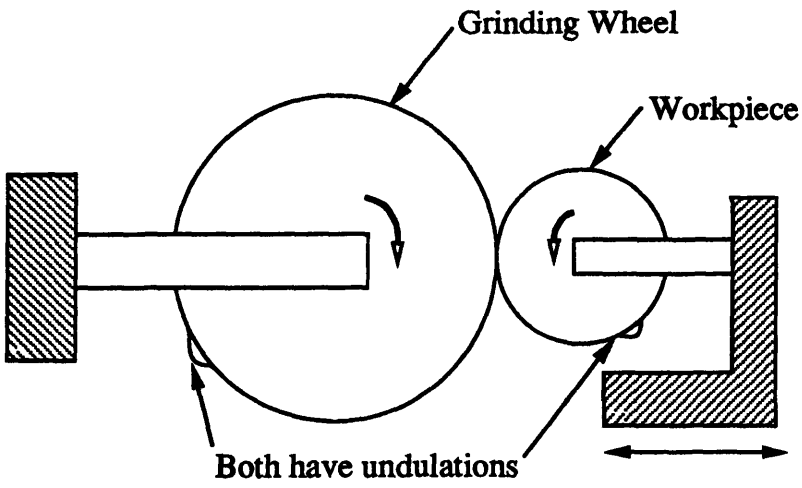

Figure 2-2: Center-type Grinding Operation Showing Double Regeneration Effect.

grinding chatter sometimes grows at extremely slow rates. Also, both workpiece and grinding wheel waviness were found to be factors in the process. In a later report[25], Miyashita showed that a higher stiffness, higher speed grinder would have a larger stable operating region than conventional grinders.

In the grinding process, low frequency vibrations of the grinding wheel will be transmitted to the workpiece in the form of surface undulations. At higher and higher vibration frequencies, the copying mechanism from the wheel to the workpiece eventually diminishes until almost no vibration from the grinding wheel is transmitted to the workpiece. This effect is called geometrical interference and it can play an important role in the stabilization of high frequency chatter. In 1984, Hashimoto, Miyashita, and Kanai[23] added geometrical interference to their grinding model and analyzed resultant levels of instability and chatter growth.

Srinivasan[28] used the spectrum method and a model similar to Miyashita's for estimation of wheel regenerative chatter based on the unstable roots of the model's characteristic equation. In a later paper[22], Hashimoto and Miyashita showed another method to analyze the roots of the characteristic equation and estimate the growth rate of chatter vibration. Testing showed that this model was sufficient to predict the growth rate of chatter for several different grinding wheels.

In 1986, Matsubara, Mizumoto, and Yamamoto[5] modified previous models and

presented a new block diagram of the chatter phenomenon in center-type grinding accounting for more grinding parameters including energy, frequency, and damping. They solved for unstable roots and proposed an optimal stability criterion. Matsubara followed this paper with an experimental evaluation[4] showing that the model was very accurate. The only significant limitation of the model was that the structural dynamics of the machine only had one degree of freedom. Several valuable results from this line of research can be applied to centerless grinding including the fact that high machine structural stiffness reduces chatter.

2.2 Wheel-type Centerless Grinding Research

2.2.1 Process Geometry Research

Of the forms of grinding, centerless grinding is more recently developed. In wheel-type centerless grinding, the workpiece is held between the grinding wheel, a regulating wheel, and a stationary support blade, as shown in Figure 2.3, leading to more complicated delay effects not found in other processes. The first qualitative analysis of centerless grinding was published in 1925 by Peets. In 1939 another approach was taken by Sachsenberg and Kreher[38], but the first broad study of the out-of-round condition was conducted by Dall[37] in 1946. Dall investigated the rate of reduction in the initial out-of-roundness of a workpiece in centerless grinding, and later Yonetsu investigated the same problem with harmonic analysis techniques.

In 1964, W.B. Rowe in Manchester, England took another approach. Rowe and Koenigsberger[11] introduced a model including two delays and a regeneration effect which was used to predict the geometric stability of centerless grinding. In their papers, they used computer simulation[12] to track the workpiece roundness throughout the grinding process. Though it made many assumptions, their model showed that the process and geometry could be adequately modeled. Through discretization of the workpiece surface, they found the effect of grinding a stepped surface workpiece in terms of roundness. Although the theory and testing were conducted in a generally

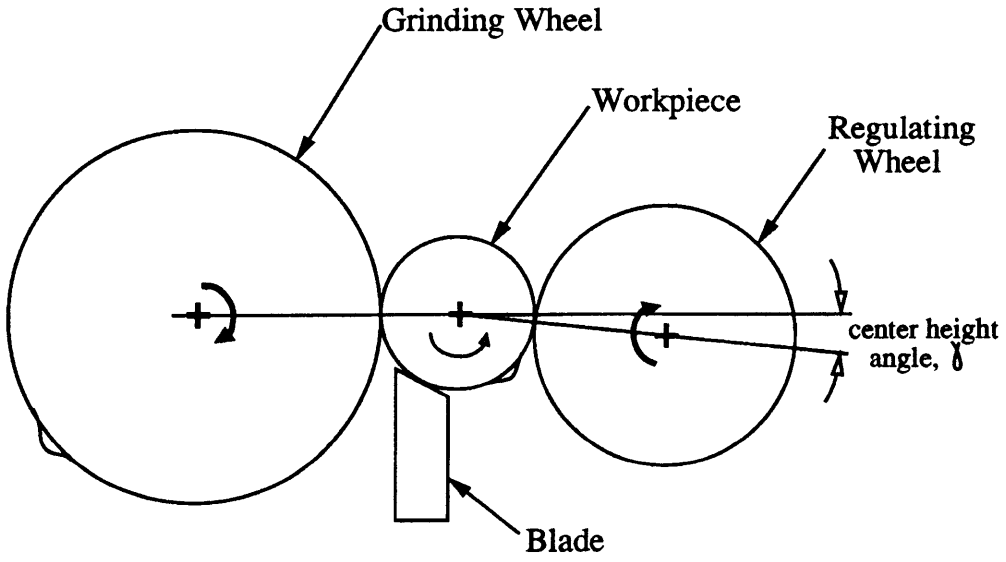

Figure 2-3: Wheel-type Centerless Grinding Operation Showing Regeneration Effects.

unstable set up region, experiments verified the validity of their model and initial stability charts based on grinding angle were formed.

Further work by Rowe and Koenigsberger[10] applied Rowe's model to frequency analysis of the rounding effect in centerless grinding. The analysis was mainly static, but it found that the workpiece center-height angle (see Figure 2.3) produces odd order lobing below six degrees and even order lobing above eight degrees, with best overall roundness results between six and eight degrees. This result holds today for wheel-type centerless grinding.

In subsequent work,[8,9] Rowe continued to further his geometric analysis in the frequency domain and showed the extent of instability for some geometric set-ups. Results showed that the work support blade angle and the speed of the workpiece affect the stability of the system. Often, a slower workpiece speed will reduce chatter due to the wheel copying mechanism previously mentioned. Also, two work support blade angles were tested, and it was found that a blade angle of 30 degrees is better than a blade angle of 20 degrees.

More recently, in 1981, Chien extended Rowe's earlier work by simplifying process assumptions[18]. Using the lever postulate of roundness error on a workpiece, out of round lobes were modeled with a four bar linkage. As a result, a new form of the stability diagram was shown. In subsequent papers[16,17] Chien optimized the analysis and showed that particular lobing instability could be minimized with his table. One inherent drawback of Chien's analysis is the inability to know the general degree of instability for any particular set up. For example, all set up conditions contain some instability, but some set up conditions take a few seconds to produce significant lobing while others take several minutes.

Probably the most comprehensive research into the geometric stability of centerless grinding was published by Frost and Furdson in 1985[21]. Their work showed that very little of the centerless grinding region is geometrically stable, and that workpiece roundness depends more on the number of workpiece revolutions during grinding rather than on total grinding time.

2.2.2 Dynamic Behavior Research

The first electronic simulation of centerless grinding was conducted by Gurney[36] who applied other machine analysis techniques to investigate transient forces in centerless grinding. Although no experimental work was published, Gurney used an analog computer to simulate the triple delay effect found in centerless grinding. The results of his work were semi-accurate stability diagrams depicting dynamically stable and unstable set up conditions over a small range.

In 1969, a researcher in Tokyo, Masakazu Miyashita, published a paper[26] showing extensive research into the dynamics of centerless grinding. His work analyzed both the static and dynamic stability of the workpiece and wheel system under forced vibration. The model which Miyashita developed not only included the triple delay work mechanism, but also the machine compliance and the grinding wheel and regulating wheel wear. Rowe had earlier predicted that the optimal center height degrees was between 6 and 8 degrees, and Miyashita's main result narrowed that prediction to a center height angle of seven degrees.

In 1982, Miyashita, Hashimoto, and Kanai[24] extended Miyashita's earlier work by producing a diagram showing the level of instability for different set up operations. Also in this work, there was a detailed analysis of the root locus solution to the characteristic equation governing the system. This work is probably the most comprehensive centerless grinding research to date, but even it made several assumptions, including the neglect of the blade angle (ϕ_1) influence which will be shown below as being important in shoe-type grinding.

All of the papers presented so far have analyzed the centerless grinding process in two dimensions assuming constant depth of the workpiece. One study by Udupa et al[13] showed that the process could be modeled three dimensionally. Although the model was not theoretically intensive, it was verified by experiments that with specific geometry the process is slightly different when viewed from a three-dimensional perspective. For most purposes though, a two-dimensional representation is sufficient for modeling.

2.2.3 Combined Geometric and Dynamic Research

In the earliest analysis of centerless grinding, Gurney and Rowe recognized the importance of analyzing the system from both a geometric and dynamic standpoint. Not until very recently was this attempted by researchers, Bueno et al[1], in Spain. Bueno's work was an extension and compilation of both Miyashita's and Rowe's. The analysis showed that no set-up of the centerless grinding machine can be completely free from instability, but that some regions are more stable than others. Unfortunately, Bueno's methodology did not allow for a parametric determination of set up condition stability. Also, Bueno's work has not been proven experimentally (and results of experiments presented here do not support Bueno's methodology).

Other work related to centerless grinding is useful for modeling. A study by Steffens[19,20] et al analyzed the microscopic grinding mechanism of grain to work chip formation and removal for analysis of dynamic stability. This analysis included kinematics, cutting forces, thermal behavior, and elastoplastic processes. An earlier study by Snoeys and Wang[35] looked at the static and dynamic stiffness of the grinding

wheel. Also, a study by Baylis and Stone[27] incorporated wheel compliance and contact stiffness to model the transient buildup of vibration. It was found that after initial buildup, the contact stiffness can be assumed constant for modeling purposes.

Several studies have discussed the optimal design of centerless grinders. One study by Rowe et al[7] showed that increasing the stiffness of the centerless grinding machine can greatly reduce the onset of chatter vibration. Another study by Lee and Furukawa[2,3] discussed the optimal stiffness and damping ratio of a grinder based on a simple, lumped parameter model of the system.

2.3 Shoe-type Centerless Grinding Research

Shoe-type centerless grinding is slightly different than wheel-type centerless grinding studied previously. In most centerless grinding operations, the regulating wheel is compliant rubber. In shoe-type grinding, the front shoe (support blade) and the rear shoe (in place of the regulating wheel) are typically both made of steel, shown in Figure 2.4. Although shoe-type grinding process geometry is the same as wheel-type, the system dynamic characteristics change. Also, in all studies noted, the workpiece was considered rigid, but with a stiff shoe and a thin walled workpiece, the workpiece will initially be considered compliant in this study.

As far as the author knows, study on shoe-type centerless grinding has only been published three times. Miyashita[32] did experimental analysis in his 1972 paper with the rear shoe fixed at eleven degrees resulting in a corresponding optimal front shoe placement at fifty-five degrees (which is supported by this study). Kotov and Gershenzon[30], two Russian authors, studied the rotational speed of the workpiece in shoe-type centerless grinding under one geometric configuration to find the maximum workpiece speed before seizing. Also, previously mentioned Frost and Furdson[21] used a shoe grinding set up to test unstable geometric lobing near ϕ_1=90 degrees (see Figure 3.2). All of this research was mostly experimental in nature, making it difficult to draw any general conclusions about shoe-type centerless grinding.

Most research to date has been concerned with only the geometric tendencies of

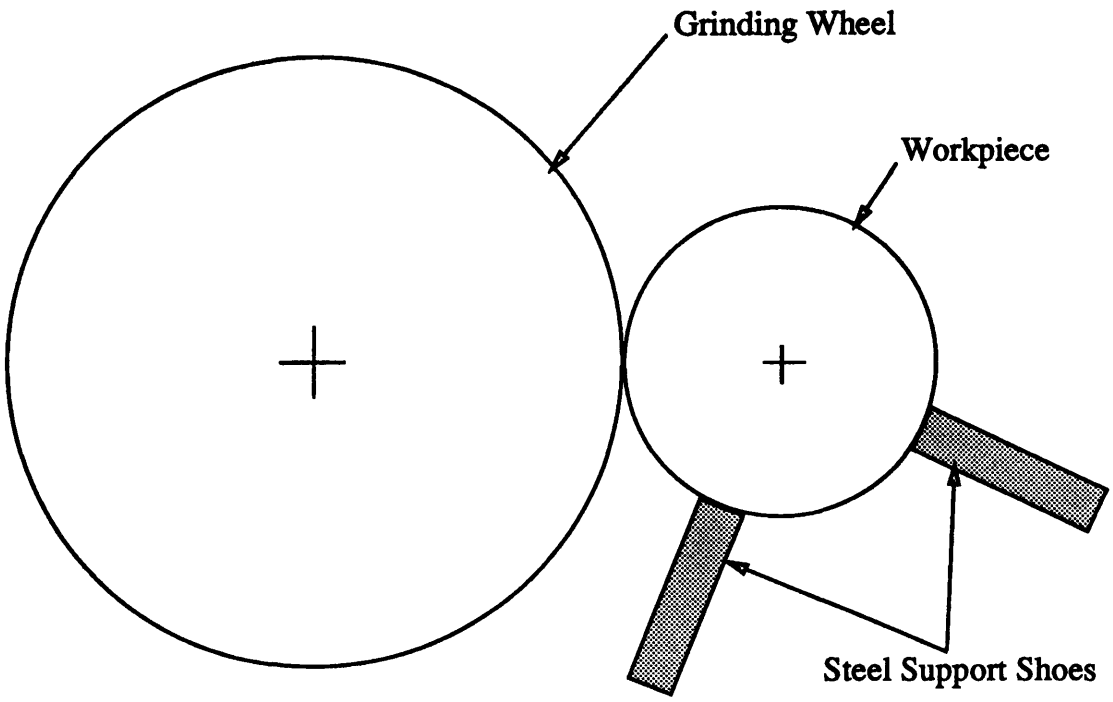

Figure 2-4: Shoe-type Centerless replaces the Regulating. Wheel with a Steel Shoe.

centerless grinding over a very limited range of set up conditions. This study will analyze a comprehensive geometric *and* dynamic model over a wide range of set up conditions. As noted above, this type of extensive study in centerless grinding has not before been published.

Chapter 3

The Centerless Grinding Model

When grinding circular cross sections, the variables of interest are the total stock removal and rate, the final roundness accuracy, and the surface finish of the workpiece. Hahn[14] has shown that stock removal is proportional to normal grinding force. Workpiece roundness accuracy is caused by deviations in stock removal, or variations in grinding force. Surface finish is is controlled by the workpiece and grinding wheel materials, the stock removal rate, and the relative velocity between the work and the wheel. The main variable for analysis of grinding is often the grinding force.

Two types of analysis must be completed to characterize the forces found in grinding. First, the static forces of gravity, constant feed force, and constant rotational torque must be considered for a steady state process. Secondly, since grinding is a dynamic process and includes transient forces, a dynamic model must be developed and analyzed. This study will propose a dynamic model which can be used to predict *both* the static (geometric) and dynamic stability of the shoe type centerless grinding process.

3.1 Static Force Analysis

Although most of the forces of interest in centerless grinding are transient, it is worthwhile to investigate the static, or steady state, forces. Figure 3.1 shows a diagram of the shoe-type centerless grinding process with the forces on the workpiece.

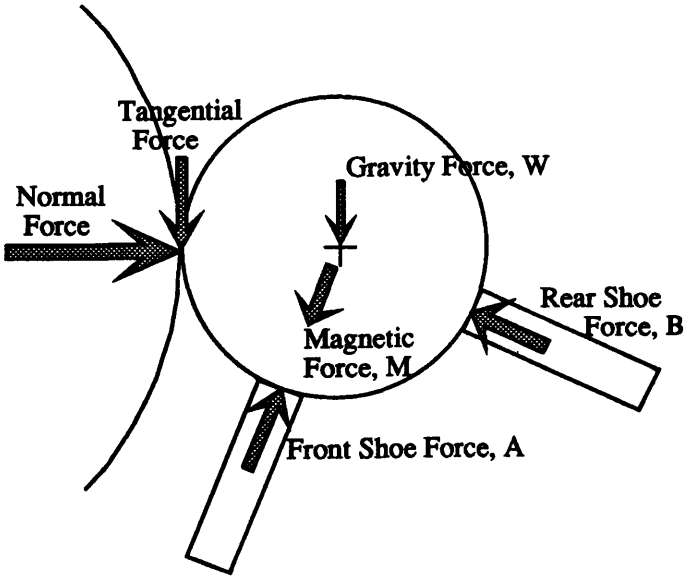

Figure 3-1: Diagram of force on the workpiece in Shoe-type Centerless Grinding.

The tangential shoe forces were neglected since they are not significant compared to the other forces on the workpiece. The normal and tangential grinding forces along with the weight of the workpiece create reactionary forces from the shoes to maintain the static balance of the system. Previous research has show that the tangential grinding force is approximately half of the normal grinding force, though the exact value likely varies between various grinding wheels.

In shoe-type centerless grinding the workpiece back face is held with a rotating magnetic chuck. This magnetic plate is used primarily to prevent the workpiece from rotating at the same speed as the grinding wheel. The workpiece speed is controlled by the rotational speed of the magnetic chuck which creates relative velocity between the workpiece and grinding wheel surfaces. The magnetic force between the chuck and the workpiece must be great enough to provide static friction between their faces yet small enough to prevent interference with the three point contact geometry of the centerless grinding process. For example, if the magnetic force were too great then the shoes would have virtually no effect and the process would become like center-type grinding. Often, the center of the magnetic force is displaced slightly from the

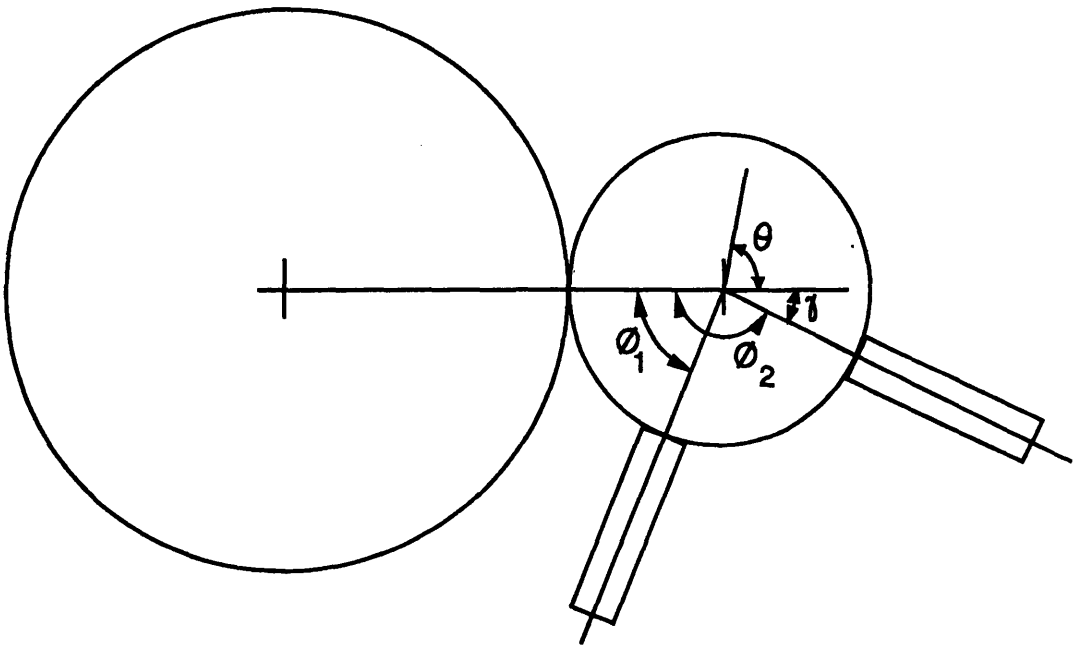

Figure 3-2: Shoe-type Centerless Grinding Geometric Angle Characterization.

center of the workpiece toward the front shoe to assure that the workpiece is always in contact with the shoes, as depicted in Figure 3.1.

Shoe-type centerless grinding is characterized by two separate angles, ϕ_1 and ϕ_2. Figure 3.2 shows the configuration for centerless grinding. As can be seen, ϕ_1 is the angle between the grinding wheel contact point and the front shoe contact point, typically near 60 degrees. ϕ_2 is the angle between the grinding wheel contact point and the rear shoe contact point, often between 155 and 180 degrees. The angle, γ is defined as $180-\phi_2$, and is called the center-height angle in wheel-type centerless grinding. For this horizontal infeed grinding configuration, ϕ_1 must be less than 90 degrees and $\phi_2-\phi_1$ must be less than 180 degrees from the simplest geometric criteria.

If the forces in Figure 3.1 are balanced in the horizontal and vertical directions, then:

$$\sum F_{horz} = F_n + Acos(\phi_1) - Bcos(\gamma) - \mu Mcos(\theta) = 0. \qquad (3.1)$$

$$\sum F_{vert} = -F_t - W + Asin(\phi_1) + Bsin(\gamma) - \mu Msin(\theta) = 0. \quad (3.2)$$

where μ is the coefficient of friction between the magnetic face plate and the workpiece back face, and θ is the offset angle of the magnetic force. The weight, W, in equation 3.2 can often be neglected when compared to the other forces in the system. Since γ is often small compared to ϕ_1, most of the normal grinding force is offset by the rear shoe (force B) and the magnetic face force. The tangential grinding force and the vertical component of the magnetic face force are primarily offset by the front shoe (force A). If W is neglected and F_t/F_n is approximately 1/2, then equations 3.1 and 3.2 combine to show:

$$A = (\frac{tan\gamma}{tan\gamma + tan\phi_1})(\frac{1 - 2tan\gamma}{2tan\gamma cos\phi_1})F_n + (\frac{tan\gamma}{tan\gamma + tan\phi_1})(\frac{sin\theta + tan\gamma cos\theta}{tan\gamma cos\phi_1})\mu M. \quad (3.3)$$

Summing the torque around the workpiece center to establish rotational acceleration yields:

$$\sum \tau = -F_t R + \mu_s AR + \mu_s BR + \mu Mr = 0. \quad (3.4)$$

If the magnetic force is applied at the circumference of the workpiece, then r=R and the radius vanishes from the equation. The shoes are often made of hardened steel, so the sliding coefficient of friction, μ_s, between the workpiece and shoes is typically quite low. For simplification, if μ_s is zero, then μM must be equal to or greater than the tangential grinding force to maintain relative rotational velocity between the workpiece and grinding wheel during grinding.

It is quite possible that γ could be increased enough with a constant magnetic plate force where the normal grinding force would not be balanced allowing the workpiece to be pushed away from its grinding position. In order to prevent this from occurring, the moment around the rear shoe must be balanced. Summing the moments around the rear shoe contact point from Figure 3.1 results in:

$$\sum M_B = F_n Rsin\gamma - WRcos\gamma - F_t R(1+cos\gamma) + ARsin(\phi_1+\gamma) - \mu MRsin(\theta+\gamma) < 0. \quad (3.5)$$

Therefore, using equations 3.3 and 3.5, the required magnetic force can be calculated

in terms of the grinding force for actual processing depending on the set up conditions, ϕ_1, ϕ_2 (180-γ), and the choice of magnetic plate offset, θ.

It should be clear that this static analysis is only a preliminary step in the actual grinding analysis. Grinding is a very dynamic process requiring a transient model for meaningful study of accurate workpiece production techniques.

3.2 Transient Force Analysis

The transient grinding force depends on the initial workpiece roundness, the grinding wheel infeed rate, the geometric set up condition (the shoe angles), and the machine vibration. No workpiece is perfectly round, and grinding the piece can increase or decrease workpiece roundness. Throughout this analysis, workpieces will be considered in terms of roundness, meaning the degree of out-of-round, since attempting to generate a perfectly round piece with a grinding machine would be most difficult in high-speed production.

The model of centerless grinding is developed by analyzing the instantaneous grinding force during processing. If a rigid machine is initially assumed, then only the geometry of the process is important. The instantaneous force can be derived by combining the initial workpiece lobing and and current workpiece angular position (accounting for both shoes) to find the current depth of cut. Analysis of a single lobe on the workpiece shows that the instantaneous grinding force will be influenced by the lobe as it passes over the front shoe then the rear shoe and then again as it encounters the grinding wheel after one full revolution. These three geometric effects can be considered as three time delays in a mathematical model. Therefore, at any instant, the theoretical depth of cut can be found by knowing only the initial workpiece roundness and the time elapsed during grinding (assuming constant rotational velocity). The theoretical depth of cut can be converted into grinding force by knowing the cutting stiffness of the grinding wheel. Relaxing the assumption of a rigid machine allows changes in the instantaneous depth of cut due to flexing of the machine.

This study proposes a model which accounts for the the transient forces found in

centerless grinding including: the time variation in workpiece roundness, the lobing time delays, the grinding force, and the machine vibration. Figure 3.3 shows the proposed model of centerless grinding. The command infeed combines with the machine vibration and with the grinding wheel roundness to form the actual displacement infeed of the grinding wheel. The grinding wheel infeed and the effects of the two shoe positions combine with the workpiece deviation from round to give the depth of cut into the grinding wheel. The depth of cut combines with the cutting stiffness of the grinding wheel to give the instantaneous normal grinding force. The grinding force feeds back into the machine and grinding wheel which in turn effect the actual infeed as previously mentioned.

The time delay effects in the model have fairly simple origins. If one bump or lobe on the workpiece is studied, there is a time delay (the workpiece angular velocity times the included angle ϕ_1) for the lobe to travel from the grinding wheel to the front shoe. As the bump encounters the front shoe, the workpiece moves up (parallel to the back shoe face) and away from the grinding wheel, as shown in Figure 3.4. Figure 3.5 depicts the geometric effect on the grinding wheel of a lobe on the front shoe. In equation form, the horizontal displacement of the workpiece center due to a unit bump is:

$$a = \frac{sin(\phi_2)}{sin(\phi_2 - \phi_1)} \tag{3.6}$$

Similarly, there is a second delay as the lobe travels to the second shoe. Derived geometrically in Figure 3.6, as the bump hits the second shoe it forces the workpiece into the grinding wheel parallel to the front shoe leading to an increase in grinding force. The horizontal displacement is termed, b, and is similar in form to the front shoe factor, a, for a unit size lobe:

$$b = \frac{sin(\phi_1)}{sin(\phi_2 - \phi_1)} \tag{3.7}$$

The workpiece also has a third delay effect, termed regeneration. As the lobe

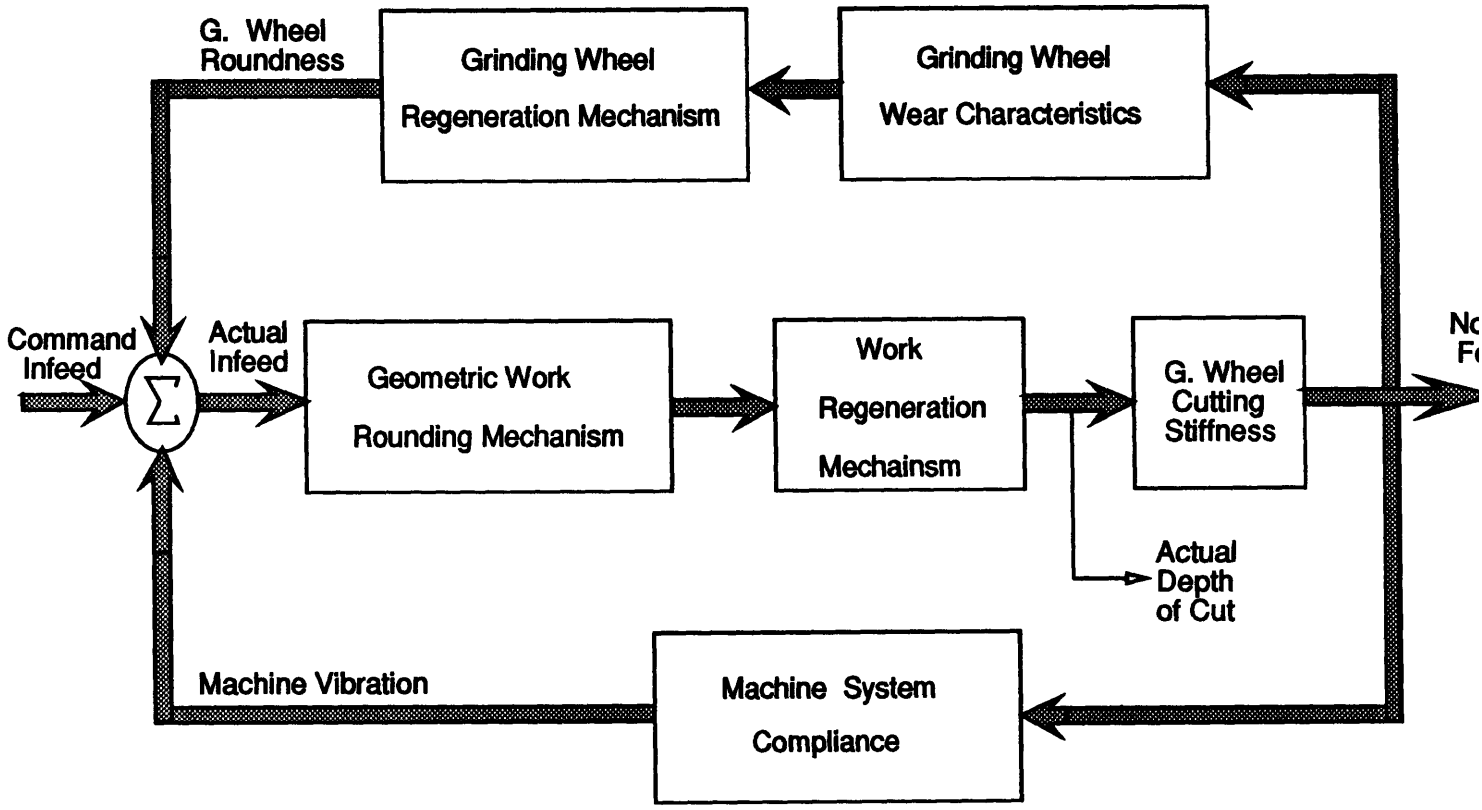
G. Wheel Roundness
Grinding Wheel Regeneration Mechanism
Grinding Wheel Wear Characteristics
Command Infeed
Actual Infeed
Geometric Work Rounding Mechanism
Work Regeneration Mechainsm
G. Wheel Cutting Stiffness
Actual Depth of Cut
Machine Vibration
Machine System Compliance

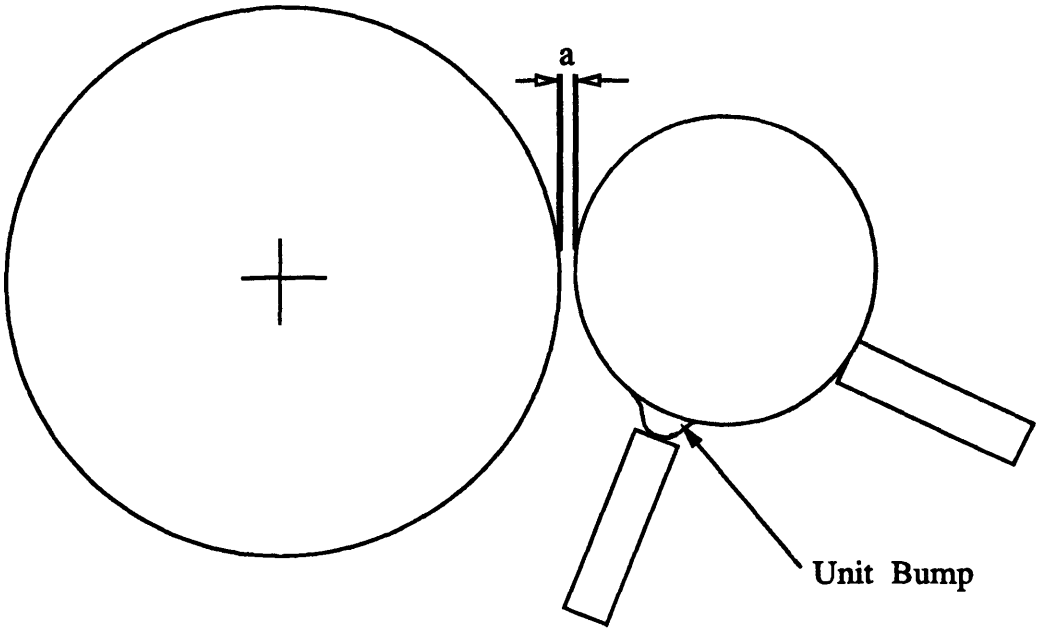

Figure 3-4: Diagram Showing a lobe on the front shoe pushing the workpiece away from the grinding wheel parallel to the back shoe.

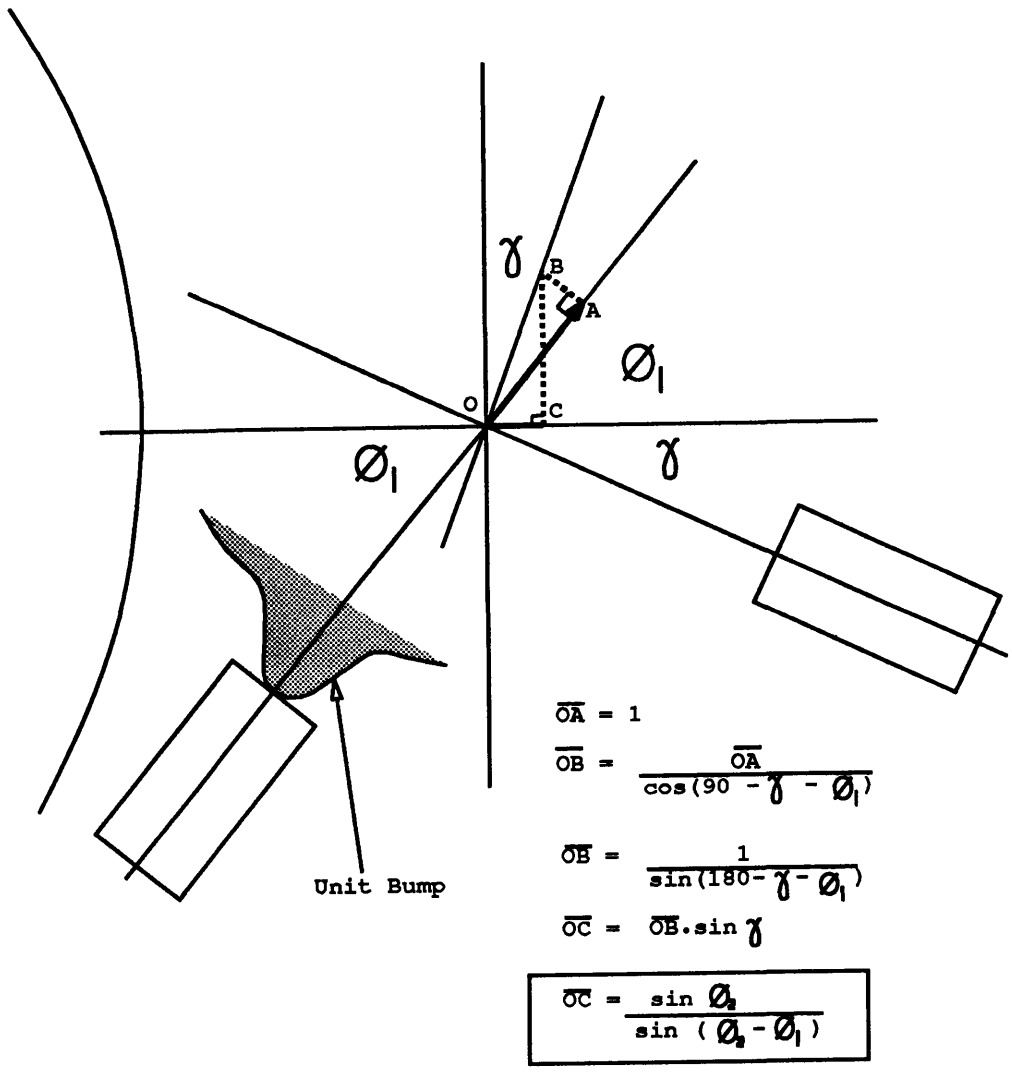

Figure 3-5: Geometric Effect of Front Shoe lobe on Grinding Depth of Cut.

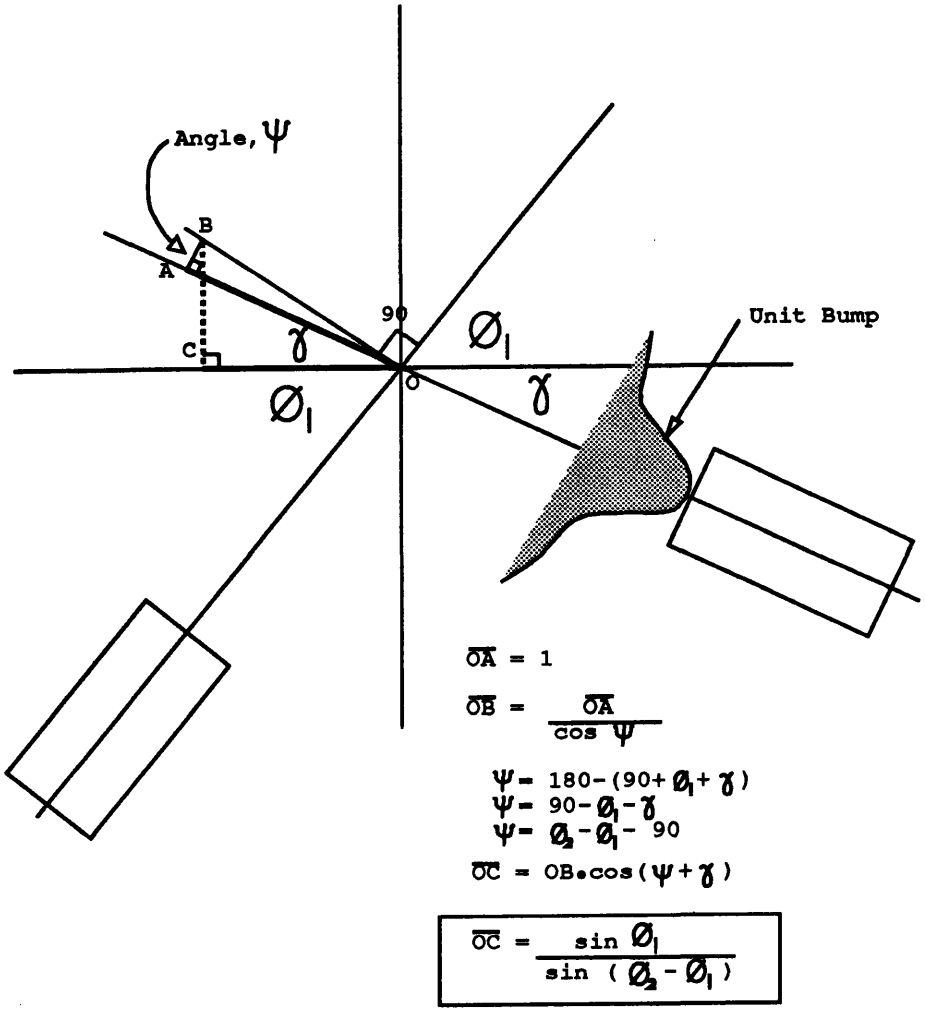

Figure 3-6: Geometric Effect of Rear Shoe lobe on Grinding Depth of Cut.

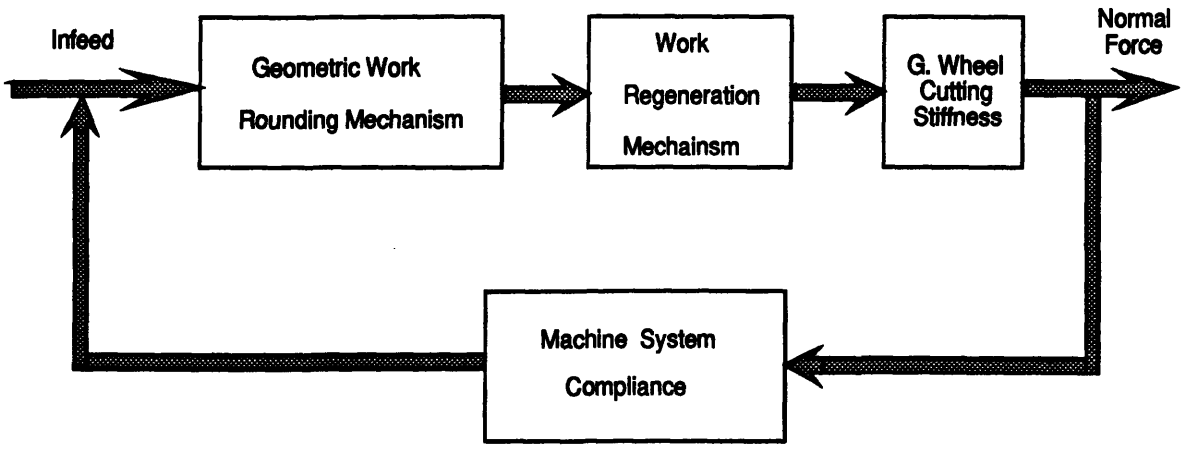

Figure 3-7: Effective model for Transient Analysis of Centerless Grinding.

rotates a full 360 degrees back to the grinding wheel, the instantaneous depth of cut is affected by the lobe which was a result of the previous revolution. Since grinding force depends on the depth of cut, a bump or lobe will cause an increase in grinding force while a depression or valley will cause a proportional decrease in force.

Separately, the grinding wheel has its own regeneration effect based on the transient worn roundness of the wheel. Hashimoto and others have determined that the grinding wheel regeneration effect often takes several minutes to significantly effect the grinding process, while workpiece regeneration takes only seconds to affect the process. Because of the large difference between transient growth rates, the grinding wheel regeneration effect will be neglected as insignificant compared to workpiece effects. For this analysis, then, the grinding wheel will be assumed perfectly round with even wear characteristics.

To allow for a simpler model, the grinding wheel cutting stiffness will be assumed constant for this analysis. Hashimoto et al[23] have shown that the cutting stiffness of the grinding wheel depends non-linearly on the grinding wheel loading; though, for constant stock removal rates, a constant cutting stiffness can be assumed. Also, the machine will be discretized to a finite number of linear mass, spring, and dashpot elements for simple dynamic analysis.

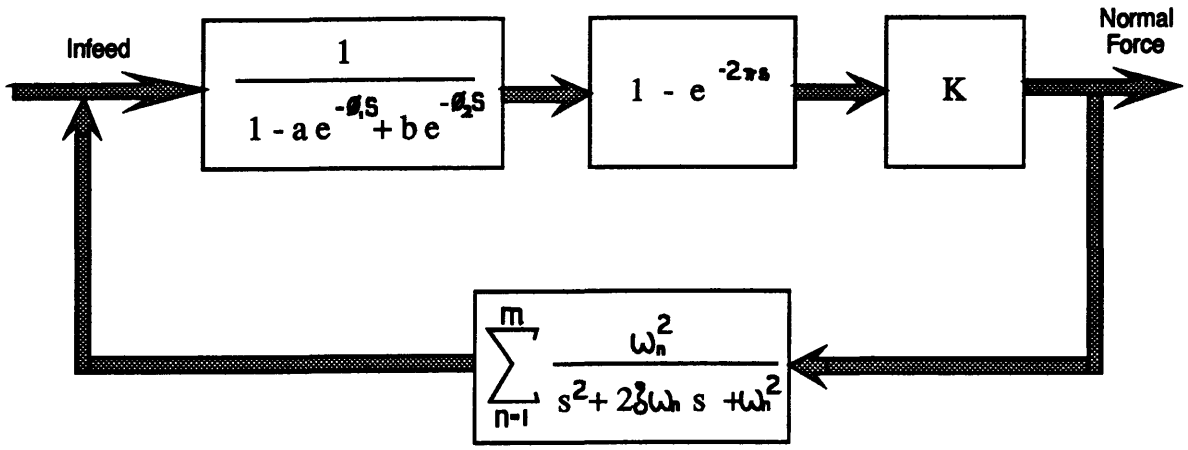

Figure 3-8: Model in Laplace Equation Block Form.

Figure 3.7 shows the simplified model of the centerless grinding system in symbolic form. Figure 3.8 shows the model in Laplace equation form where the input variables are the command feed rate, the two shoe angles (ϕ_1 and ϕ_2), and the initial workpiece roundness.

The strategy for analysis in this study will be to decompose the model into sections, analyze each section, then combine them together to form conclusions. The top section of the model alone (when the machine feedback is zero) represents a purely geometric analysis of the system. The top section will be analyzed and conclusions based strictly on the geometry of the process will be drawn first. Then, the machine stiffness will be relaxed from infinity and the vibration dynamics of the process will be analyzed for varying levels of instability based on set up condition geometry.

Chapter 4

Geometric Theory and Equations

The proposed model uses Laplace operators to aid in the analysis of the centerless grinding system. Figure 4.1 shows the block diagram reduction of the system. To solve the system's characteristic equation,

$$1 + G(s) * H(s) = 0 \tag{4.1}$$

and find the stable and unstable roots, it is best to separate the geometry and machine effects by rearranging equation 4.1 as:

$$H(s) = -1/G(s). \tag{4.2}$$

For geometric analysis, the machine is assumed to be infinitely stiff. In equation 4.2, this translates to solving

$$-1/G(s) = 0. \tag{4.3}$$

Although the equations represented in Figure 4.1 can be solved through numerical methods, a graphical solution will be sought since it is more explanatory and intuitive.

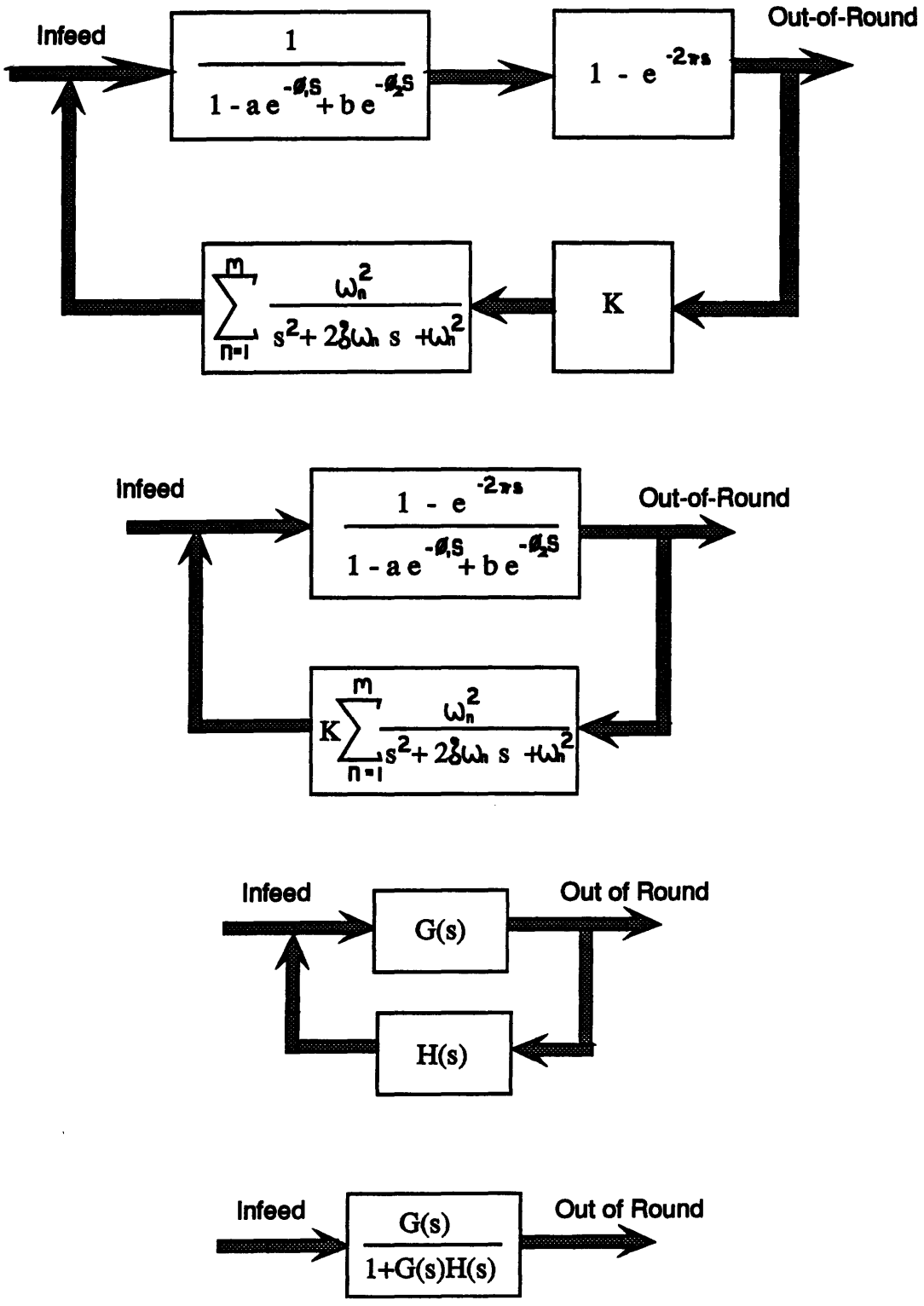

Figure 4-1: Block Diagram Reduction of Centerless Grinding Model.

4.1 Work Rounding Vector Locus

In the Laplace domain, a time delay is represented by an exponential function, $e^{-\theta s}$, where θ is the phase angle and s is the Laplace operator, $s = \sigma + jn$. Observing the part of equation 4.3 representing the work rounding vector locus in 1/G(s) form, the exponential phase shifts are the shoe angles ϕ_1 and ϕ_2:

$$1 - a * e^{-\phi_1 s} + b * e^{-\phi_2 s} \tag{4.4}$$

Since the Laplace operator, $s = \sigma + jn$, has both real and imaginary components, the exponentials in equation 4.4 are complex functions. It is necessary to recall from complex analysis that:

$$e^{\sigma + jn} = e^{\sigma}(cos(n) + jsin(n)). \tag{4.5}$$

For simpler analysis or 0graphical representation on the complex plane the function shown in equation 4.5 can be separated into its real and imaginary parts. If equation 4.4 is separated into its real and imaginary components like equation 4.5, then:

$$Re(rnd) = 1 - a * e^{-\sigma\phi_1} cos(n\phi_1) + b * e^{-\sigma\phi_2} cos(n\phi_2) \tag{4.6}$$

$$Im(rnd) = a * e^{-\sigma\phi_1} sin(n\phi_1) + b * e^{-\sigma\phi_2} sin(n\phi_2) \tag{4.7}$$

These equations can be analyzed at varying σ, n, ϕ_1, and ϕ_2 with the factors a and b as shown in equations 3.6 and 3.7.

Stability analysis is simplest when observed from the stability limit of $\sigma = 0$ in $s = \sigma + jn$. This approach reduces equations 4.6 and 4.7 to:

$$Re(rnd) = 1 - a * cos(n\phi_1) + b * cos(n\phi_2) \tag{4.8}$$

$$Im(rnd) = a * sin(n\phi_1) + b * sin(n\phi_2) \tag{4.9}$$

For any given set up condition, the angles ϕ_1 and ϕ_2 will be constant, so equations 4.8 and 4.9 can be plotted on the complex plane as simply a function of the frequency,

n. Since the real part of the function is 1 minus cosine functions, and the imaginary part of the function is sine functions, the complex plot should be something similar to circles centered around the point (1,0). Figure 4.2 shows these 'circles' for one particular setup condition and frequencies 2 through 30. Integer frequencies, lobe numbers n, are plotted for lobes 2-4 to aid in graphical understanding.

For different set up conditions, the circular trends shown in Figure 4.2 remain the same though their orientation changes slightly. If there were interest in only the rounding mechanism without the effect of the grinding wheel, then stability and instability trends would be worth pursuing at this stage. But, since the geometry of the system must include the interaction with the grinding wheel to have meaningful conclusions, the pursuit of independent stability trends in the rounding mechanism alone will not be presented here. Researchers such as Bueno, Modler, and others have pursued this avenue, though it yields little physical explanation of the process since the analysis neglects the existence of the 360 degree full rotation delay of the workpiece.

Normally in the complex plane, a function with a positive σ component would imply that the function was unstable, but equation 4.3 called for -1/G(s) while Figure 4.2 shows part of 1/G(s) implying that the left half of the complex plane is unstable in this case. Later in this analysis, the regeneration mechanism will take the minus sign from equation -1/G(s), allowing a positive sign in this section. Since equation 4.3 called for the entire block, G(s), the rounding mechanism must be combined with the regeneration mechanism for meaningful analysis.

Later it will be seen that slight changes in sigma from the stability limit of $\sigma = 0$ will result in small changes in the size of the work rounding 'circles'. Positive sigma will increase the size of the circles while negative sigma will decrease their size.

It would be useful to note the importance and trends of the factors a and b. The factors a and b in equation 4.4 represent the effect of a lobe on the depth of cut from the front and rear shoes, respectively, as discussed in section 3.2. As ϕ_1 or ϕ_2 increase in the normal grinding range (ϕ_1=40-90, ϕ_2=150-180), the factor b becomes larger while a becomes smaller. In wheel-type centerless grinding ϕ_2 is often proportionally

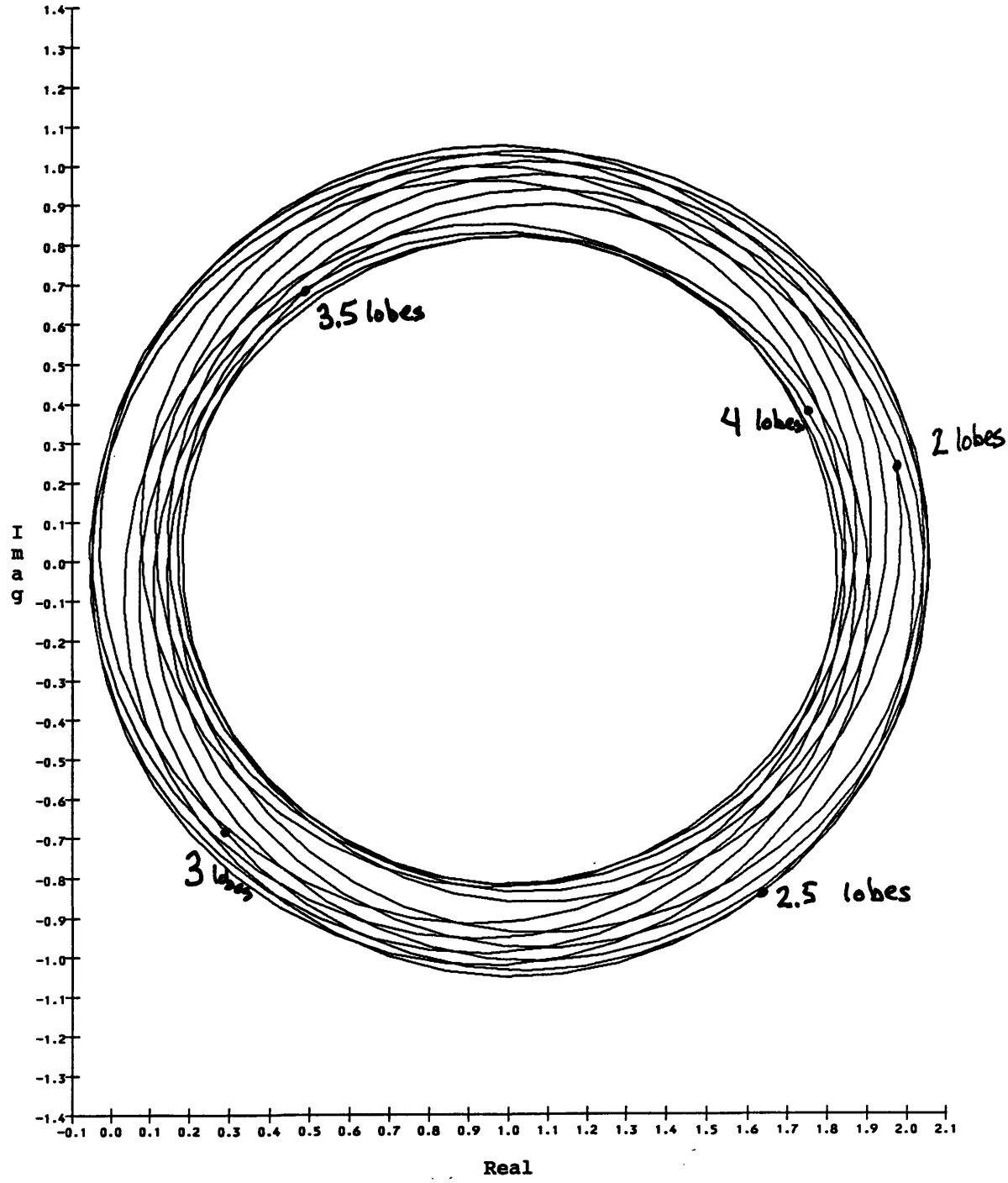

Figure 4-2: Work Rounding Vector Locus 'Circles' for one set up condition.

large so the effect of ϕ_1 is sometimes neglected. When the whole grinding range is considered as in shoe-type centerless grinding, the factor a cannot be neglected.

4.2 Regeneration Vector Locus

The 360 degree rotation of the workpiece back to the grinding wheel represents the third time delay in the proposed model. The regeneration mechanism is important because the instantaneous depth of cut will depend greatly on the amount of stock on the piece at the grinding wheel which was caused by the previous rotation's cut. Similar to the work rounding mechanism, equation 4.3 is shown in terms of the regeneration function (with the minus sign from -1/G(s)) as:

$$\frac{-1}{1-e^{-2\pi s}} \tag{4.10}$$

Since the complex Laplace operator, $s = \sigma + jn$, is in the denominator, equation 4.10 should be multiplied by the denominator's complex conjugate for separation into real and imaginary parts. This manipulation and separation results in:

$$Re(rgn) = \frac{-1 + e^{-2\pi\sigma}cos(2\pi n)}{1 + e^{-4\pi\sigma} - 2e^{-2\pi\sigma}cos(2\pi n)} \tag{4.11}$$

$$Im(rgn) = \frac{e^{-2\pi\sigma}sin(2\pi n)}{1 + e^{-4\pi\sigma} - 2e^{-2\pi\sigma}cos(2\pi n)} \tag{4.12}$$

For geometric analysis at the stability limit $\sigma = 0$, equations 4.11 and 4.12 reduce to simply:

$$Re(rgn) = -1/2 \tag{4.13}$$

$$Im(rgn) = \frac{sin(2\pi n)}{2 - 2cos(2\pi n)} \tag{4.14}$$

Equation 4.14 varies from positive infinity at integer numbers of n (5.000, 6.000, etc.) to negative infinity at numbers just less than integer (5.999, 6.999, etc.). As sigma changes from the stability limit of $\sigma = 0$, the regeneration mechanism folds in on itself and forms circles. Slight variations in sigma greatly affect the size of these

circles which will become important when the machine stiffness is addressed.

4.3 Combining the Work Rounding and Regeneration Vector Locus

In the Laplace domain, combining the work rounding mechanism and the regeneration mechanism requires simple equation multiplication. For graphical analysis, the combined mechanism effect is found through vector multiplication at matching $s = \sigma + jn$. For this method, a vector from the origin to both the rounding and regeneration mechanisms is found at the same frequency and sigma (here, $\sigma = 0$). In vector multiplication, the magnitude of each vector is multiplied and the angles from the positive real axis are summed. For example, Figure 4.3 depicts a typical vector multiplication at the frequency n=7.5. As can be seen, the work rounding vector has a magnitude of 2 and an angle of -45 degrees while the regeneration vector has a magnitude of 3 and an angle of 120 degrees. The combined vector for this condition is shown in Figure 4.4 where the magnitude of the n=7.5 vector is 6 (2*3) and the angle is 75 degrees (120+ −45). Part of the vector locus for lobes from 6 to 8 is shown here to depict the general pattern of the combined vector locus for varying lobes and set up conditions.

Figure 4.5 shows sample points of the combined work mechanism locus for 2 through 10 lobes at a particular set up condition. These hyperbola shaped loci are centered around the point (−.5,0) in the complex plane and have infinite asymptotes covering the range from 0 to 360 degrees. The asymptotes have an imaginary components starting at positive infinity for integer numbered frequencies (5.000, 6.000, etc.) and ending at negative infinity for numbers just less than integer (5.999, 6.999, etc.). The characteristic that varies most for these loci is the angular orientation of the asymptotes. It will be proposed that asymptotes near 0 degrees imply geometric instability.

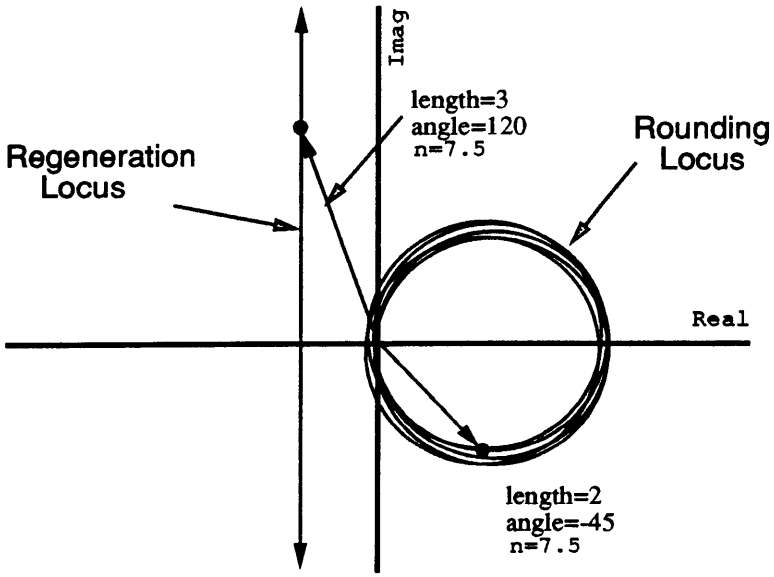

Figure 4-3: Vector Multiplication for a sample frequency at the stability limit.

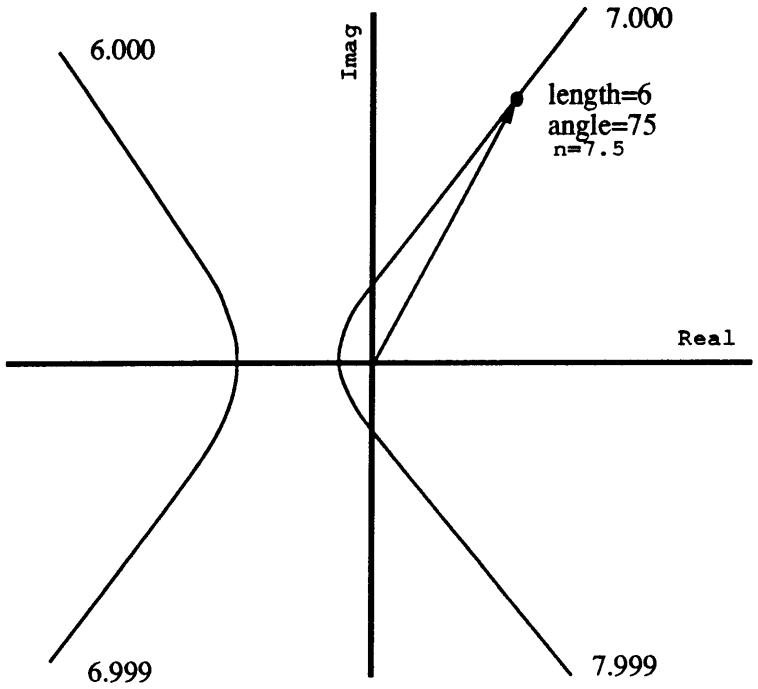

Figure 4-4: Combined Vector Locus for 6 to 8 lobes at a sample set up condition.

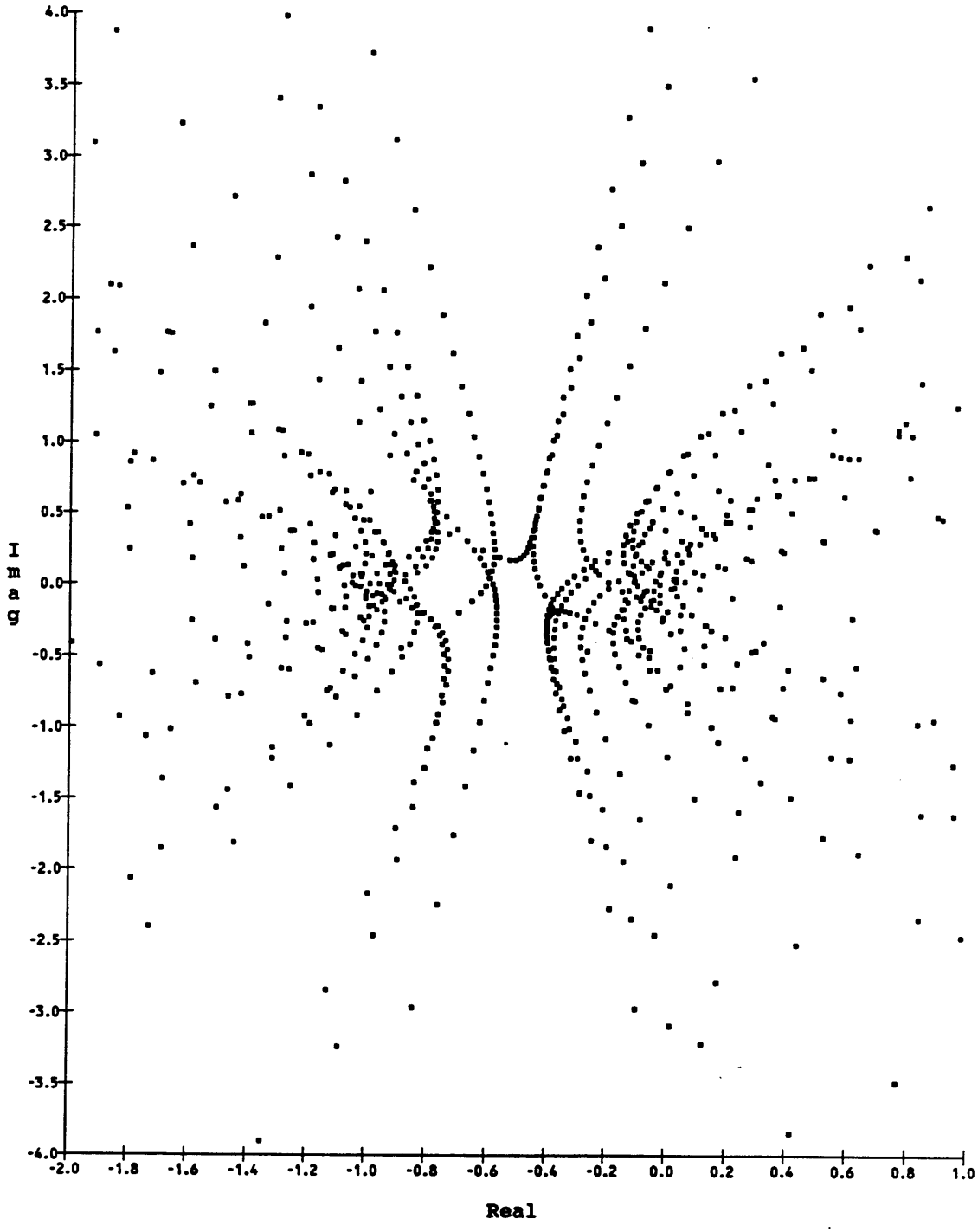

Figure 4-5: Points from the combined work mechanism vector locus for a range of lobes at a sample set up condition. The asymptote angles vary widely.

4.4 Geometric Lobing Instability

The hyperbola shaped rounding and regeneration vector loci found in Section 4.3 vary predictably in their asymptote angles. Figure 4.6 shows the asymptote angle trends for a particular set up condition with varying lobes. As can be seen the asymptotes follow the basic trend of increasing about 2.5 degrees per lobe with odd and even, integer and near integer lobes grouped together approximately 180 degrees apart. Figure 4.7 shows the trends of the asymptote angles with changing ϕ_2 for a few lobe numbers at a constant front shoe angle, ϕ_1=55 degrees. This graph shows a decrease in asymptote angle with increasing ϕ_2, but it also shows odd and even, integer and near integer asymptote angles which fall approximately 180 degrees apart.

Since the asymptote angles follow clear patterns, interpretation of the angles would be beneficial in understanding the geometric process of centerless grinding. Two possible interpretations are proposed. The first requires an in depth look at the vector multiplication of the rounding and regeneration vector loci. The second possible interpretation of asymptote angles comes from observing the graphical coincidence of the regeneration and rounding mechanisms combined vector locus with the vector locus of an infinitely stiff machine.

In section 4.1 the work rounding mechanism was found to be unstable when the vector locus had a negative real part. The vector angle of an unstable rounding mechanism locus will be greater than 90 or less than -90 degrees from the positive real axis. Since the regeneration vector locus also lies in same region, its vector angle will be similar at the same frequency. When the rounding and regeneration mechanisms coincide at a particular frequency, that is their geometric angles cancel, then the combined vector locus will result in a hyperbola with a 0 degree (-360) asymptote. This mechanism coincidence implies geometric instability of an asymptote's particular lobe.

An infinitely stiff machine's vector locus is a point at the origin on the complex plane. Since the rounding and regeneration vector loci are centered around the point

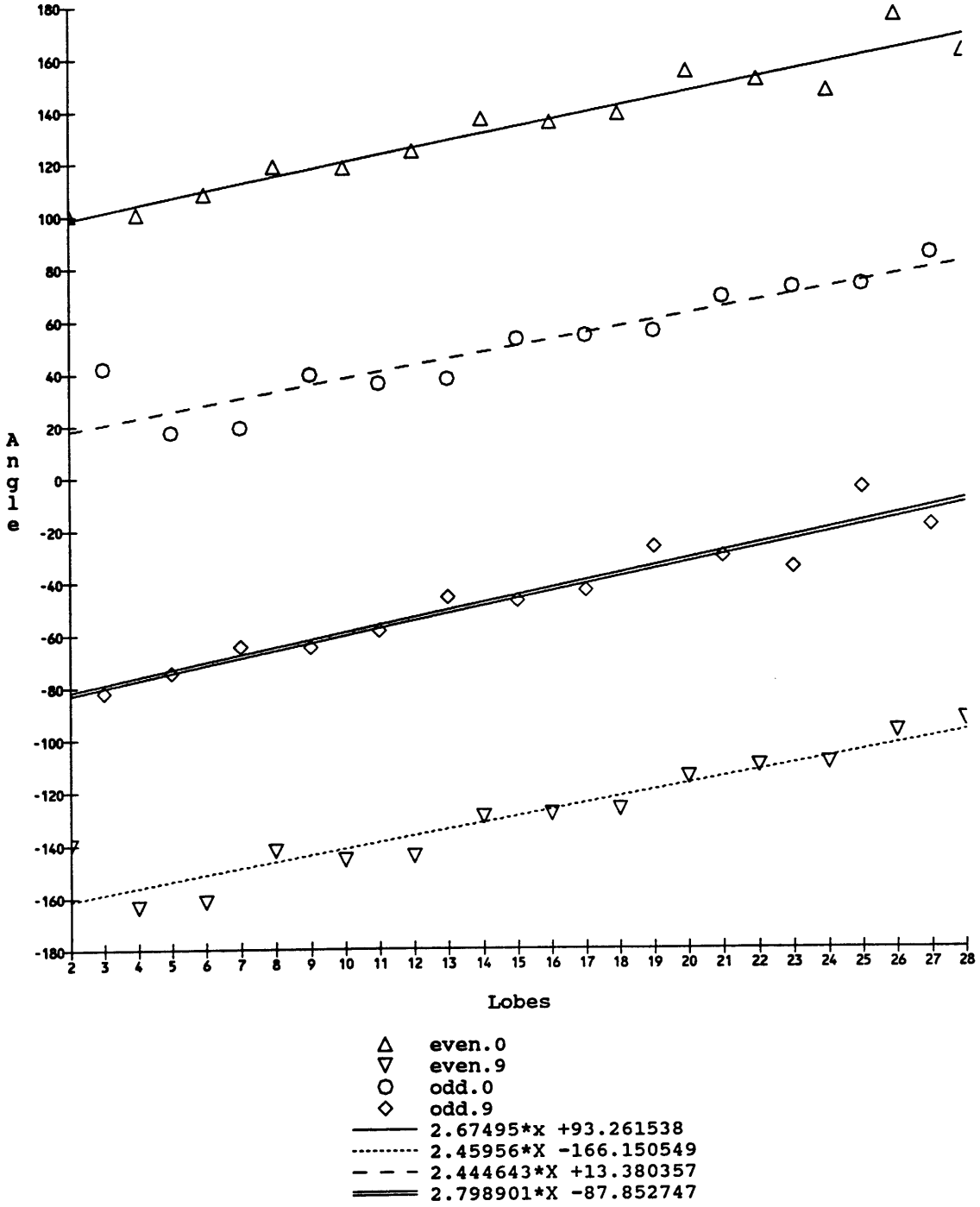

Figure 4-6: Combined Vector Locus Asymptote Angle trends with changing frequency.

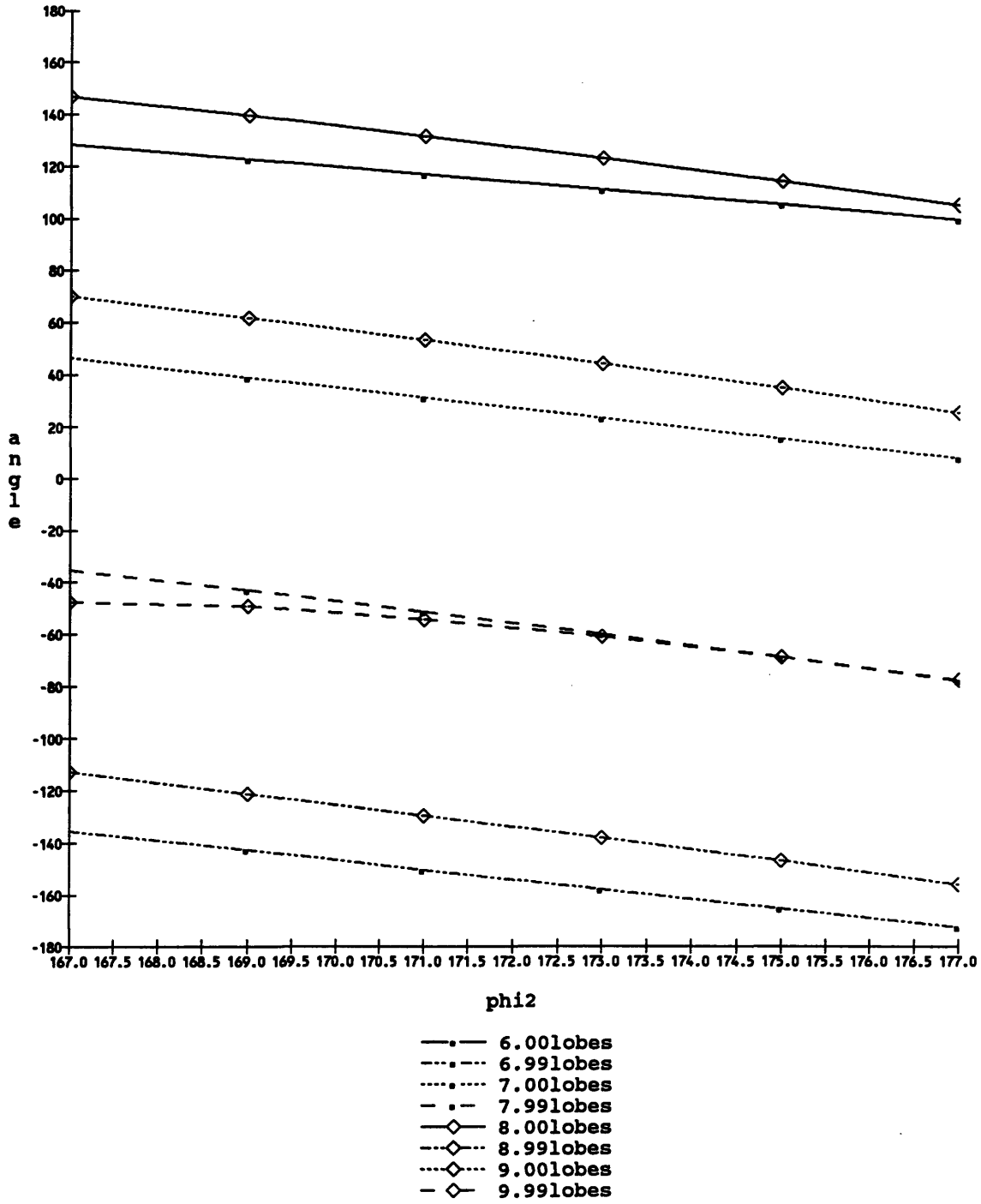

Figure 4-7: Combined Vector Locus Asymptote Angle trends with changing rear shoe angle.

(−.5,0), any particular vector locus which had an asymptote at 0 degrees would likely intersect with the machine locus. Graphical coincidence results in a system mechanism matching effect for that particular lobing frequency allowing unstable growth of that lobe. This interpretation uses an infinitely stiff machine and therefore implies geometric instability of lobing frequency based on vectoral coincidence in the complex plane.

Since asymptote angles depend on lobe number and set up geometry, it is possible to predict, given the above analysis, which lobes will be unstable over a range of set up conditions. If one lobe number's asymptote angle is observed over an entire range of set up geometries, then the theoretical geometric instability of that lobe number will be seen when the asymptote angle is a multiple of 2π radians. Figure 4.8 shows a contour plot of the asymptote angle in radians for 14 lobes in the normal range of centerless grinding set up geometry. As can be seen, the angular shift from 2π to 0 radians results in a high density of contours making it easy to see the areas where the asymptotes are at multiples of 2π. This plot shows that 14 lobes is theoretically unstable near ϕ_1=52 and 78 degrees and ϕ_2=143 and 168 degrees. Although only one line in each of these regions will be exactly at 0 degrees, unstable lobing often occurs at numbers slightly away from integer due to a phase shift in lobe regeneration in grinding. Therefore, it is best to look only at the general region where the integer lobe is unstable. For example in Figure 4.8 an ellipse can be drawn around the area of concentrated contour lines to represent the general area where 14 lobes is theoretically unstable. If these ellipses are compiled for all lobe numbers of interest, a stability chart will be formed.

Figure 4.9 shows a comprehensive plot of lobing geometric instability for 2 through 22 lobes over the normal range of centerless grinding based on asymptote angles. It shows that most of the grinding region has some sort of geometric instability and that the instability of lobes follows a pattern. For example: 12 lobes is geometrically unstable near ϕ_1=60 and ϕ_2=165 degrees, 14 lobes is unstable up and to the left near 52 and 168 degrees, 16 lobes is up and to the left of that, etcetera. This chart allows grinding set up geometries to be selected which reinforce or reduce particular lobing

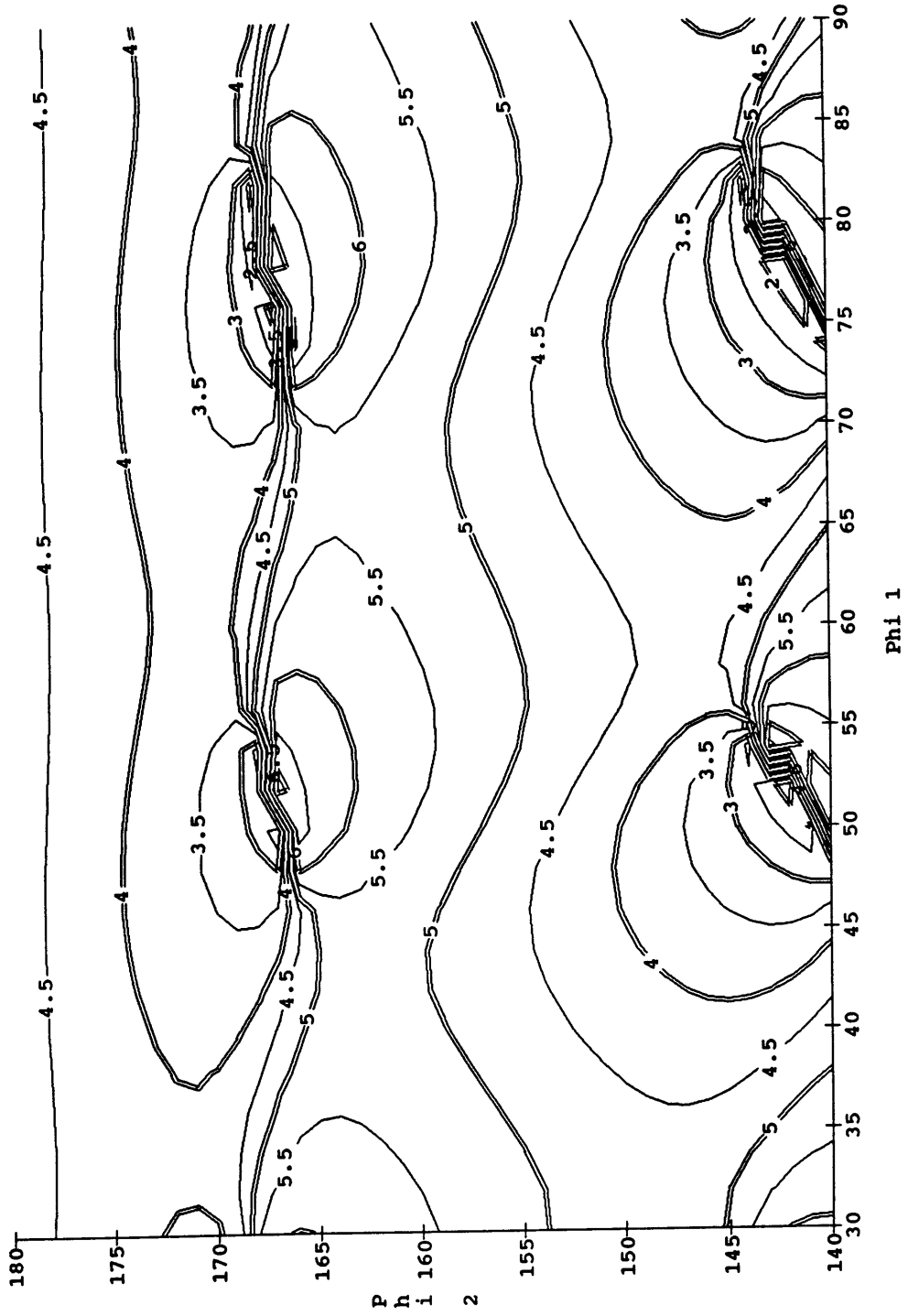

Figure 4-8: Contourplot in radians of asymptotic angles for 14 lobes in the normal grinding region

conditions.

Graphs similar to Figure 4.9 have been developed by other researchers, but the methodology and derivation presented here is new. Research by Chien, Dunbar, and others have proven the reliability of graphs quite similar to Figure 4.9. The data presented here is based on analysis in the Laplace domain and yields good predictions of geometric instability. As will be seen in section 6.2, the theoretical predictions presented here coincide well with experimental tests.

4.5 Geometric Stability Charts

In section 4.3 analysis was conducted in the Laplace domain at the stability limit of $\sigma = 0$ in $s = \sigma + jn$. It would be useful in grinding to compare set up geometries in terms of total level of instability instead of simply on/off stability as presented in section 4.4. Two methods of development will be pursued to estimate the overall geometric stability of each set up condition. Similar in mathematical analysis both yield basically similar predictions, though the first is at the stability limit of $\sigma = 0$ while the second assumes an infinitely stiff machine and some level of instability. The results of the two developments are slightly different in detail, and it will take experimental analysis to determine which method is preferable for the determination of workpiece roundness trends.

4.5.1 Angular Analysis Based Stability Chart

Section 4.4 concluded that when the combined rounding and regeneration mechanism locus for any lobe had an asymptote at 0 degrees, then that lobe was geometrically unstable. In the same analysis it was shown that the asymptote angles follow basic trends depending on set up condition. Given this fact, it is reasonable to infer that the closer an asymptote angle is to 0 degrees the less stable its lobe becomes.

Using this methodology, a summary plot can be found which suggests the degree of instability overall for each set up condition. To do this, a parameter was needed which was proportional to angle where angles near 0 or 2π were heavily weighted and

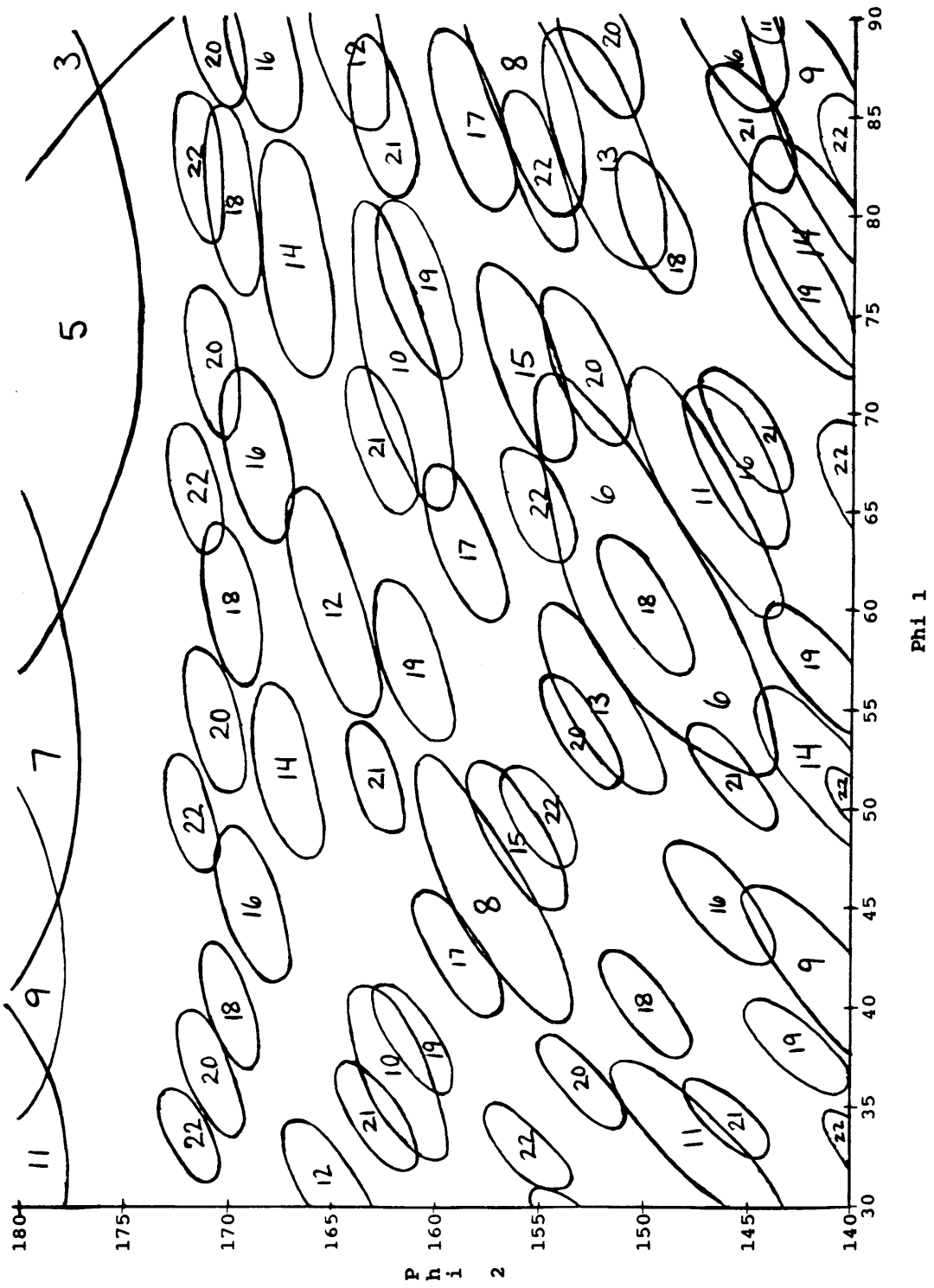

Figure 4-9: Geometric Lobing Instability Plot based on Angular Analysis of the Combined Vector Locus at the Stability limit in the normal grinding range.

angles far away from 0 or 2π were given little weight. The cosine function is a good candidate for such a weighting scheme. If the cosine of the radian values shown in Figure 4.8 are taken, then a plot results proposing the relative level of instability for 14 lobes at different set up conditions. On this plot, shown in Figure 4.10, contours with levels near zero (0.1, 0.2) are much more stable than levels near 1.0.

If the same analysis from Figure 4.10 is added for every lobe number from 2 through 30 in the normal grinding range, then a comprehensive geometric stability chart results as shown in Figure 4.11. Because of the weighting scheme selected, lower numbers on the plot imply improved geometric stability. As a rough interpretation of the plot, it can be seen that lower values of ϕ_1 and ϕ_2 result in greater geometric stability. It will be shown later that if the machine is dynamically stable in terms of vibration then a comprehensive plot of geometric stability should predict final part roundness trends based on set up geometry.

4.5.2 Non-zero Sigma, Diameter Based Stability Chart

When the combined rounding and regeneration vector locus is observed with a non-zero growth rate, sigma, then its graphical representation changes dramatically. As mentioned in section 4.2, non-zero sigma changes the regeneration vector locus from a straight line into circles as seen in Figure 4.12. With an increasingly positive sigma, the circles get smaller converging to the point (-1,0), while an increasingly negative sigma produces smaller circles converging to the origin. The size of the locus decays faster than an exponential function, so only it takes small values of sigma to change the shape of the combined rounding and regeneration vector locus significantly.

Figure 4.13 shows the combined vector locus of the rounding and regeneration mechanisms with varying positive sigma for 6.000 to 7.999 lobes at a given set up condition. Roughly, it can be seen that the hyperbola wraps around itself to form looping spirals. Figure 4.14 shows these same looping spirals with varying negative sigma. Negative sigma causes the spirals to wrap around themselves in the opposite direction, maintaining their size but changing their orientation. Different set up con-

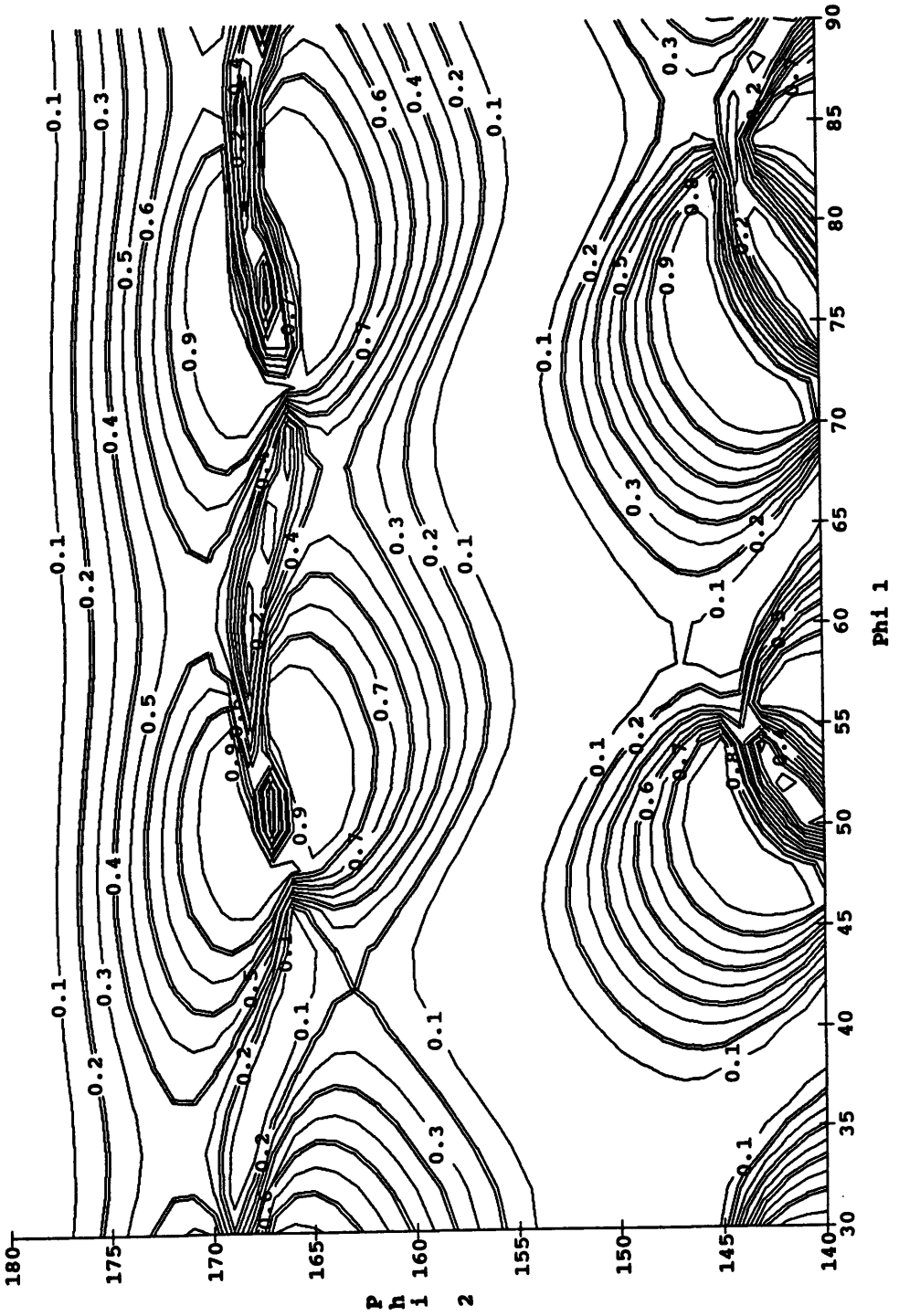

Figure 4-10: Contourplot of Cosine of asymptotic angles for 14 lobes in the normal grinding region.

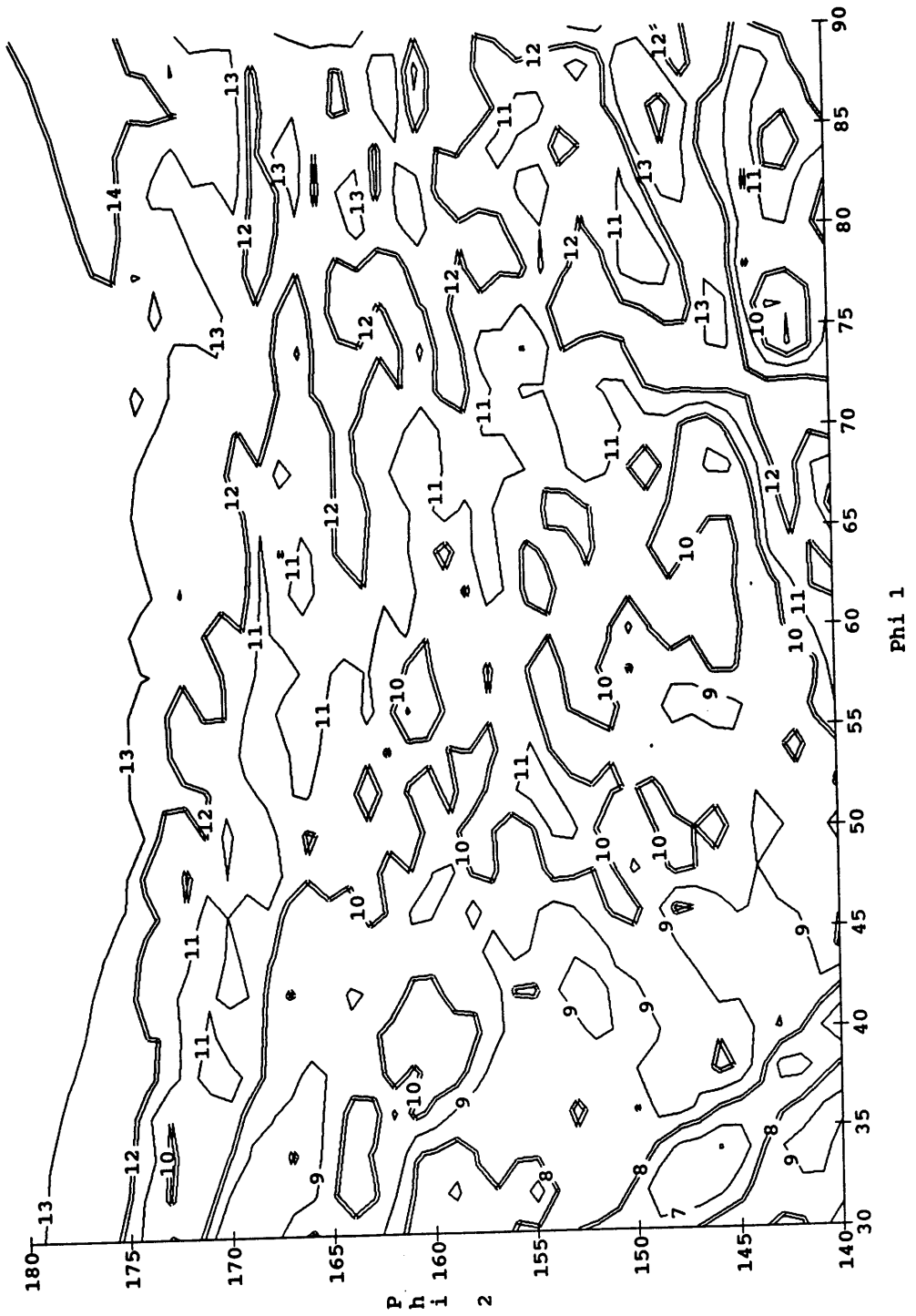

Figure 4-11: Contourplot of sum of Cosine of Asymptote Angles for 2-30 lobes in the normal grinding region.

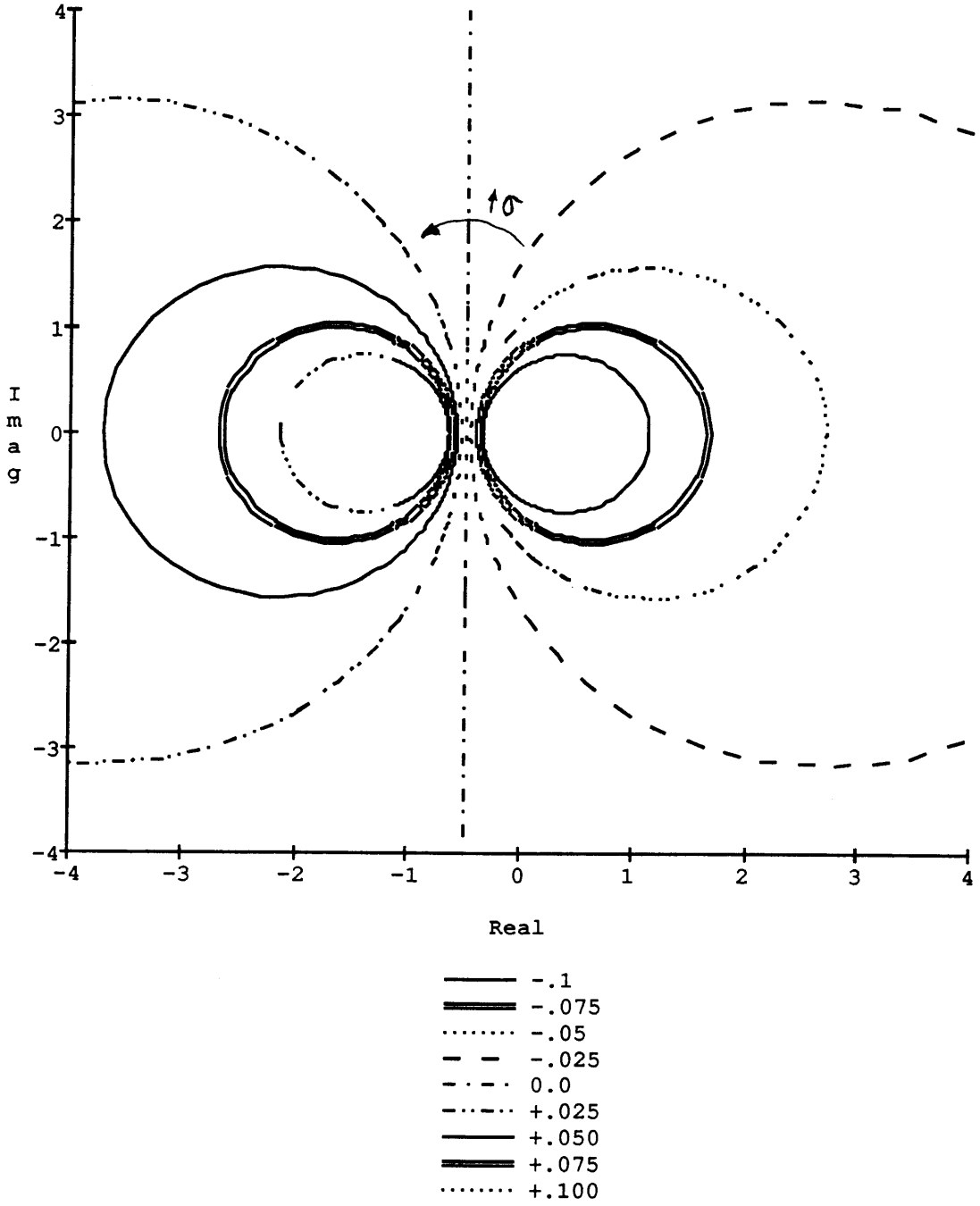

Figure 4-12: Regeneration Vector Locus with varying growth rate, sigma.

ditions change the angular orientation of the spirals similar to the way the hyperbola asymptotes changed in section 4.3.

What is significant about the spirals is their variation in size with changing lobe number and set up condition. Figure 4.15 shows the combined vector locus for 2 through 10 lobes with constant sigma at a given set up condition. As can be seen, some of these loops are much bigger than others. Like the angle analysis developed in section 4.4, it would beneficial to interpret the possible meaning of the spiral size in terms of the grinding process geometric stability.

An infinitely stiff machine is represented by a point at the origin on the complex plane. When the rounding and regeneration vector locus intersects with this machine locus, then geometric instability results. If a particular spiral is to intersect with the machine locus, it must be small enough to be near the origin. Therefore, whatever value of sigma is required to make the spiral small enough to intersect with the machine locus will be that particular lobes level of instability. For example, if one spiral is large compared to another at the same sigma, it should be clear that the larger spiral will require a larger sigma to become small enough to intersect with the machine's vector locus. Another way of viewing this is to realize that a better grinding condition will result from a set up condition whose spirals require very little instability (very small sigma) to intersect with the machine locus. Given this analysis, a set up condition with mostly large spirals is less desirable than a set up with smaller spirals at the same unstable sigma.

Using this reasoning, it is possible to derive an estimate of geometric grinding stability based on the size of the combined rounding and regeneration vector locus at a constant, non-zero sigma. If all lobing spirals at all set up conditions of interest are viewed on the complex plane with the same unstable sigma, then the total size of the spirals is likely proportional to the instability at each set up condition. Figure 4.16 shows the sum total size of spirals from 2 to 30 lobes at each set up condition in the normal grinding region. A three dimensional plot is pictured to aid in conceptual understanding.

Some important interpretations can be drawn from Figure 4.16. First, the same

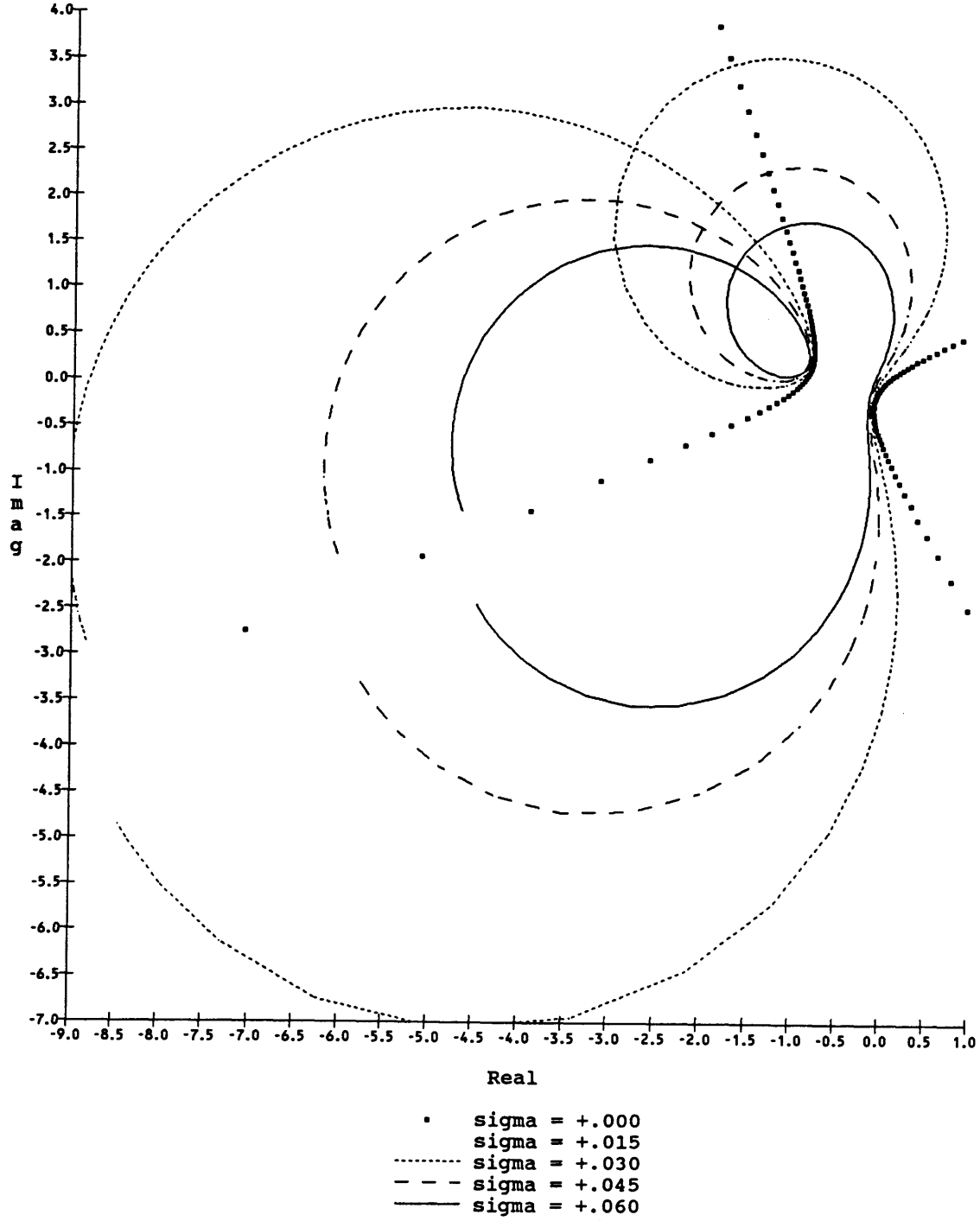

Figure 4-13: Positive Sigma changes the combined vector locus into spirals. As sigma increases, the size of the spirals decrease.

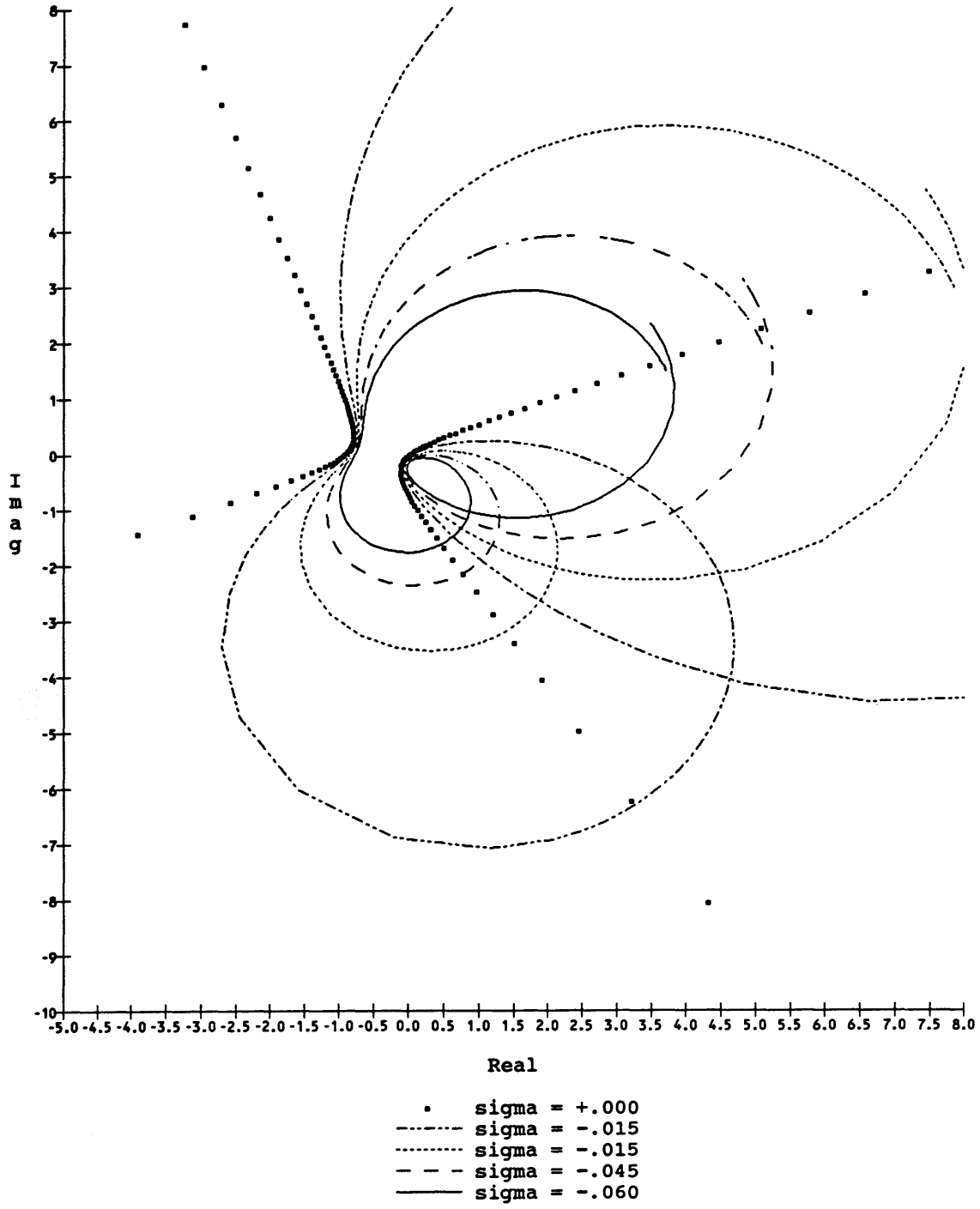

Figure 4-14: Negative Sigma also changes the combined vector locus into spirals but in the opposite direction. As absolute sigma increases, the size of the spirals decrease.

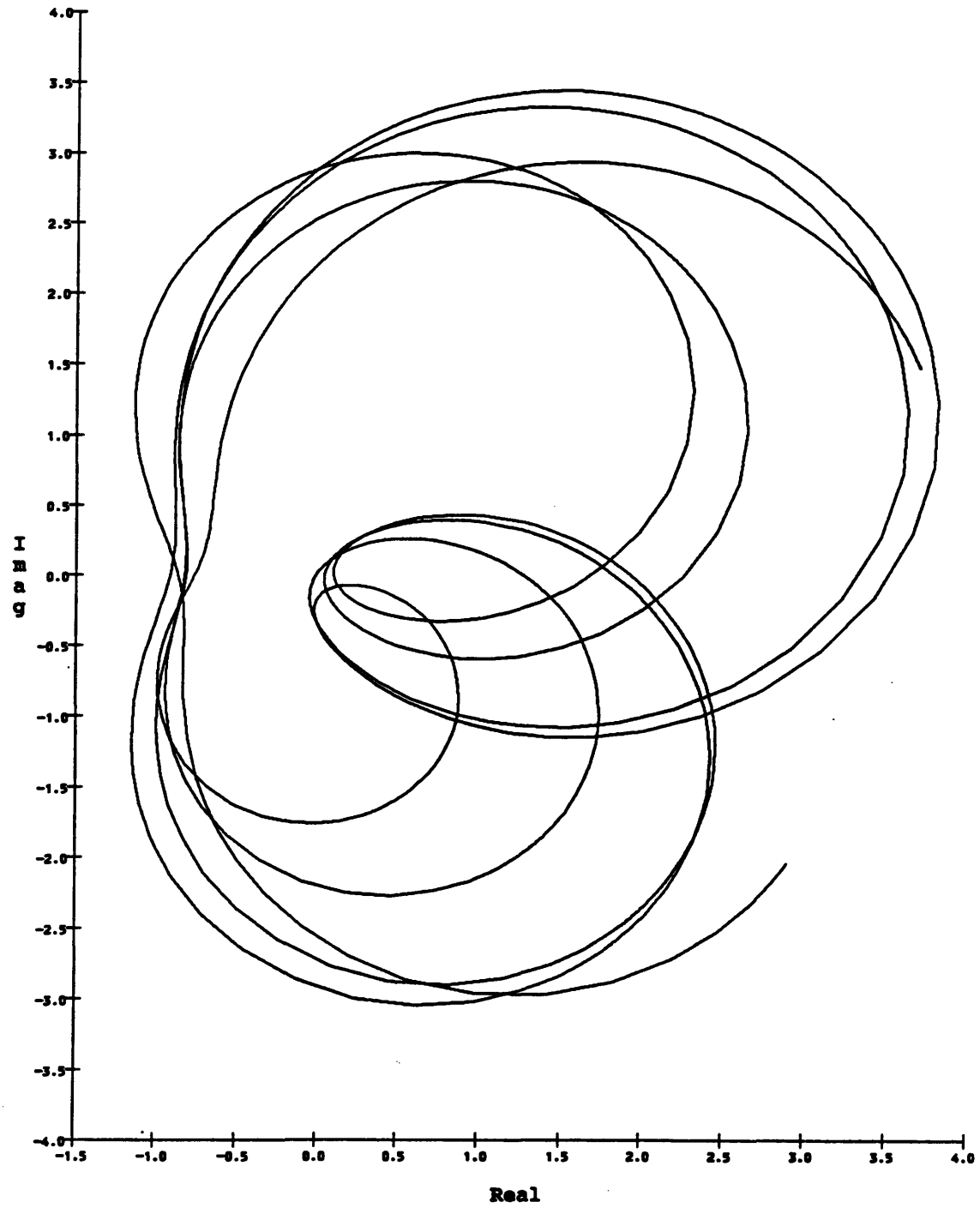

Figure 4-15: At constant, non-zero sigma, the combined vector locus varies in size for each separate frequency.

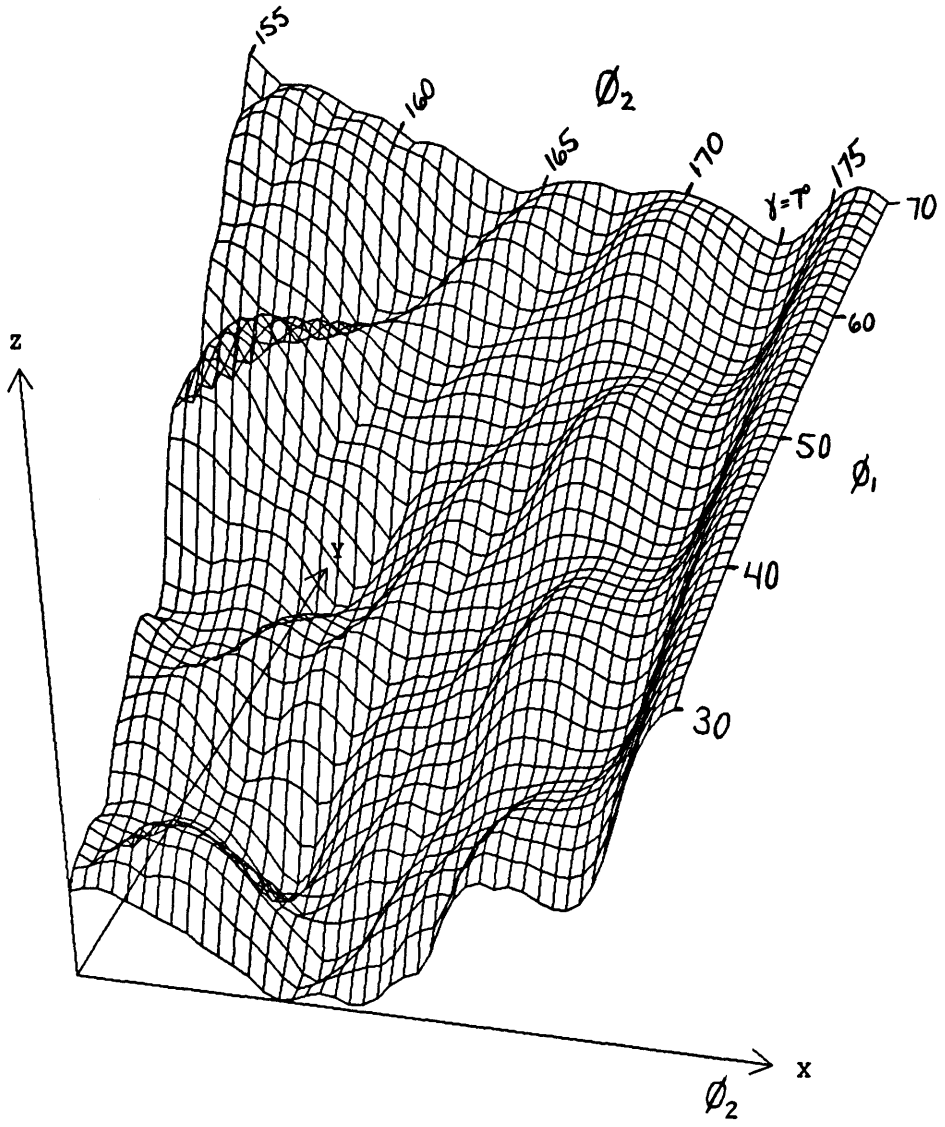

Figure 4-16: Three dimensional plot of the sum of the size of the combined vector locus in the normal grinding region for 2-30 lobes. Lower regions imply greater geometric stability.

general trends seen in the angular analysis plot of Figure 4.11 are also seen here: that smaller ϕ_1 and ϕ_2 generally imply greater geometric stability and should result in better workpiece roundness on a dynamically stable machine. Second, recalling that in wheel-type centerless grinding the maximum achievable center-height angle is about 11 degrees, the general conclusion from previous research that a center height of 7 degrees is optimal is reconfirmed here by the local valley near ϕ_2=173. Finally, there are several local minimums on Figure 4.16, implying the possibility of several acceptable geometric set up conditions which might achieve good part roundness.

Figure 4.17 shows a contour plot of the same analysis for the entire range of possible grinding geometries (neglecting gravity, friction, and workpiece driving torque). Assuming that lower numbers imply greater stability, there are two general regions of geometric stability. The first is found near the normal configuration of centerless grinding (ϕ_1=40-65, ϕ_2=140-175). The second favorable area is found near a configuration for centerless honing (ϕ_1=150-175, ϕ_2=185-210). Although never theoretically derived before, this plot shows that centerless grinding has empirically drawn itself near stable grinding regions.

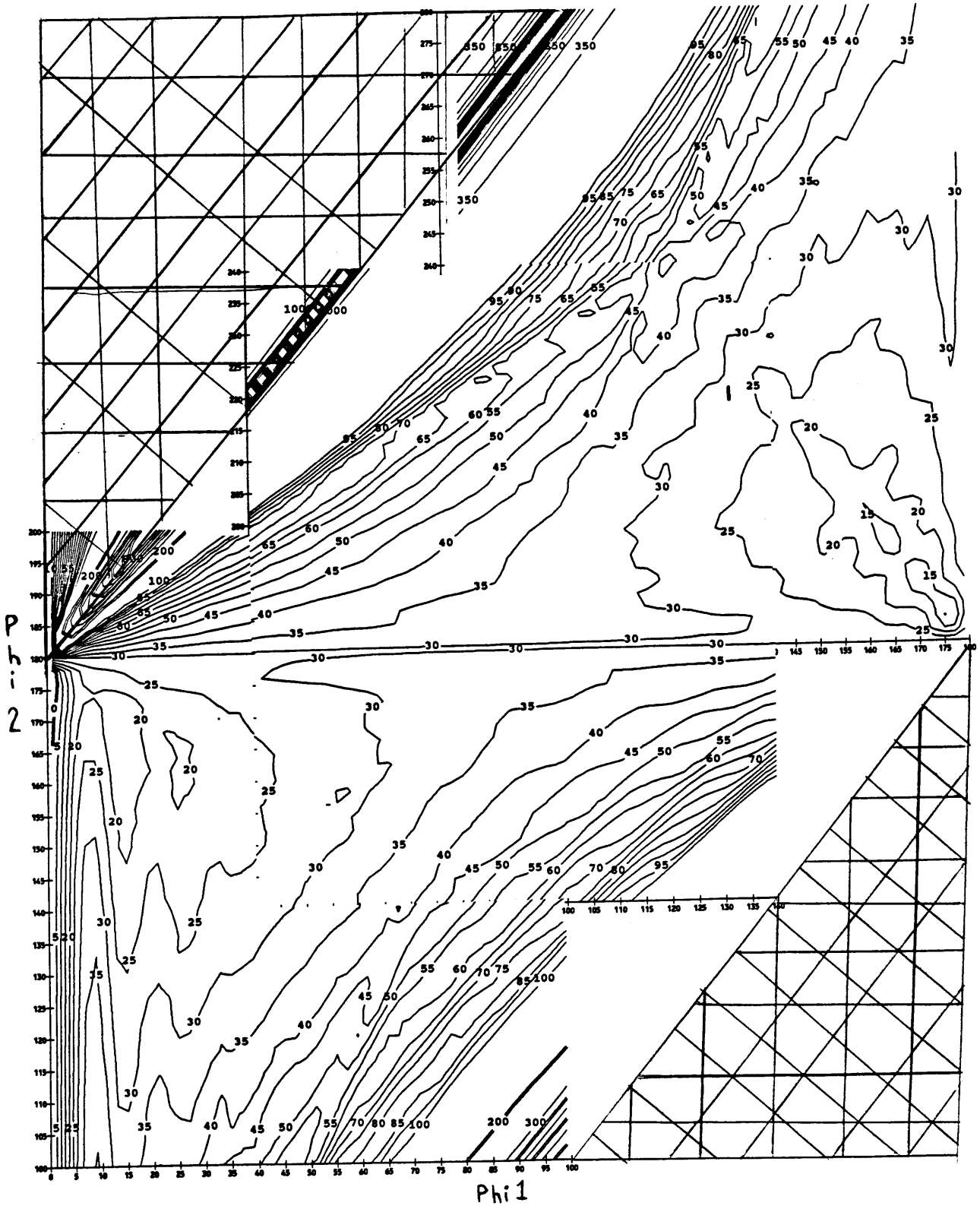

Figure 4-17: Contourplot of the sum size of the combined vector locus over the entire possible grinding range for 2-30 lobes. Lower contours imply greater geometric stability.

Chapter 5

Dynamic Theory and Analysis

The analysis so far has assumed that the part, support shoes, grinding wheel, and machine were perfectly rigid. In reality, the entire machine system is flexible and vibrates at a whole range of frequencies during normal operation. This section will attempt to model the machine and find its effect on the production process. The strategy here is to adequately model the machine in the Laplace domain, to match the machine locus with the combined locus from chapter 4 in the complex plane, and then to compare the various $s = \sigma + jn$ between set up conditions.

The machine vibration affects the accurate production of circular cross-sections three possible ways. First, the static stiffness of the machine can affect the workpiece size accuracy if grinding forces deflect the machine and result in erroneous sizing feedback. Second, the geometric effects discussed in chapter 4 will be amplified or reduced depending on the machines' lower resonant frequencies. Finally, the machines higher resonances can generate high frequency undulations on the piece, known as chatter, separate from of the geometric regeneration mechanisms. These mechanisms can all be described by observing the vibration frequency spectrum with corresponding growth rates in the s domain.

The machine effects will be combined with the work effects found in chapter 4 in the Laplace domain. By matching the machine vector locus with the combined work rounding and regeneration vector locus at a given frequency, the systems characteristic equation is solved graphically allowing the dynamic vibration growth rate to be

determined. This graphical coincidence will allow the comparison of differing set up geometries in terms of unstable exponential growth rates, σ in $s = \sigma + jn$.

5.1 Modeling the Machine

Grinding machines are made from separate components including motors, feed mechanisms, bearings, wheels, etc. Each of these components will likely resonate at one or more separate frequencies. Machine components are continuous structures which can be modeled as discrete sets of separate elements consisting of linear springs, masses, and dashpots. Each set of modeling elements will have its own characteristic equation, and all of these can be combined in the Laplace domain to yield the equation found in Figure 3.7:

$$H(s) = \sum_{n=1}^{m} \frac{\omega_n^2}{s^2 + 2\zeta\omega_n s + \omega_n^2} \tag{5.1}$$

The number, m, in equation 5.1 in reality approaches infinity, yet most of the major machine effects can be found when m is small and finite. This approach assumes that the machine is made of linear springs, etc. and that any non-linear element is linearized for the model.

To assure adequate modeling of a complex, unknown machine, this study will produce a detailed model and then simplify it to retain only the important effects. Figure 5.1 shows the proposed model of the machine which allows a simple system for each major component including: the workpiece, the shoes, the contact stiffness of the grinding wheel, the grinding wheel, the grinding wheel spindle, the infeed slide mechanism, and the machine base. This modeling allows for 7 independent natural frequencies, or m=7 in equation 5.1.

Figure 5.2 shows the bond graph representation for the system found in Figure 5.1. The input force is the normal grinding force which simultaneously transfers through the part to the shoes to the machine base and through the contact stiffness to the grinding wheel to the spindle to the slide to the machine base. It is assumed that the base is connected to the ground which damps out any remaining vibration. The machine's structural loop can be seen easily in this bond graph representation. This

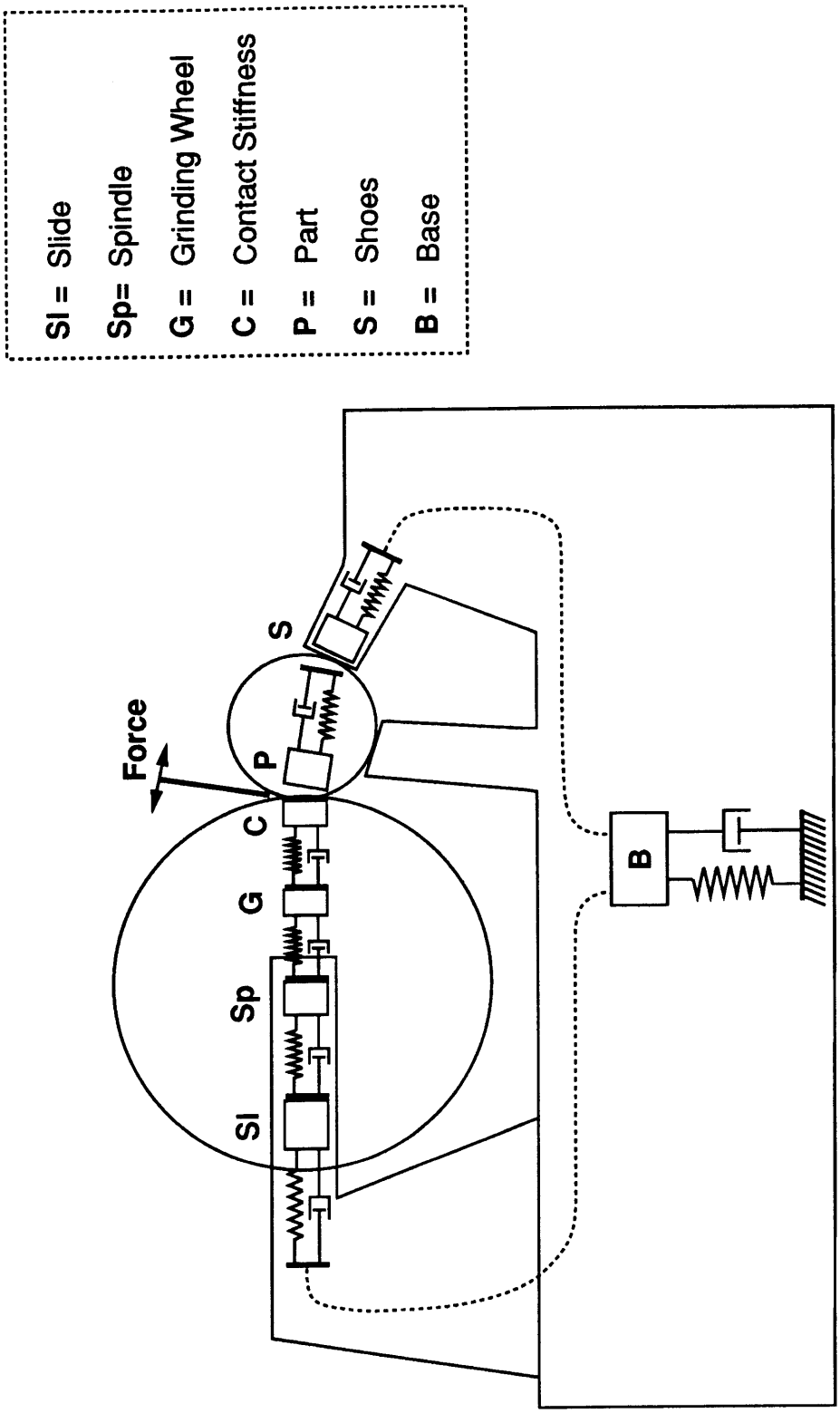

Figure 5-1: Diagram of the machine modeled with springs, masses, and dashpots.

model allows for the simultaneous vibration of both the grinding wheel and the part from the same grinding force, which increases the model's validity.

Using bond graph methods, linear, first order differential equations for the system shown in Figure 5.2 can be derived. Since there are seven masses and seven springs in series, there are fourteen independent energy storage elements in the system resulting in fourteen first order differential equations. The set of linear, differential equations is shown in matrix form in Figure 5.3. The matrix is quite symmetric and relatively sparse though large in size.

Clearly, virtually any response from such a large system could be derived depending on the mass, spring, and dashpot inputs of the model. It is therefore crucial to adequately estimate the m, k, and c inputs for the specific machine used during experimental testing. For example, grinding wheel spindle bearing surfaces can be either hydrostatic or rolling element, but a hydrostatic spindle's stiffness is much greater than the stiffness of a rolling element bearing. Therefore, the model must be tailored to the specific machine in question. Calculating the stiffness and damping of individual machine elements is extremely difficult, so it is often more practical to simply test the machine with vibration sensors to find resonant frequencies and damping coefficients. Although normally reserved for the experimental procedure section, it is useful to introduce these vibration tests now.

The shoe-type centerless grinding machine used in this study is a typical machine used in the bearing industry. An accelerometer and Hewlett-Packard vibration analyzer were used to test the machine for resonant frequencies. With the machine both operating and not, the accelerometer was placed at various locations on the machine to monitor vibration. For 'power off' tests, a piezo-electric hammer was used to simulate a forced impulse. Although any particular resonance is difficult to isolate, strategic placement of the accelerometer (for example directly behind the shoe) allowed relative isolation of particular component resonant frequencies. Figure 5.4 shows some of the vibration read-outs taken from the machine. By analyzing this vibration data, the resonant frequency of the components were estimated as shown in Figure 5.5. Because the linear model in Figure 5.2 requires mass, spring and dashpot

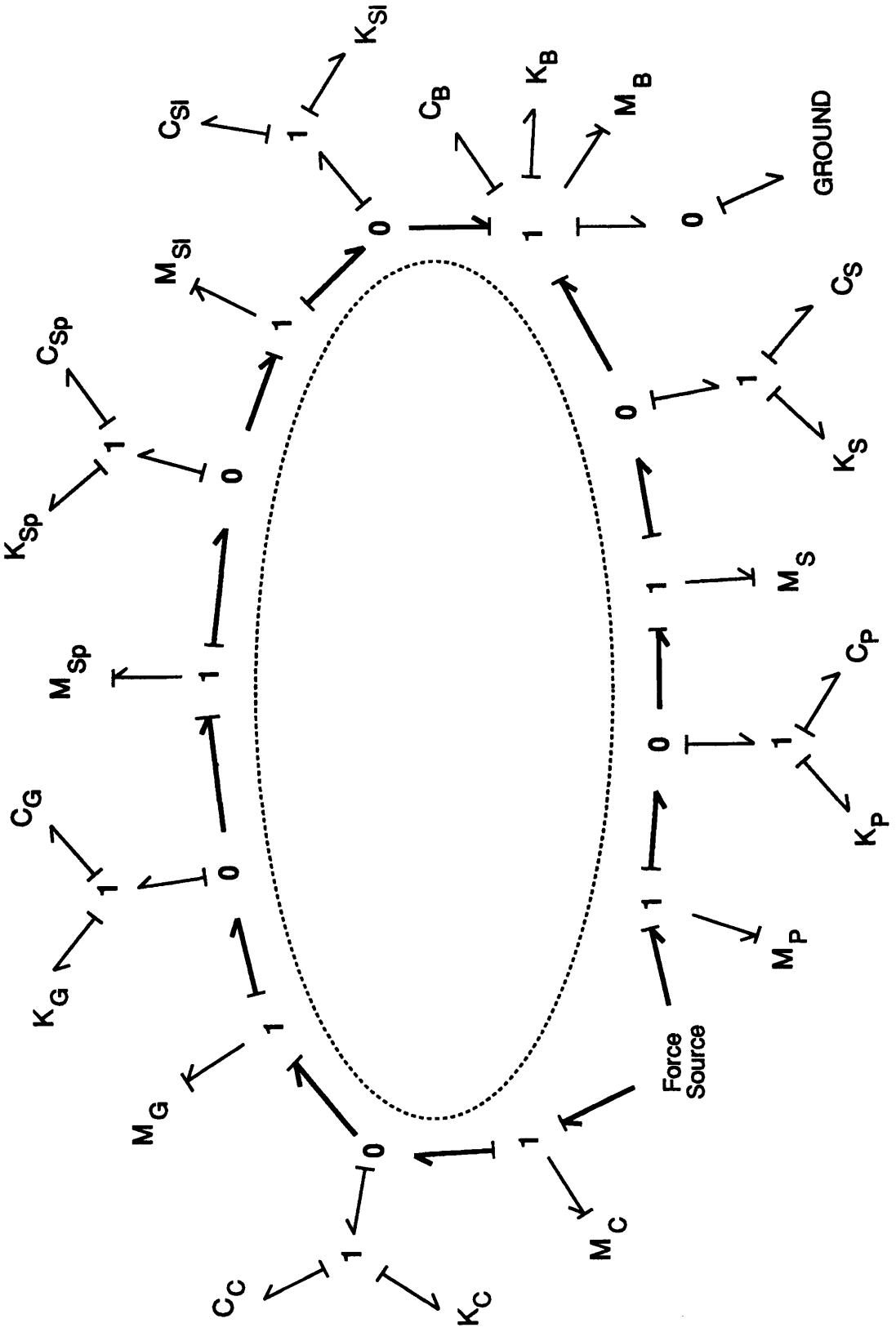

Figure 5-2: Bond Graph Representation of the dynamic machine.

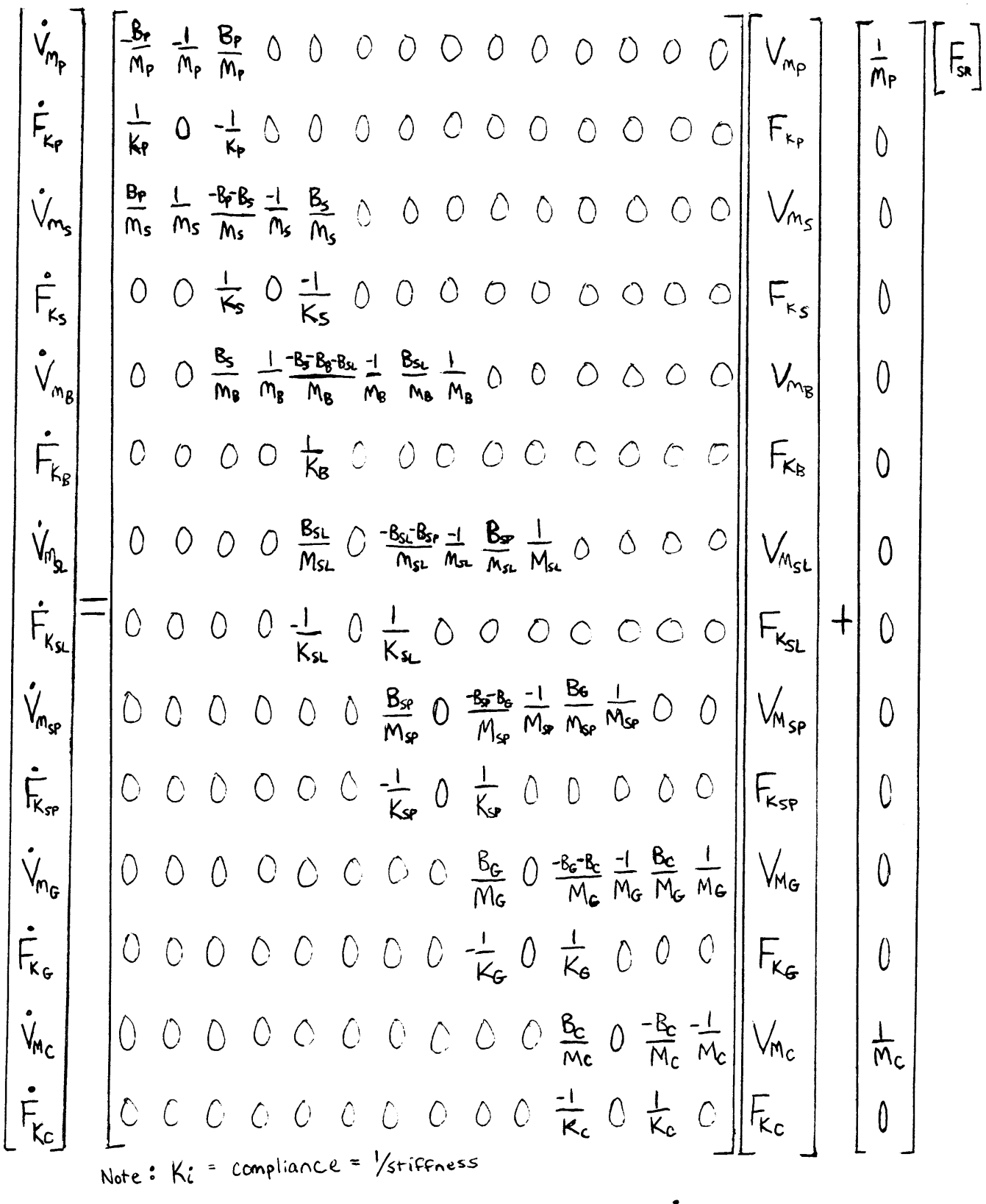

Figure 5-3: System linear, first order differential equations in $\dot{\vec{x}} = A\,\vec{x} + B\,\vec{u}$ form.

coefficients, the effective mass of each component had to be estimated to fit the model to the experimental machine vibration and damping characteristics.

When the experimental coefficients were entered into the linear model, a realistic mathematical simulation could result. In fact, a fourteenth order model was developed (as opposed to some other number) partially as a result of the machine vibration tests. The model was simulated using Matlab, and the resulting characteristic equation's amplitude Bode plot is shown in Figure 5.6. Since the linear model is somewhat coupled, the components were varied individually to find their resultant effect on the Bode plot. As can be seen, only a few of the resonant frequencies dominate the machine's dynamic response. The machine base resonance and the grinding wheel infeed slide were the major vibratory components of this machine. Results may vary from machine to machine, but as will be seen below, the general dynamic stability conclusion for centerless grinding will remain unchanged.

The conclusion from the above detailed machine modeling is that this machine can be effectively modeled with a reduced order system. That is, a sixth or fourth order system should include the majority of the machine effects. Shown in Figure 5.7 are the linear differential equations for a reduced, sixth order model. A much simpler derivation leads to these equations, and a representation similar to the bode plot amplitude is shown in Figure 5.8. For simpler calculations, a second order model was also analyzed to obtain a rough estimate of machine vibration.

5.2 The Combined Machine and Work Mechanism Vector Locus

This section will discuss the solution to the model originally presented in section 3.2. Because an explicit mathematical solution would be very difficult to find, a numerical solution was found with the graphical coincidence method. The machine vector locus was plotted in the complex plane, and the work mechanism locus (the combined rounding and regeneration locus) frequency and growth rate were adjusted until they graphically coincided. When graphical coincidence is achieved the

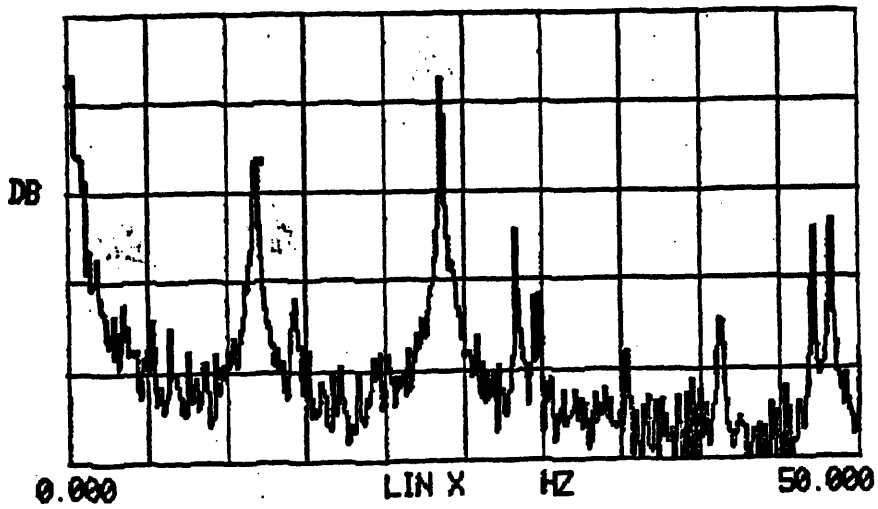

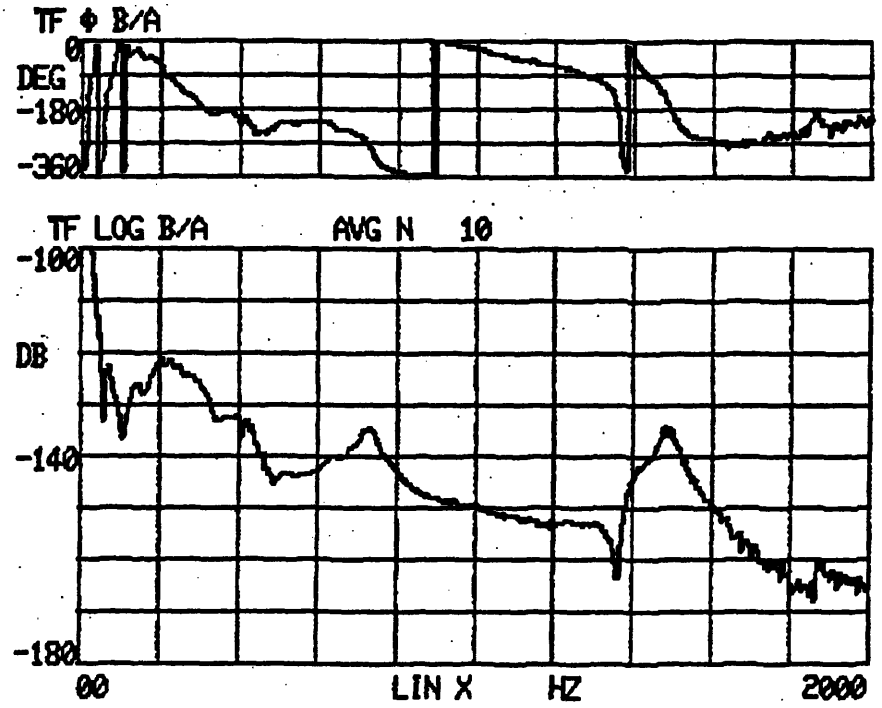

Figure 5-4: Sample experimental vibration test results from the machine.

Experimental Vibration Tests

Component	Natural Frequency
Machine Base	23.5 Hz
G. Wheel Slide	48.8 Hz
Contact Stiffness	82.5 Hz
G. Wheel Spindle	194 Hz
Workpiece	525 Hz
Shoes (both)	735 Hz
Grinding Wheel	1950 Hz

Figure 5-5: Experimental vibration frequencies table.

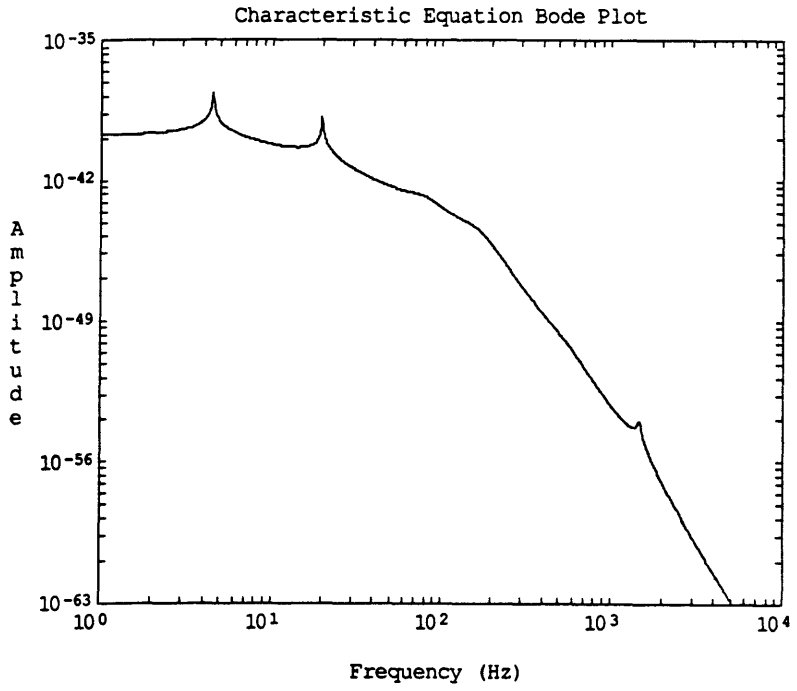

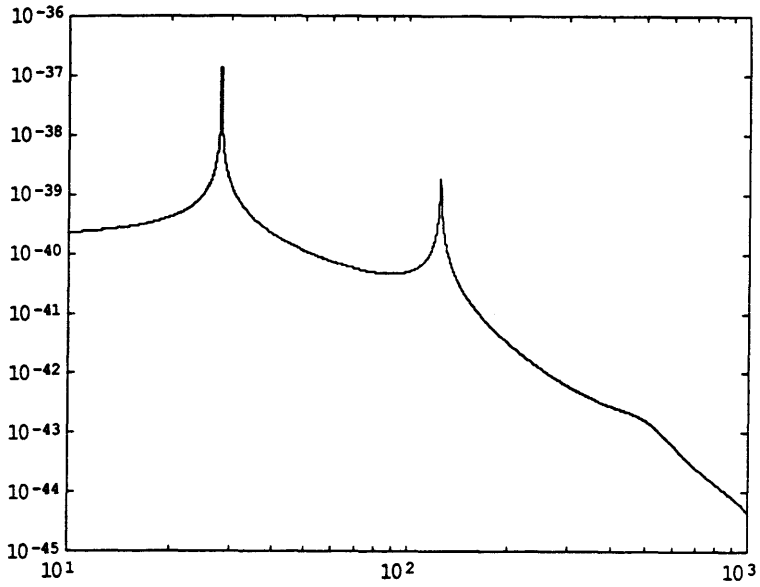

Figure 5-6: Bode plot of the 14th order machine characteristic equation using the parameters from the vibration tests from the experimental machine.

$$\begin{bmatrix} \dot{V}_{m_1} \\ \dot{F}_{K_1} \\ \dot{V}_{m_2} \\ \dot{F}_{K_2} \\ \dot{V}_{m_3} \\ \dot{F}_{K_3} \end{bmatrix} = \begin{bmatrix} -\frac{B_1}{M_1} & -\frac{1}{M_1} & \frac{B_1}{M_1} & 0 & 0 & 0 \\ K_1 & 0 & K_1 & 0 & 0 & 0 \\ \frac{B_2}{M_2} & \frac{1}{m_2} & \frac{-B_1-B_2-B_3}{m_2} & \frac{-1}{m_2} & \frac{B_3}{m_2} & \frac{1}{m_2} \\ 0 & 0 & K_2 & 0 & 0 & 0 \\ 0 & 0 & \frac{B_3}{m_3} & 0 & -\frac{B_3}{m_3} & -\frac{1}{m_3} \\ 0 & 0 & -K_3 & 0 & K_3 & 0 \end{bmatrix} \begin{bmatrix} V_{m_1} \\ F_{K_1} \\ V_{m_2} \\ F_{K_2} \\ V_{m_3} \\ F_{K_3} \end{bmatrix} + \begin{bmatrix} 1/m_1 \\ 0 \\ 0 \\ 0 \\ 1/m_3 \\ 0 \end{bmatrix} \begin{bmatrix} F_{SR} \end{bmatrix}$$

Figure 5-7: First order differential equations matrix for 6th order machine.

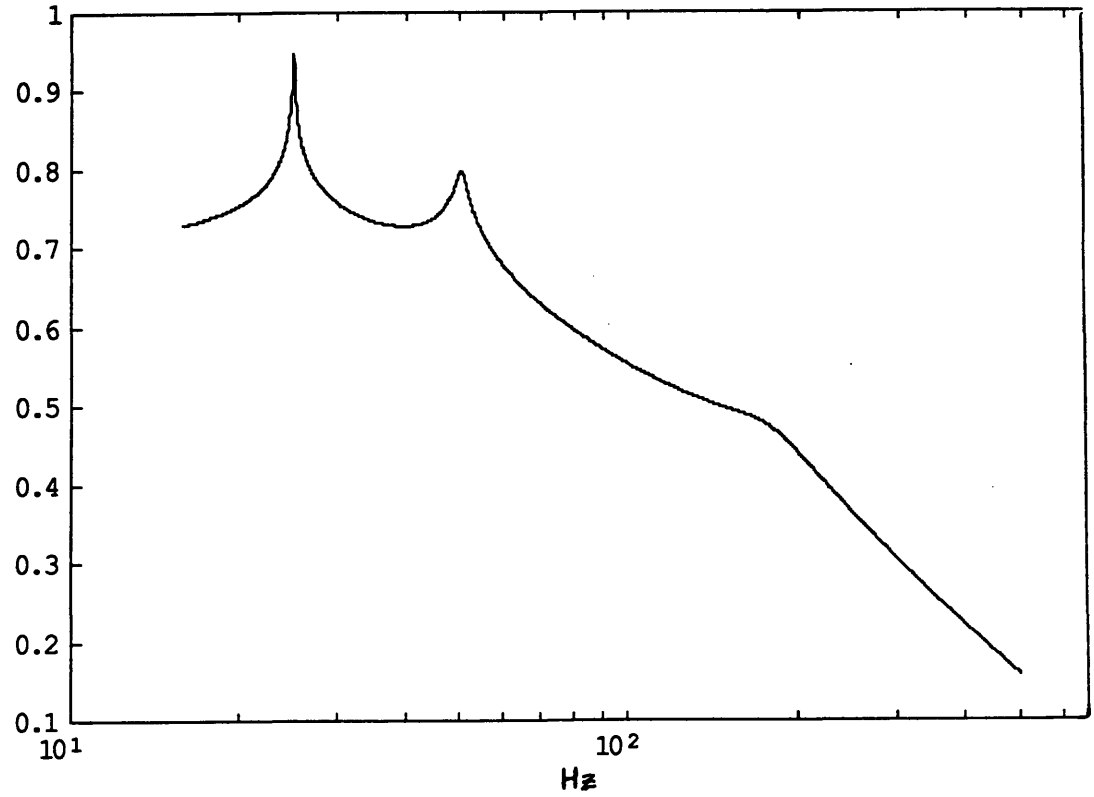

Figure 5-8: Plot similar to Bode representation of the 6th order machine.

frequency and sigma match for both loci, and a system dynamic root is established. Dynamic analysis is best conducted by finding the system roots, since the roots of the system completely characterize system stability. A comparison of the system roots at different set up conditions allows a comprehensive dynamic stability chart to be developed based on set up conditions.

As developed in section 4.5.2., for any particular set up condition, the work rounding and regeneration spiral for a particular lobe can be adjusted in size by changing the exponential growth rate, sigma. The goal of this analysis was to pick a particular frequency on the machine locus and find the lobing frequency (lobe number times workpiece revolutions per second) which matched it. Then, the sigma value was adjusted until both loci intersected on the complex plane. The final sigma value may have been either positive or negative depending on the specific lobe, and the exact frequency may have been adjusted to find a perfect match.

A numerical iteration scheme was developed to find the roots of the system. First, the machine vector locus and the work mechanism vector locus at a particular frequency were plotted. The sigma was varied slightly (plus and minus) to find a sigma which minimized the distance between the vector loci (since zero distance would imply a match). Then, in repetitive fashion, the exact frequency and sigma of the loci were varied until the relative distance was very small. Figure 5.9 shows this 'root finder' solution in action on the complex plane for a particular lobe at a given set up condition. As can be seen, the program zeros in on the root until a match is found at an stable sigma of -.014. This same scheme was repeated for each frequency of possible unstable matches over the entire range of set up conditions.

Figure 5.10 shows the range of matched sigmas and frequencies for a particular set up condition with a second order machine plotted in the s domain. Any negative sigma implies that the vibration frequency will not grow exponentially while any positive sigma implies unstable vibration growth. As can be seen, the even and odd frequencies followed trends of stability. The even number frequencies typically remained in the stable region, while the odd number frequencies went unstable near ω/ω_n=1 to ω/ω_n=1.5, as depicted in Figure 5.11.

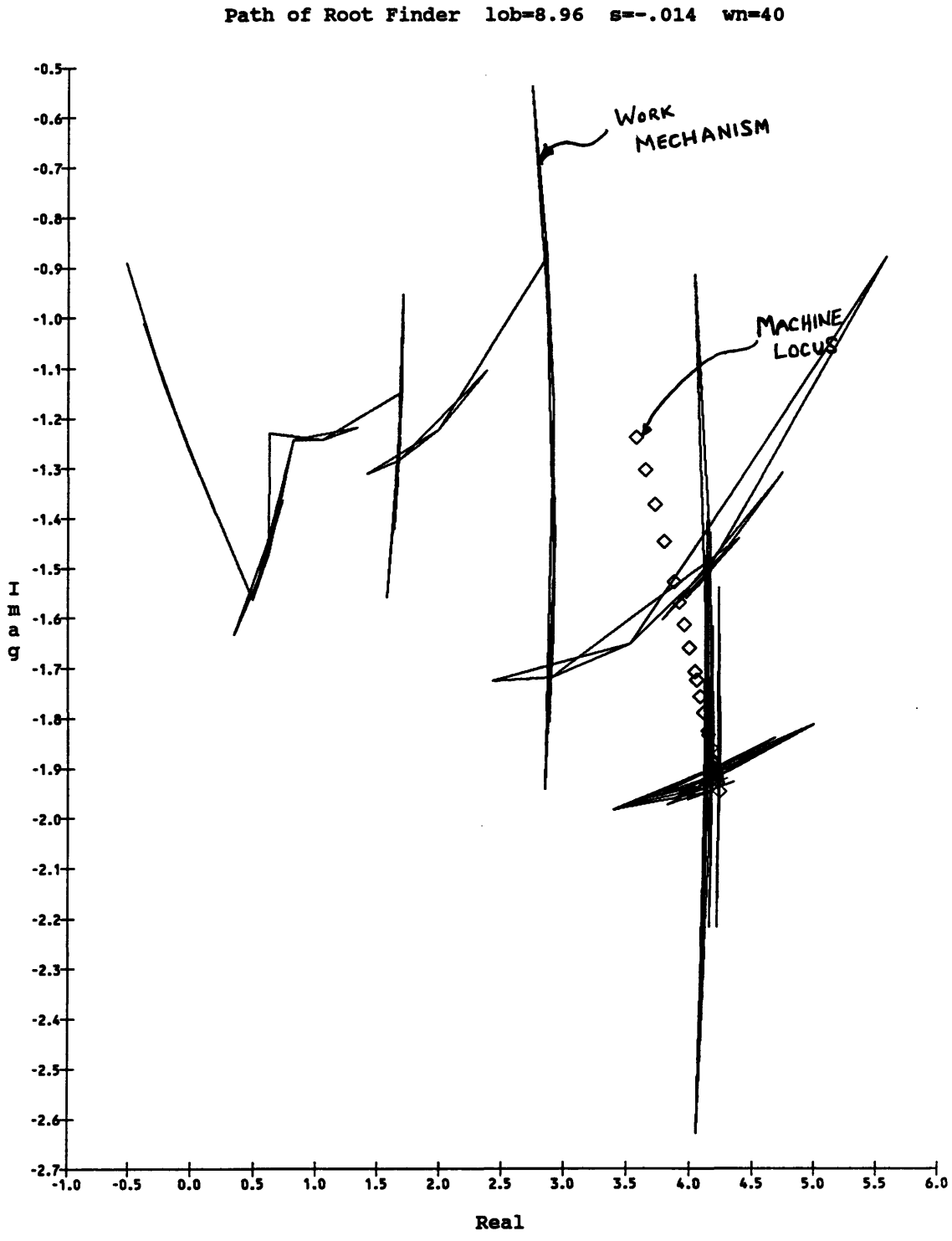

Figure 5-9: 'Root Finder' iteration scheme adjusts the frequency and sigma until the machine and work mechanism vector locus match on the complex plane.

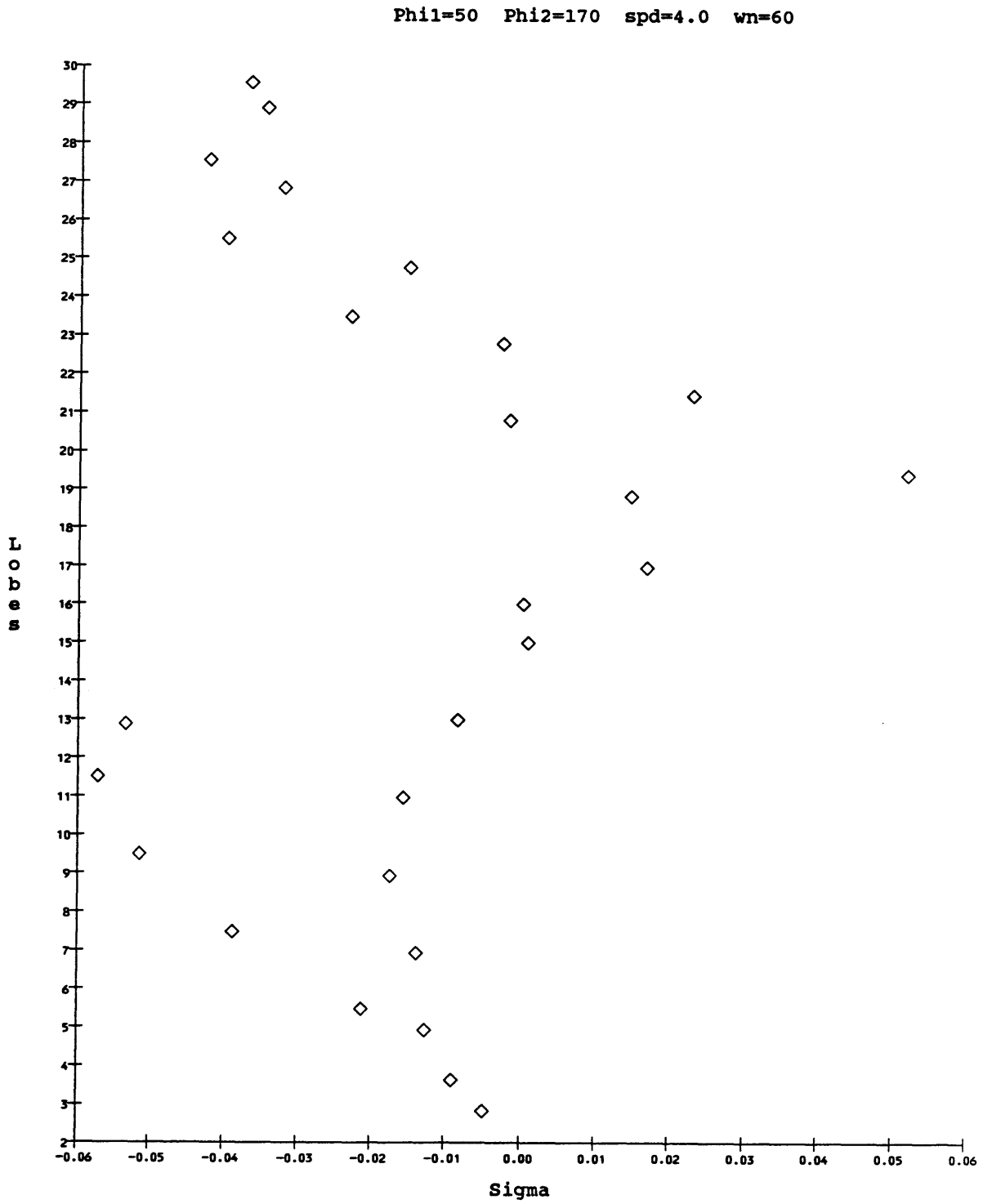

Figure 5-10: Characteristic roots for one particular set up condition. The system goes unstable approximately between ω/ω_n=1 to 1.5. Each lobe number has either a positive or negative dynamic growth rate.

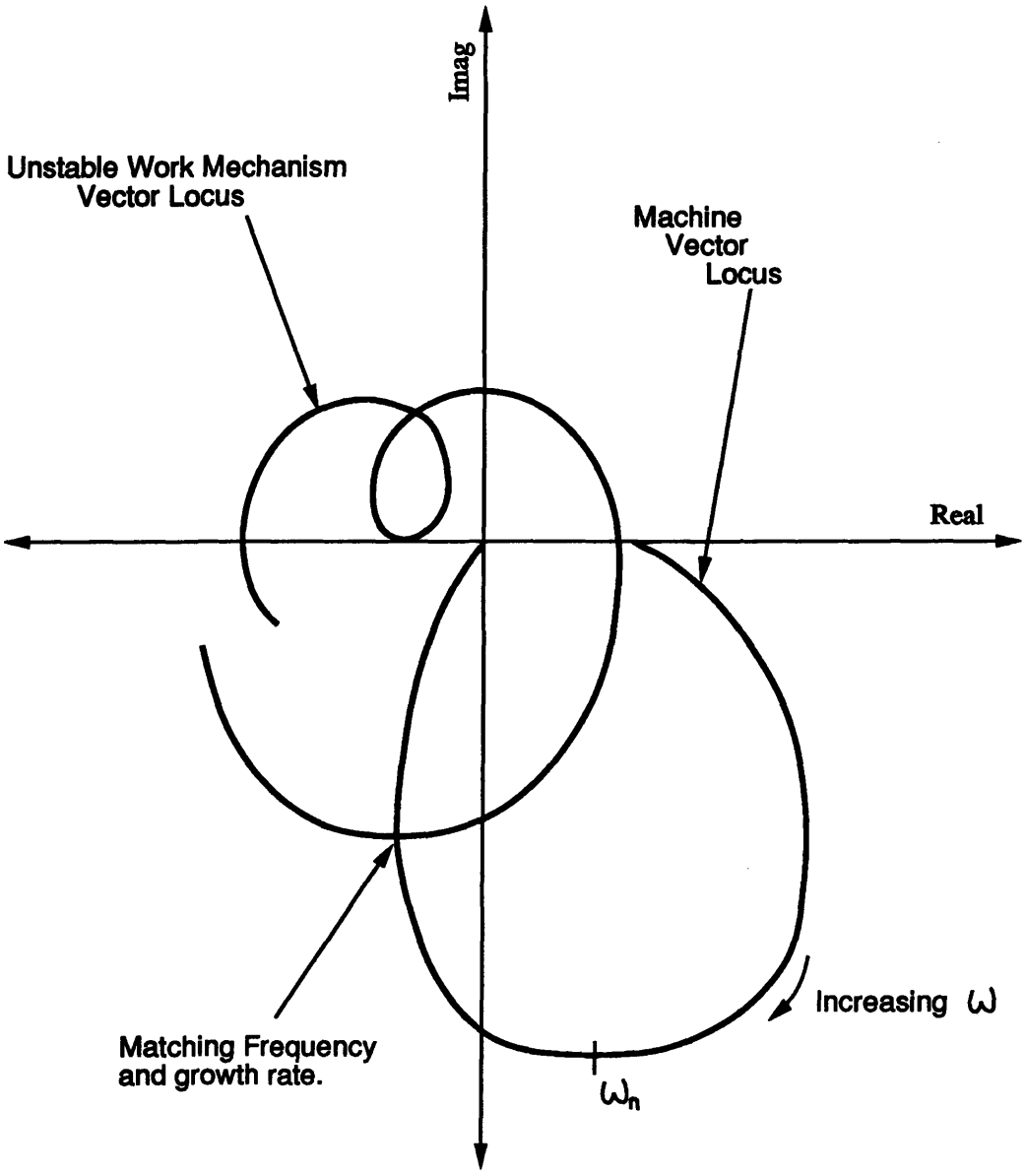

Figure 5-11: Sketch showing why the unstable frequencies are often just higher than ω_n. The sample spiral shown has an positive growth rate.

The stable and unstable roots in centerless grinding have never been found before for the complete system proposed in this study. Several interpretations of the root locus for centerless grinding are warranted. First, each resonant frequency of the machine may produce unstable roots for the system, depending on workpiece speed. Second, both the maximum unstable root and the total sum of unstable roots can be used as a parametric stability estimate of any particular set up condition. Third, higher frequencies are often damped by the contact length of the grinding wheel resulting in better performance for stiffer machines. Finally, higher machine damping will decrease the magnitude of unstable roots, suggesting that better damping will yield better machine performance regardless of set up conditions.

What is fundamental to this analysis is the ability to compare different set up conditions in terms of dynamic stability. The numerical root simulation was performed for second and sixth order machines, each resulting in the same general conclusion: that increasing ϕ_1 and ϕ_2 in the normal grinding range will increase the dynamic stability of the system. Figure 5.12 shows the contour plot of the maximum unstable root at each set up condition in the normal grinding range and beyond for a second order system with a resonant frequency of 100Hz. Figure 5.13 shows the total sum of roots at each set up condition for the same range and machine. The general appearance of both plots is similar, namely that smaller values of ϕ_1 and ϕ_2 are generally more unstable than larger values. One notable exception is for the immediate area near ϕ_2=180 degrees, which is generally unstable regardless of the value of ϕ_1. This same simulation was performed for second and sixth order machines with varying resonant frequencies, with each result differing slightly in detail but all holding the same general conclusion represented by Figure 5.14 where darker regions are more unstable than lighter regions. This conclusion has not been suggested from a rigorous theoretical standpoint before this study. As will be shown in chapter 6, the general trends suggested here were verified experimentally.

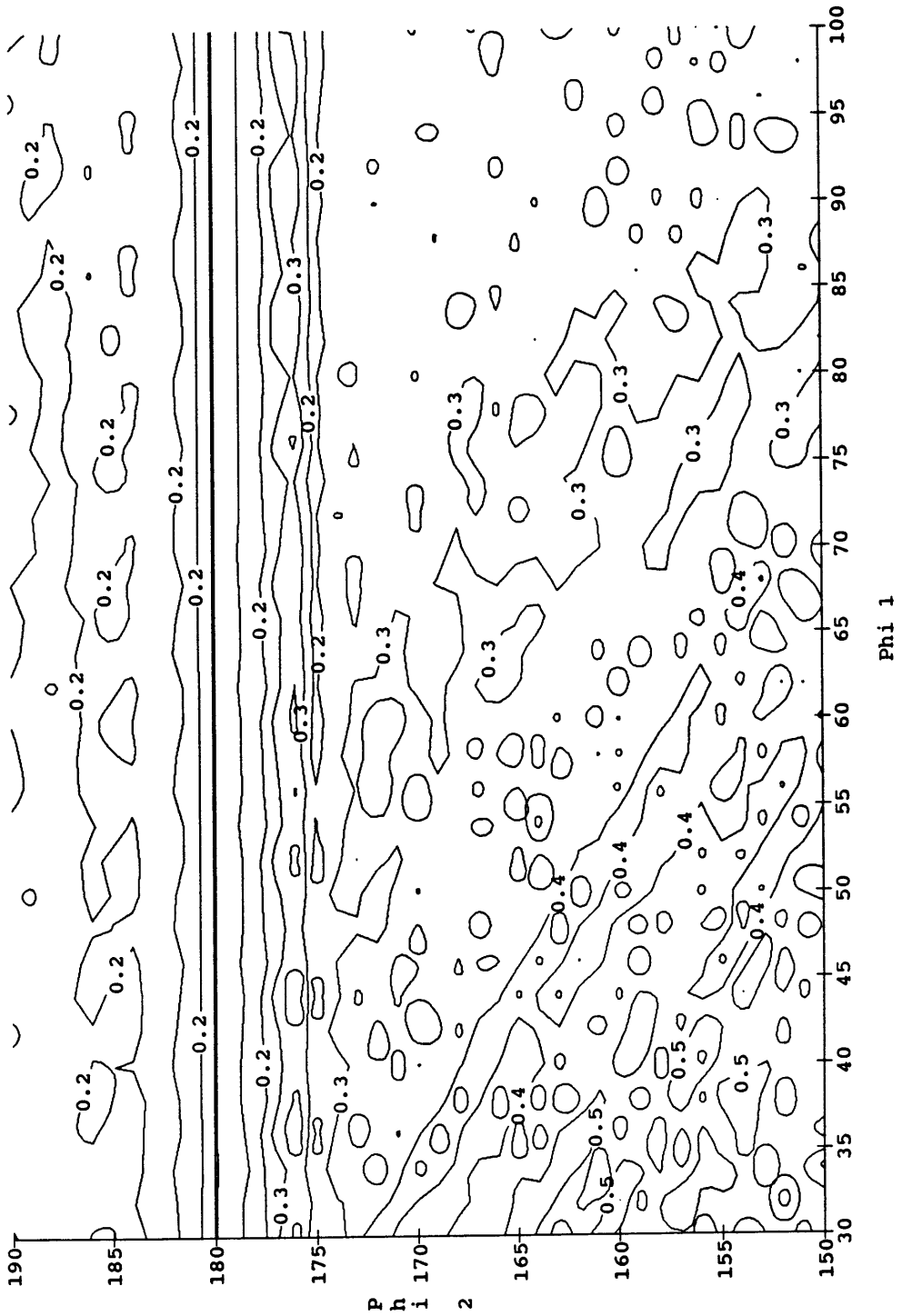

Figure 5-12: Contourplot of unstable roots found in the entire grinding region for a second order machine. Though difficult to see clearly, the higher (more unstable) contours are located at the lower left of the plot with better stability at increasing set up angles.

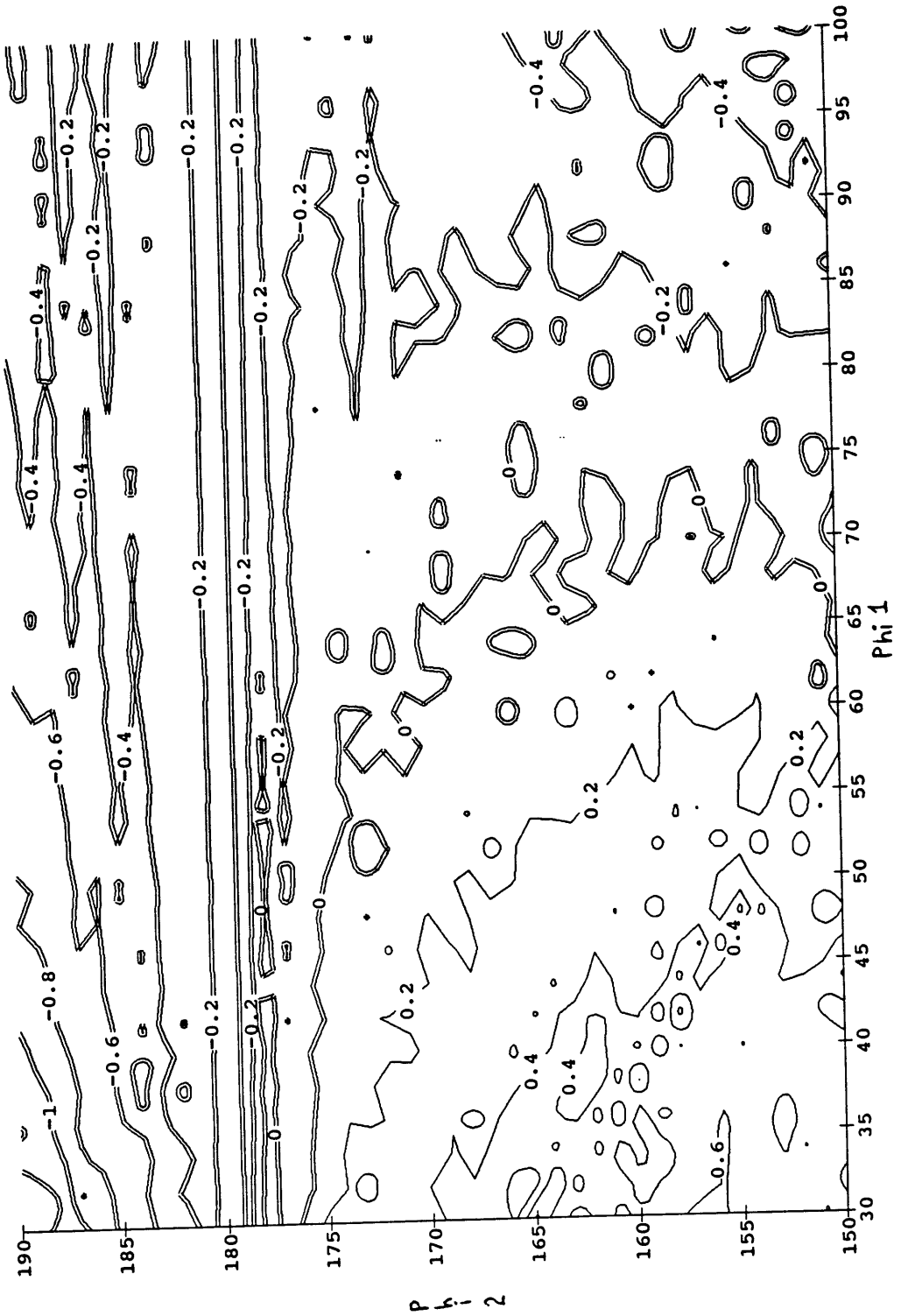

Figure 5-13: Contourplot of sum of roots found in the grinding region for a second order machine. Again difficult to see clearly, the higher (more unstable) contours are located at the lower left of the plot with better stability at increasing set up angles.

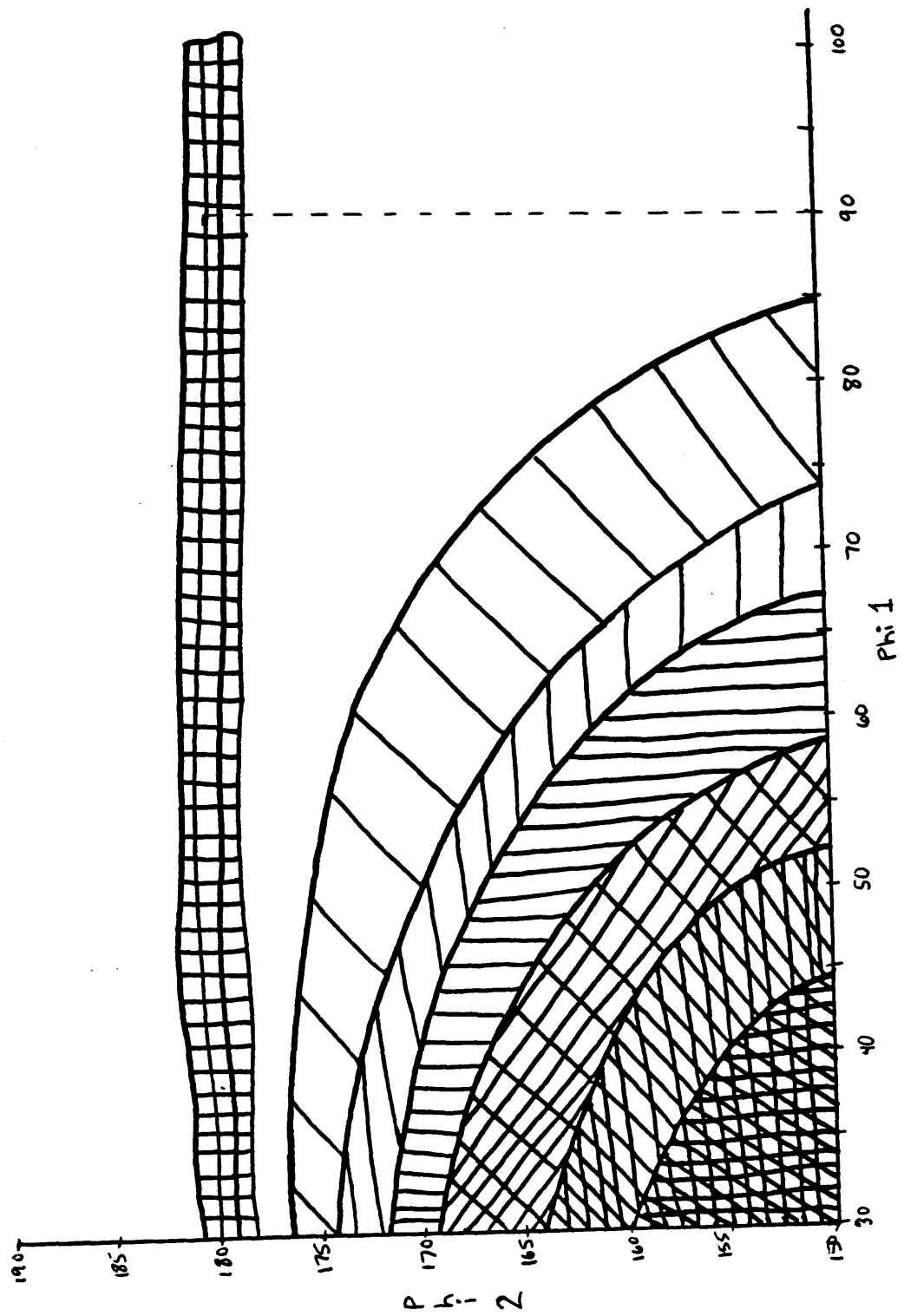

Figure 5-14: Sketch showing the general trends of dynamic stability in centerless grinding. Here, the darker regions imply worse dynamic stability

Chapter 6

Experimental Testing

6.1 Experimental Apparatus and Procedure

Testing was completed to verify the theoretical results presented in this study. The machine used was a typical one for the bearing industry, as mentioned before. As much as possible, all grinding variables (speeds, feeds, etc.) were kept constant in these tests except for the two shoe angles, ϕ_1 and ϕ_2. Changes in the angles ϕ_1 and ϕ_2 were made with two adjustable shoe mechanisms represented in Figure 6.1. At each shoe position, the shoes were secured in place with bolts, allowing repeatability better than 0.25 degrees. For all of the geometric tests the workpiece speed was kept low enough to allow the grinding wheel contact length to filter out a machine resonance near 800Hz, but in the vibration growth tests, the workpiece speed was doubled so that this source of vibration was not filtered out.

Since ϕ_2 is generally more critical than ϕ_1 in the normal set up range, ϕ_2 was tested at increments of 2 degrees from 149 to 177 degrees. ϕ_1 was tested at increments of 5 degrees from 35 to 65 degrees. All workpieces were pre-ground at the same set up condition to reduce workpiece input variation. Then, to assure repeatability, from 2 to 5 workpieces were ground at each combination of shoe angles in the range. Also, the grinding wheel was dressed between each test to assure wheel roundness. Workpiece roundness traces were taken with an Indy-rond gage connected to a digital spectrum analyzer.

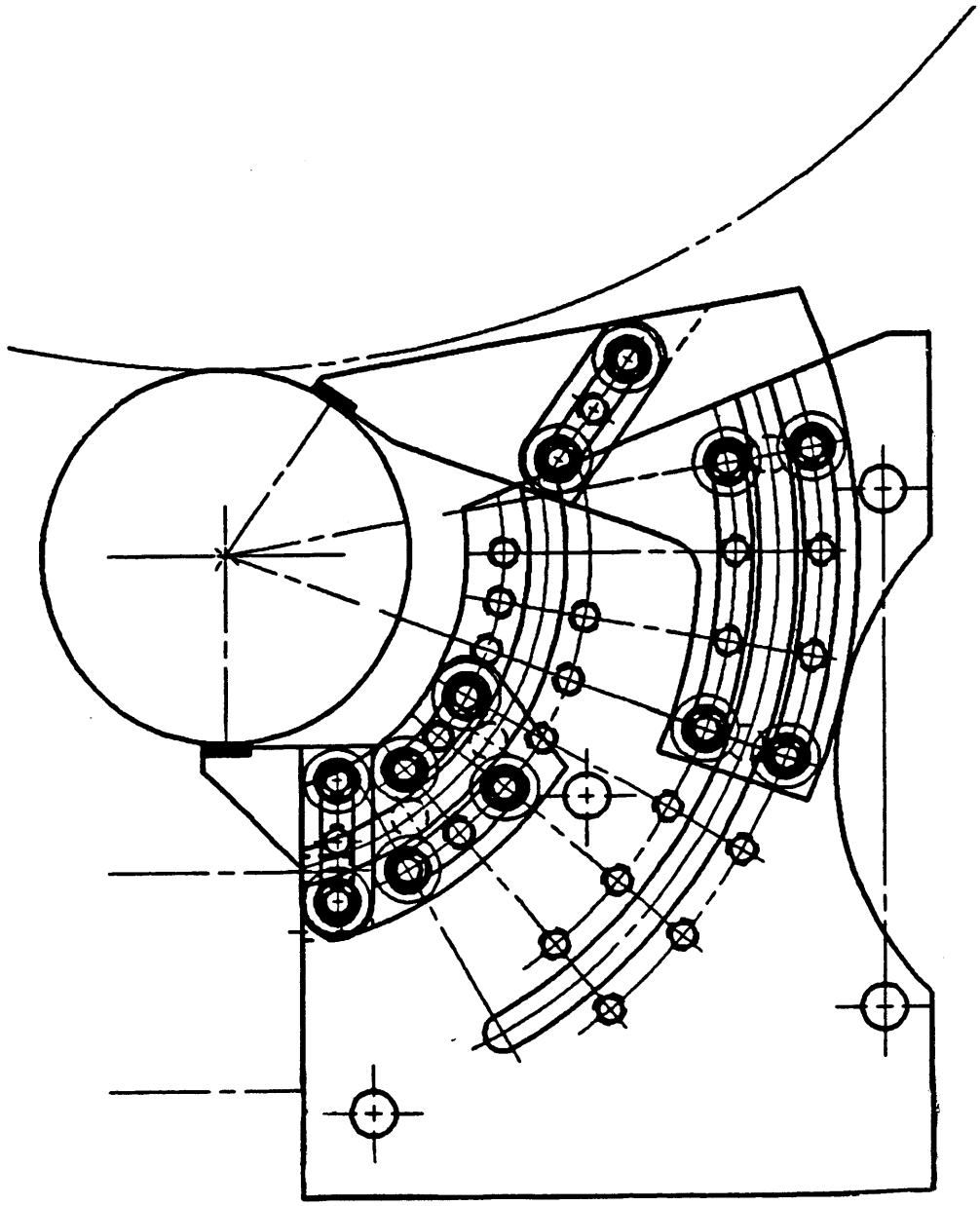

Figure 6-1: Sketch of experimental set up where each shoe could be moved inside a 30 degree range then bolted into place.

A typical roundness trace is seen in Figure 6.2. As can be seen, both the deviation from a perfect circle is plotted along with a listing of the magnitude of any lobing frequency whose amplitude exceeded 3μin. For example, Figure 6.2 shows that the set up condition, ϕ_1=60 and ϕ_2=165 degrees, showed a total radial deviation from round of 72μin with significant lobing at 2,3, and 12 lobes. Traces like Figure 6.2 were taken from hundreds of various tests with results below.

6.2 Lobing Instability

Section 4.4 discussed the possibility that under dynamically stable conditions, unstable lobing could still result from purely geometric considerations. Each test's roundness trace was analyzed for any lobing with amplitude greater than 20μin. For example, the trace seen in Figure 6.2 has a significant 12 lobe condition with a magnitude of 30μin. A tabular summary of each set up conditions significant lobing is seen in Figure 6.3 where ϕ_1=60, γ=15 (ϕ_2=165) degrees shows 2, 3, and 12 lobes from Figure 6.2. As can be seen, sections of this table have lobes which are generally significant over a particular region. These significant regions (two or more nearly adjacent set ups except for 2 and 3 lobes) were reduced to a contour style map and then plotted against the theoretical predictions (Figure 4.9 from section 4.4) in Figure 6.4. The experimental test results are plotted inside the box shown with a dark black line. As can be seen *every* significant lobing region found experimentally coincides with those predicted by the theory except the 12 lobe condition near ϕ_1=60 and ϕ_2=150 degrees. The exact alignment is not perfect but the experimental regions do match the general regions predicted by the model. Also, every lobe predicted unstable by the theory is not seen experimentally with a value over 20μin, most likely due to the fact that the theory is geometric in nature while the experiments include the finite stiffness of the machine and the fact that the testing only sample select points in the region.

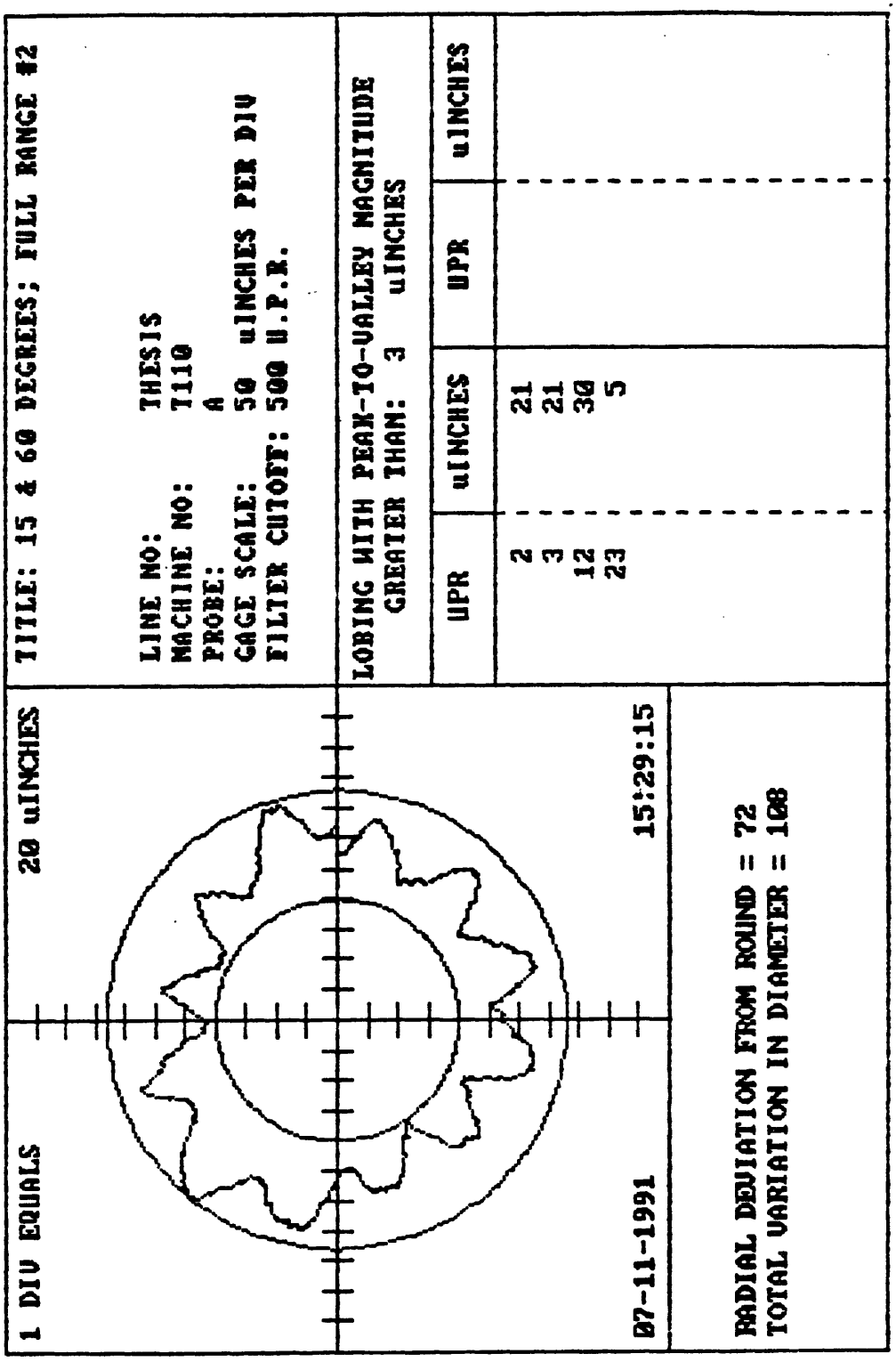

Figure 6-2: Sample roundness trace of an experimental workpiece taken with an Indy-Rond Gage.

GAMMA	35	40	45	50	55	60	65
31	2, 30	2, 18	*	*	2, 6, 13, 19	2, 6, 12, 18	*
29	2, 20	2, 8, 18	*	*	6,13,18,25	6,12,18	*
27	2, 20	2, 8, 16	8, 15	2, 6	2, 6, 13	2, 3, 6, 12	2, 3, 6, 27
25	2	2, 8	8, 15, 17	2,3,6,8,15	2, 6	2, 6, 17, 24	2, 3
23	2, 10	2, 17, 8	8, 17	2	2, 3, 6	2, 17, 35	2, 3, 17
21	2, 3, 10	2, 17	2, 17	2	2, 19	2, 3	2, 3
19	2, 3, 10	2	2	2, 3, 21	2, 19	2, 3, 12	2, 3
17	2	2	2, 3	2, 3, 14	2	2, 3, 23	2, 3, 10, 21
15	2, 3	2	2, 3	2, 3	2	2, 3, 12	2, 3
13	2, 3	2, 3	2, 3	2, 3, 16	2, 3	2, 3	2, 3, 5, 16
11	2, 3	2, 3	2, 3	2, 3, 16, 20	2	2, 3, 5	2, 3, 16
9	2, 3	2, 3	2, 3, 22	2, 3, 20	2, 3	2, 3	2, 3, 5, 9
7	2, 3, 5	2, 3	2, 3	2, 3, 5	2, 3, 5	2, 3, 5	2, 3, 5
5	2, 3	2, 3	2, 3	2, 3, 5, 7	2, 3, 5	2, 3, 5, 7	2, 3, 5, 9
3	2, 3, 5	2, 3, 5	2, 3, 5, 7	2, 3, 5, 7	2, 3, 5, 7	2, 3, 5, 7	3, 5
1	*	*	*	*	*	*	*

Phi 1

Figure 6-3: Table showing which lobing conditions were found at various set up conditions with an amplitude over 20 microinches. A '*' indicates no testing was done at this set up condition.

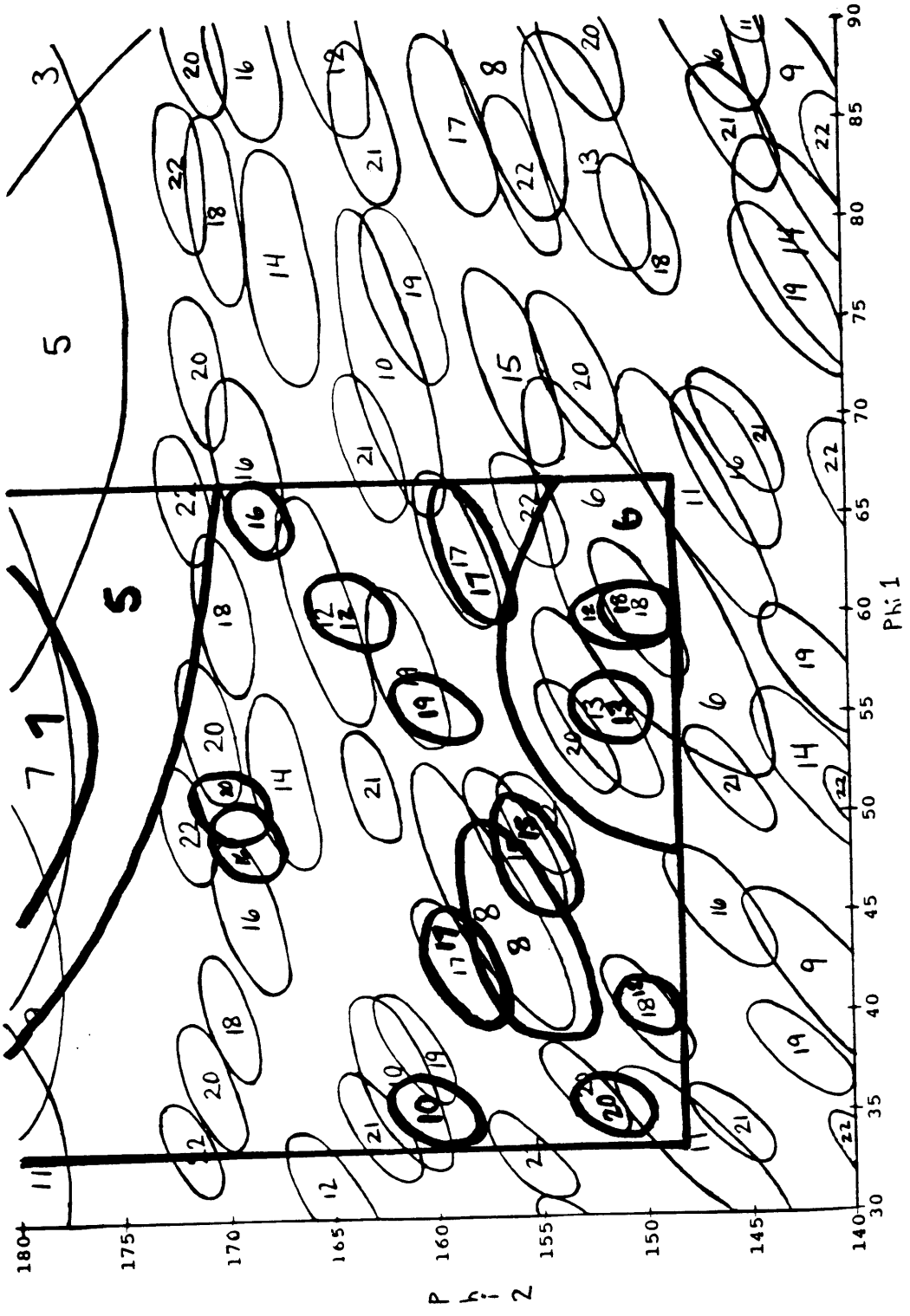

Figure 6-4: Experimental groupings of significant lobing overlaid on the theoretical predictions. The darker lines represent the experimental findings.

6.3 Overall Roundness Results

For the grinding range in this study, the average roundness results for each set up condition are shown as a contour plot in Figure 6.5 where the y-axis is the angle γ which is $180-\phi_2$. Although the plot represents just less than 100 averages, a computer program was used which analyzed the roundness gradients between set up conditions and formed contour lines shown in Figure 6.5. The contours represent lines of constant out-of-round. For example, the set up condition γ=15 (ϕ_2=165), ϕ_1=60 produced pieces between 60μin and 90μin out-of-round on average. Close inspection of the plot yields several interesting conclusions. First, for $\gamma < 11(\phi_2 > 169)$ degrees, the general conclusion from other researchers that the optimal center height is between 6 and 8 degrees (ϕ_2=172 to 174) holds true. Second, there is a large range for γ between 13 and 20 degrees (ϕ_2= 160 to 167) where the roundness is better than at γ=7 degrees. In this range, the minimum point was found near ϕ_1=41, γ=18 (ϕ_2=162) degrees which is quite near the theoretical minimum from Figure 4.15. This set up condition produced an average roundness less than 39μin from over ten pieces.

The general trends predicted in Figure 4.15 were found in the actual testing represented in Figure 6.5. Nothing like the plot in Figure 6.5 has ever been published before for centerless grinding. The most extensive research published in the past has centered around picking either ϕ_1 or ϕ_2 constant and varying the other over a small range (usually 10 degrees or less). Once again, it should be noted that friction force considerations limit wheel-type centerless grinding to values of $\gamma < 11$ degrees, so the majority of the chart is available only to shoe-type centerless grinding. Still, the fact that the theoretical trends predicted in 4.5.2 are generally supported by the experiments is significant.

6.4 Unstable Vibration Tests

As noted, vibration tests were conducted under the same conditions as above except the workpiece speed was doubled to allow the machine's 800Hz resonance

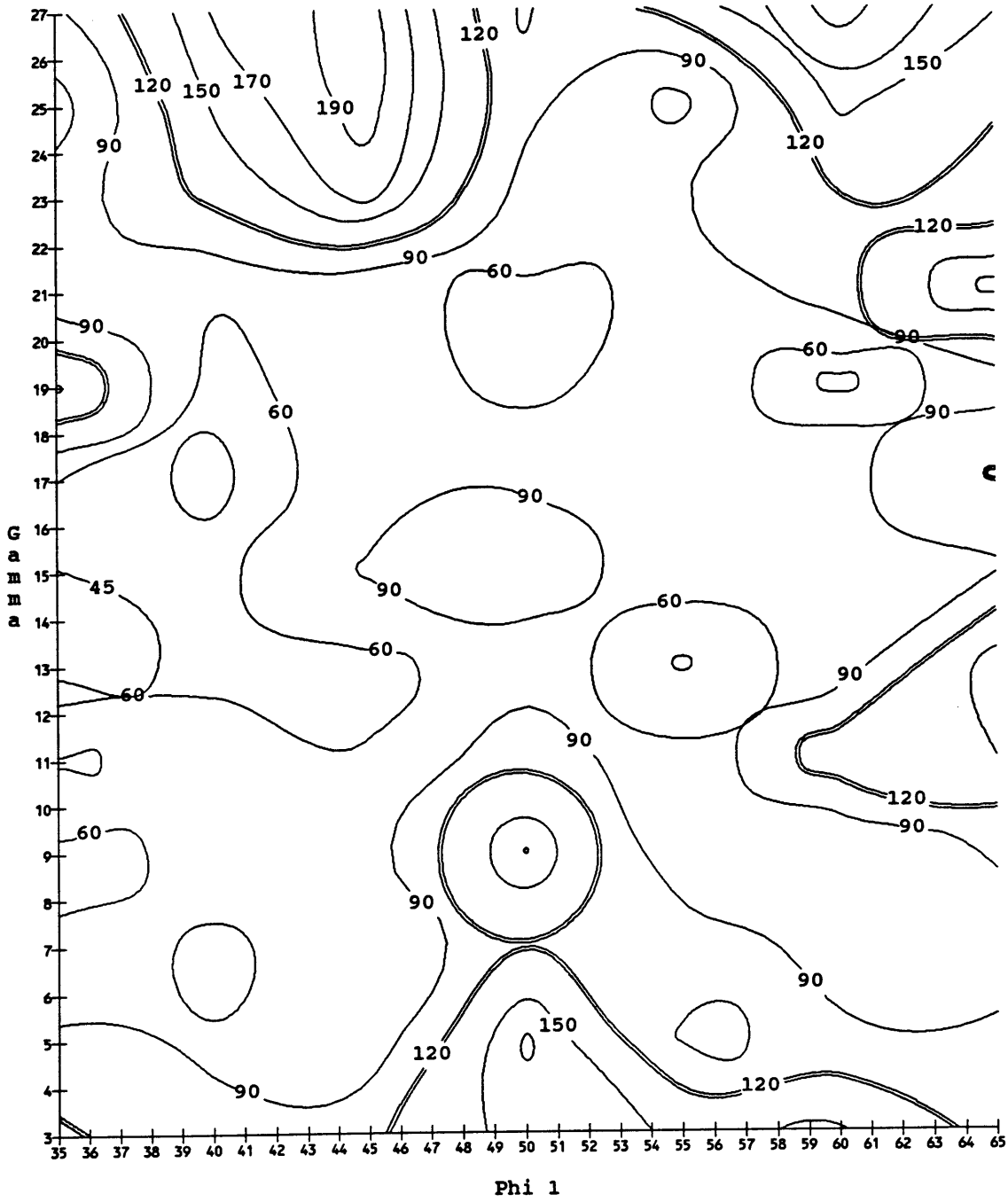

Figure 6-5: Contourplot showing the experimental roundness levels from the experimental averages. A computer program was used to interpolate between points.

(possibly due to imbalance of the wheel) to play a part in the workpiece roundness. Each part was ground for a period of 55 seconds unless vibration grew to a point where the process needed to be stopped. An accelerometer was affixed to the rear shoe in the sensitive direction and a digital 'strip chart' recorder was used to record the vibration output. Figure 6.6 shows a stable grinding set up of ϕ_1=69 and ϕ_2=166 degrees. As can be seen the amplitude of vibration was constant or even decreased during the entire 55 seconds of grinding. If an exponential curve is fitted to this graph, then the exponent, σ, would be zero or slightly negative. Figure 6.7 shows an unstable set up for ϕ_1=52 and ϕ_2=160 degrees. As can be seen the vibration initially decreases slightly due to an initial decrease in out-of-round, but the 800Hz frequency slowly takes over and grows at an exponential rate until the system saturates with vibration. If an exponential curve is fitted to this graph (before saturation) then a positive exponent, $\sigma = .0268$, is found.

Eight angles between ϕ_1=40-60 and ϕ_2=160-175 degrees were tested to evaluate the trends in unstable vibration growth in centerless grinding. Figure 6.8 shows a tabular record of these tests which yields the general trend that increasing ϕ_1 or ϕ_2 in the normal grinding range results in increased dynamic stability. This trend coincides with the theoretical predictions from chapter 5.

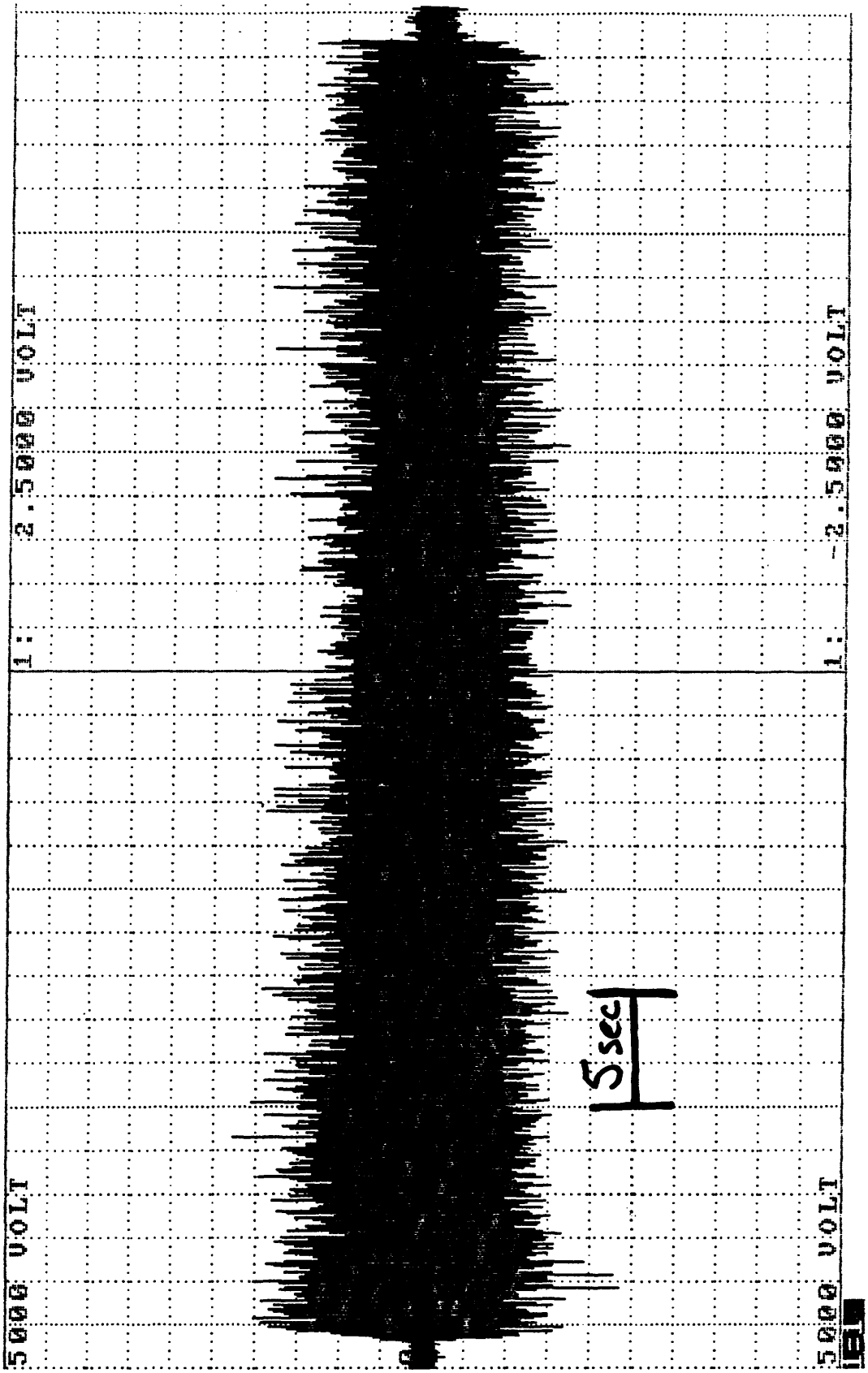

Figure 6-6: Vibration Test during part processing where ϕ_1=69 and ϕ_2=166 degrees. This stable grinding test has a zero or negative vibration growth rate.

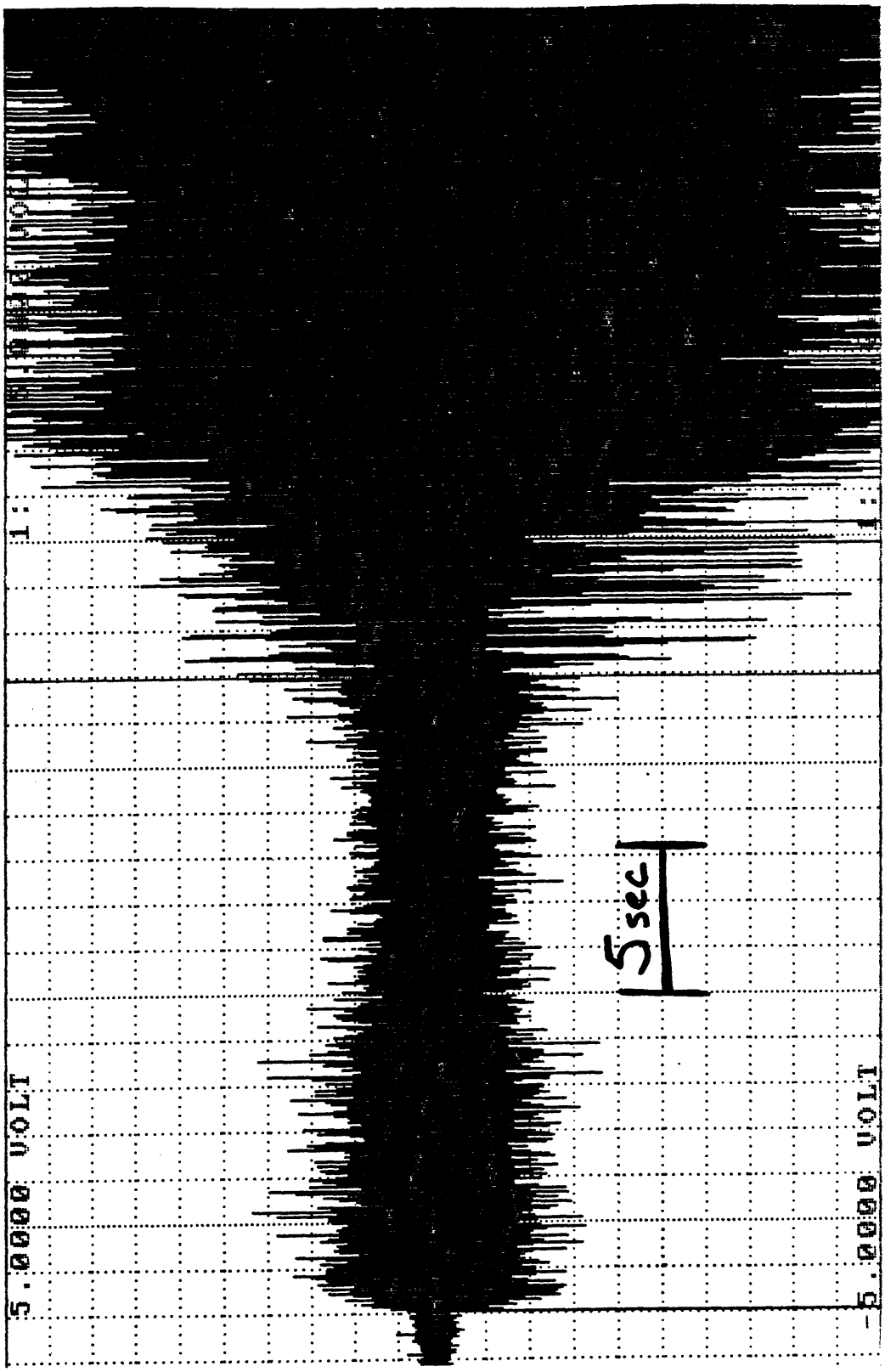

Figure 6-7: Unstable vibration test during part processing where ϕ_1=52 and ϕ_2=160 degrees. This unstable grinding test has a curve-fit exponential growth rate of .0268.

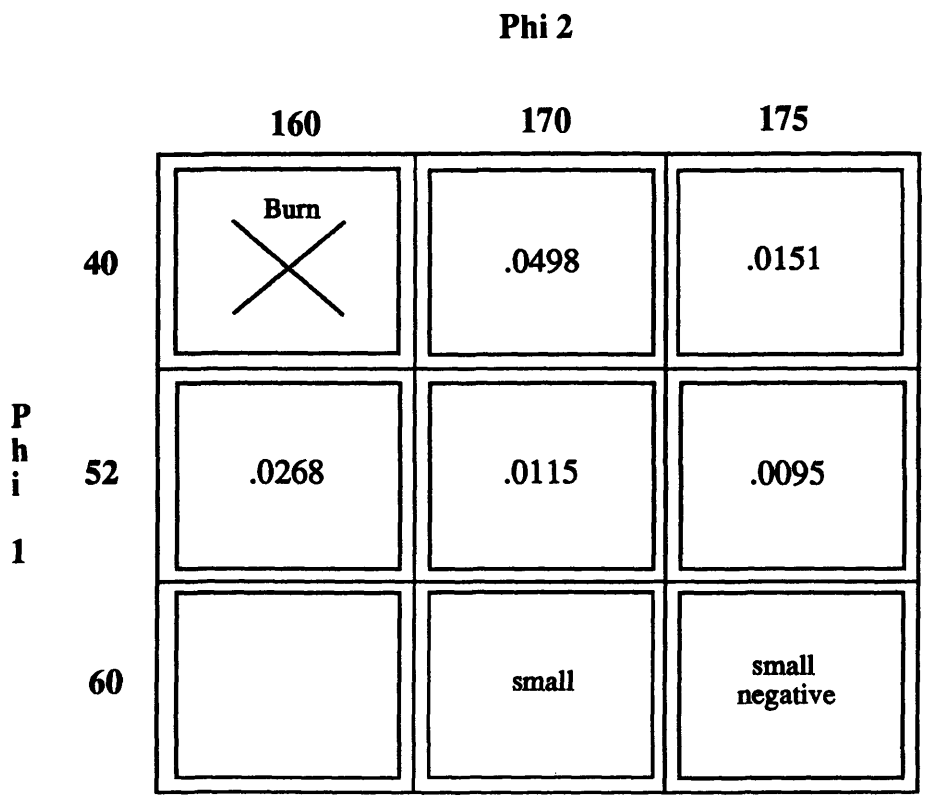

Figure 6-8: Table of vibration tests showing experimental unstable vibration growth rates and the trend that increasing ϕ_1 or ϕ_2 increases stability.

Chapter 7

Comparison and Conclusions

The model presented and analyzed in this study was found to make accurate predictions of the general trends found in centerless grinding. Section 4.4 showed the theoretical prediction of unstable lobes based on purely geometric considerations. Section 6.2 showed the experimental validation of those predictions very accurately, to the point where almost *all* significant lobing found experimentally was generally predicted by theory. Although similar conclusions concerning unstable geometric lobing have been found by other reseachers, the methodology and analysis presented in this study is new.

Section 4.5.2 showed a new method to estimate overall workpiece roundness trends based on set up geometry. Roundness trends were tested experimentally in section 6.3. Some of the conclusions which matched between the theory and experiments for part roundness included the fact that a 6 to 8 degree center-height angle is near optimal for center-heights less than 11 degrees and that there is a better region, ϕ_2=160-167 degrees, accessible only to shoe-type centerless grinding. Thus, using the methodology proposed with a dynamically stable machine, it is possible to predict final workpiece roundness trends based solely on the two shoe angles, ϕ_1 and ϕ_2.

Chapter 5 found the roots of the centerless grinding model. Comparison of the characteristic roots for differing machine models and resonant frequencies all yielded the same general result found experimentally: that increasing ϕ_1 or ϕ_2 yields a general increase in dynamic stability in the normal centerless grinding region. Section 6.4

experimentally verified this general conclusion, lending credence to the methodology presented here.

The analysis methods and conclusions from section 4.5 and chapter 5, the predictions of roundness and dynamic stability trends based on set up geometry, have not been published before for centerless grinding. The methods presented here allow a more complete understanding of the centerless grinding process. The theoretical predictions, especially of part roundness trends, are directly applicable to the bearing industry. Backed up with conclusive experimental results, this study yields useful information about the production of circular cross sections using the centerless grinding process.

Bibliography

1. R. Bueno, F. LeMaitre, M. Zatarain. **Geometric and Dynamic Stability in Centerless Grinding.** *Annals of the CIRP.* 39/1/1990 p395-398

2. H.S. Lee, Y. Furukawa. **Stiffness Design Method in Grinding Machines.** *Bulletin of Japan Society of Precision Engineers.* v24n2 June 1990 p136-141

3. H.S. Lee, Y. Furukawa. **On the Method to Determine the Stiffness of Grinding Machines.** *Bulletin of Japan Society of Precision Engineers.* v22n2 June 1988 p127-132

4. T. Matsubara, H. Mizumoto, H. Yamamoto, M. Sato. **Experimental Analysis of Work Regenerative Chatter in Plunge Grinding.** *Bulletin of Japan Society of Precision Engineers.* v21n1 March 1987 p33

5. T. Matsubara, H. Mizumoto, H. Yamamoto. **Theoretical Analysis of Work Regenerative Chatter in Plunge Grinding.** *Bulletin of Japan Society of Precision Engineers.* v20n4 December 1986 p272-277

6. T. Matsubara, H. Yamamoto, H. Mizumoto. **Study on Regenerative Chatter Vibration with Dynamic Cutting Force.** *Bulletin of Japan Society of Precision Engineers.* v19n4 December 1985 p260-265

7. W.B. Rowe, S. Spraggett, R. Gill, J.B. Davies. **Improvement in Centerless Grinding Machine Design.** *Annals of the CIRP.* 38/1/1987 p207-210

8. W.B. Rowe. **Research into the Mechanics of Centerless Grinding.** *Precision Engineering.* 1979 p75-83

9. W.B. Rowe, D.L. Richards. **Geometric Stability Charts for the Centerless Grinding Process.** *Journal of Mechanical Engineering Science.* v1n2 1972

10. W.B. Rowe, F. Koenigsberger. **Some Roundness Characteristics of Centerless Grinding.** *International Journal of Machine Tool Design Research.* v5 1965 p203-215

11. W.B. Rowe, F. Koenigsberger. **The Work-Regenerative Effect in Centerless Grinding.** *International Journal of Machine Tool Design Research.* v5 1965 p175-187

12. W.B. Rowe, M.M. Barash. **Computer Method for Investigating the Accuracy of Centerless Grinding.** *International Journal of Machine Tool Design Research.* v4 1964 p91-116

13. N. Udupa, M. Shunmugam, V. Radhakrishnan. **Three-dimensional geometric analysis of the plunge centerless grinding process.** *Proceedings of the Institution of Mechanical Engineering.* v201nC5 1987 p309-320

14. R.S. Hahn, R.I. King. *Handbook of Modern Grinding Technology.* 1986

15. R.S. Hahn. **Grinding Chatter in Precision Grinding Operations–Causes and Cures.** *SME Manufacturing Engineering Transactions.* 1979 p29-34

16. A.Y. Chien. **The Harmonic Vibration Models in Centerless Grinding.** *International Journal of Machine Tool Design Research.* v26n4 1986 p349-358

17. A.Y. Chien. **The Selection of Optimal Stable Geometrical Configurations on Centerless Grinding.** *International Journal of Machine Tool Design Research.* v24n2 1984 p87-93

18. A.Y. Chien. **The Rounding Off Theory in Centerless Grinding.** *International Journal of Machine Tool Design Research.* v21n 1981 p49-55

19. K. Steffens, H. Follinger, W. Konig. **A New Approach for Investigating Dynamic Effects in Grinding.** *Annals of the CIRP.* 34/1/1985 p267-270

20. K. Steffens, W. Konig. **Closed Loop Simulation of Grinding.** *Annals of the CIRP.* 32/1/1983 p255-259

21. M. Frost, P. Furdson. **Toward Optimal Centerless Grinding.** *ASME Milton C. Shaw Grinding Symposium.* 1985 p313-328

22. F. Hashimoto, J. Yoshioka, M. Miyashita. **Sequential Estimation of Growth of Chatter Vibration in Grinding Process.** *Annals off the CIRP.* 34/1/1985 p271

23. F. Hashimoto, A. Kanai, M. Miyashita, K. Okamura. **Grinding Mechanism of Chatter Vibrations in Grinding Processes and Chatter Stabilization of Grinding Wheel.** *Annals of the CIRP.* 33/1/1984

24. M. Miyashita, F. Hashimoto, A. Kanai, K. Okamura. **Diagram for Selecting Chatter Free Conditions of Centerless Grinding.** *Annals of the CIRP.* 31/1/1982 p221-223

25. M. Miyashita. **Unstable Vibration Analysis of Centerless Grinding System and Remedies for Its Stabilization.** *Annals of the CIRP.* 21/1/1972 p103-104

26. M. Miyashita. **Chatter Vibration in Centerless Grinding.** *Bulletin of Japan Society of Precision Engineers.* v3n3 1969 p53-59

27. R.J. Baylis, B.J. Stone, J.G. Wagner. **The Build Up and Decay of Vibration During Grinding.** *Annals of the CIRP.* 32/1/1983 p265-826

28. K. Srinivasan. **Application of the Regeneration Spectrum Method to Wheel Regenerative Chatter in Grinding.** *Transactions of the ASME.* v104 February 1982 p46-54

29. M. Weck, K.H. Schiefer. **Interaction of the Dynamic Behavior between Machine Tool and Cutting Process for Grinding.** *Annals of the CIRP.* 28/1/1979 p281-285

30. L.F. Kotov, V.D. Gershenzon. **Irregular Workpiece Rotation in Centerless Grinding on Fixed Pads.** *Machines and Tooling.* vXLIIn7 July 1977

31. I. Inaski, S. Yonetsu **Regenerative Chatter in Grinding.** *18th International Machine Tool Design and Research Conference.* 1977 p423-429

32. Y. Furukawa, M. Miyashita, S. Shiozaki. **Chatter Vibration in Centerless Grinding.** Parts 1 and 2 *Bulletin of the JSME.* v13n64 1970 p1274 and v15n82 1972 p544

33. Y. Furukawa, M. Miyashita, S. Shoizaki. **Vibration Analysis and Work Rounding Mechanism in Centerless Grinding.** *International Journal of Machine Tool Design Research.* v11 1971 p145-175

34. R. Snoeys, D. Brown. **Dominating Parameters in grinding Wheel and Workpiece Regenerative Chatter.** *Proceedings of the 10th International Machine Tool Design and Research Conference.* 1969 p325-348

35. R. Snoeys, I. Wang. **Analysis of the Static and Dynamic Stiffness of the Grinding Wheel Surface.** *Proceedings of the 9th International Machine Tool Design and Research Conference.* 1968 n2 p1133-1148

36. J.P. Gurney. **An Analysis of Centerless Grinding.** *ASME Journal of Engineering for Industry.* May 1964 p163-174

37. A.H. Dall. **Rounding Effect in Centerless Grinding.** *Mechanical Engineering N.Y.* v58 April 1946 p325-329

38. E. Sachsenberg, R.Kreher. **Centerless Grinding.** *Werkstattstechnik.* v33 1939 p280